Part I: Optically Induced, Ferroelectric Domain Gratings in Photorefractive Crystals and Applications to Nonlinear Optics

Part II: Self-Focusing and Self-Trapping of Optical Beams Upon Photopolymerization and Applications to Microfabrication

Thesis by

Anthony S. Kewitsch

In Partial Fulfillment of the Requirements

for the Degree of

Doctor of Philosophy

California Institute of Technology

Pasadena, California

1995

(Submitted May 16, 1995)

In memory of my father and sister

Acknowledgments

I would first like to thank my thesis advisor, Amnon Yariv, for his support, friendship and inspiration. The research environment he cultivates is a pleasure and honor to work in. I would also like to thank Mordechai Segev for his enthusiastic and energetic support. I deeply appreciate his friendship and guidance. Many members of the Caltech Quantum Electronics Group have been a pleasure to interact with and learn from, including (in alphabetical order): Roni Agranat, Gilad Almogy, Gert Cauwenberghs, Lars Eng, Doruk Engin, Rudy Hofmeister, John Iannelli, John Kitching, Victor Leyva, Bill Marshall, Chuck Neugebauer, John O'Brien, Sergei Orlov, Volnei Pedroni, George Rakuljic, Joseph Rosen, Akira Saito, Randy Salvatore, Thomas Schrans, Ali Shakouri, Xiao-lin Tong, Yuanjian Xu, Shogo Yagi and Min Zhang.

I wish to thank the numerous individuals whom I have had the pleasure to collaborate with, including Gregory Salamo, Edward Sharp, Ratnakar Neurgaonkar and Terrence Towe. Several experts who provided valuable insight related to this thesis research include George Rossman, Eric Cross, Robert Grubbs, Michael Hecht and Yu-Chong Tai. I thank them for their time and patience. Finally, I would like to thank Paul Davis, Anthony Siegman and David Jackson for the early opportunities to pursue undergraduate research under their supervision.

Several Caltech staff members have provided extraordinary assistance, in particular Ali Ghaffari, Paula Samazon, Reynold Johnson, Jana Mercado, and Larry Begay. I would

also like to thank Tony Stark, Ray Garcia, Bob Paz, and the staff of the interlibrary loan office.

First and foremost, I would like to thank my parents and sister for their unwavering support. The lessons in life they provided are the most priceless knowledge of all.

Abstract

This thesis explores the application of two distinct nonlinear optical phenomena, the photorefractive effect and photopolymerization, to optically generate microstructures with feature sizes on the order of optical wavelengths. First, we have found that in certain photorefractive crystals, the photogenerated space charge field dynamically aligns ferroelectric domains. This is demonstrated by the observation of Barkhausen noise linked to the formation of domain gratings. Domain gratings are recorded with spatial periods on the order of optical wavelengths, which we use for quasi-phase matched second harmonic generation and holographic data storage.

The second part of this thesis explores the nonlinear optical response accompanying photopolymerization. In some photopolymers, the crosslinking of polymer chains induces a significant increase in the index of refraction in the exposed region. This index perturbation acts as a lens which subsequently focuses down the input light wave. We observe self-focused and self-trapped optical beams upon photo-induced crosslinking of a liquid monomer. In the case of self-trapping, the inherent diffraction of the optical beam is exactly balanced by self-focusing, so the diameter of the beam does not change as it propagates through the medium. Most importantly, this waveguiding generates solid polymer microstructures in the illuminated region, which can be used to fabricate micro-electromechanical systems and optical interconnects.

Preface

This thesis explores the application of two diverse nonlinear optical phenomena, the photorefractive effect and photopolymerization, to the generation of microstructures with feature sizes on the order of a micron. First, we explore the use of optical interference patterns to tailor the ferroelectric domain microstructure of SBN crystals. The dynamic alignment of ferroelectric domains is observed in response to a photorefractive space charge field. Chapter one describes the theoretical and experimental background of the photorefractive effect and its application to record photorefractive holograms. The material properties of several photorefractive ferroelectrics are discussed in chapter two.

Photorefractive space charge fields modulate the index of refraction by slightly distorting the position of ions within the crystalline lattice through the linear electrooptic effect (chapter three). However, we demonstrate that near the ferroelectric/paraelectric phase transition, materials such as strontium barium niobate (SBN) exhibit hysteresis in the electrooptic effect (chapter four). That is, ions not only displace slightly, but also undergo inversion through the center of symmetry. This study demonstrates that in low coercive field ferroelectrics such as SBN, the dynamic alignment of domains plays an intimate and previously unappreciated role in the generation of index gratings. This interpretation is drawn from the experimental observation of Barkhausen noise, a signature of domain switching, while optically recording domain gratings. This is the subject of chapter five.

Chapter six describes one application of this hysteretic electrooptic effect: volume holographic storage. An important issue in holographic storage is the lifetime of the data upon readout. Photorefractive holograms are normally destroyed upon reconstruction unless a thermal fixing stage is applied. However, we show that photorefractive hologram lifetimes exceed 100 days in SBN crystals, a consequence of ferroelectric hysteresis. This selective, page-addressable fixing process occurs automatically.

The application of domain microstructures to quasi-phase matched second harmonic generation is the subject of chapter seven. Optically induced polarization gratings enhance the second-harmonic conversion efficiency by ensuring that momentum is conserved during the nonlinear interaction. In fact, we observe that the peak second-harmonic conversion efficiency is enhanced by a factor of 700 upon recording a domain hologram. The wavelength response is further tailored by writing an ensemble of gratings within the same volume. Each grating enhances the second-harmonic generation at a predetermined wavelength.

The second part of this thesis describes the formation of polymeric microstructures based on self-focusing and self-trapping of optical beams upon photopolymerization. By illuminating a photopolymer with UV radiation, the liquid polymer is crosslinked to produce a solid structure. The photochemistry and polymer chemistry of this process is presented in chapter eight. For some photopolymers, the index of refraction increases upon crosslinking. The origin of this index change is discussed analytically in chapter nine. We show that this index increase enables optical beams to be self-focused or self-trapped within the polymeric waveguides (chapter ten). This self-trapping balances the inherent diffraction. We numerically simulate self-focusing and self-trapping, as described in chapter eleven.

In chapter twelve we demonstrate the use of self-trapping to fabricate very deep polymeric structures with transverse dimensions on the order of optical wavelengths. This relaxes the fundamental limit to the depth of focus imposed by diffraction and enables the microfabrication of structures with extremely large depth-to-width aspect ratios. The liquid material may be removed after exposure, leaving solidified polymer only in the original illuminated regions. Polymer microstructures with feature sizes of 10 μm and 1 cm deep have been fabricated. This technique may be instrumental in fabricating optical filters, optical memory devices, micro-electromechanical systems and optical interconnects.

Table of Contents

Chapter One

Introduction to Photorefractive Nonlinear Optics

1.1 Introduction

The photorefractive effect is a nonlinear optical response characterized by a change in the optical index of refraction proportional to the absorbed optical energy. The photorefractive effect was first reported in 1966 by Ashkin et al. [1] in ferroelectrics and classified as "optical damage." A high intensity visible laser source induced index perturbations that survived even after the beam was extinguished. The visible laser deposited electronic space charge along the periphery of the beam, which induced an index change through the linear electrooptic effect. Soon thereafter, Chen et al. demonstrated that these index changes could be used to store high resolution, dynamic volume phase holograms [2]. That is, holograms could be recorded by coherent illumination in the visible spectrum and erased by uniform visible illumination. The promise of these early observations provided the impetus for further study of the photorefractive effect and its applications to holographic memories, optical processors and display devices.

1.2 Band Transport Theory

The dependence of the index change on the optical exposure is described quantitatively by the band transport theory applied to photorefractive materials by Kukhtaerev et al. [3]. The

material is assumed to consist of non-photoactive, deep acceptor levels, N_a, which ionize some fraction of optically excitable donor levels N_d (figure 1.1) at room temperature. The material is illuminated with an optical interference pattern:

$$I(x) = I_o + I_1 e^{ikx} + c.c. . \qquad 1.1$$

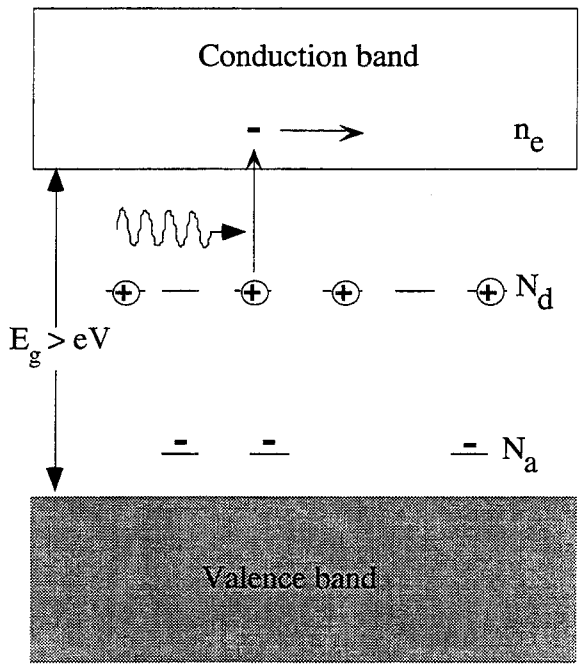

Figure 1.1: Photorefractive band model for one photorefractive donor species N_d. Note that $N_a + n_e = N_d^+$.

In the regions of illumination, electrons are excited from the donor levels N_d, to the conduction band, where they drift and diffuse until recombining. After many cycles of excitation and recombination, electrons will tend to accumulate in the dark regions of the interference fringes, resulting in a modulated density of ionized donors N_d^+. This produces a local space charge field (figure 1.2) which is a slightly distorted replica of the optical

intensity pattern. In non-centrosymmetric electrooptic materials, this local electric field produces an index change through the linear electrooptic effect [4]:

$$\Delta\left(\frac{1}{n^2}\right)_{ij} = r_{ijk}\, E_k \,. \qquad 1.2$$

r_{ijk} is the third-rank linear electrooptic tensor, and E_k is the component of the electric field along the k direction. This electric field is generated by the modulated density of ionized donors.

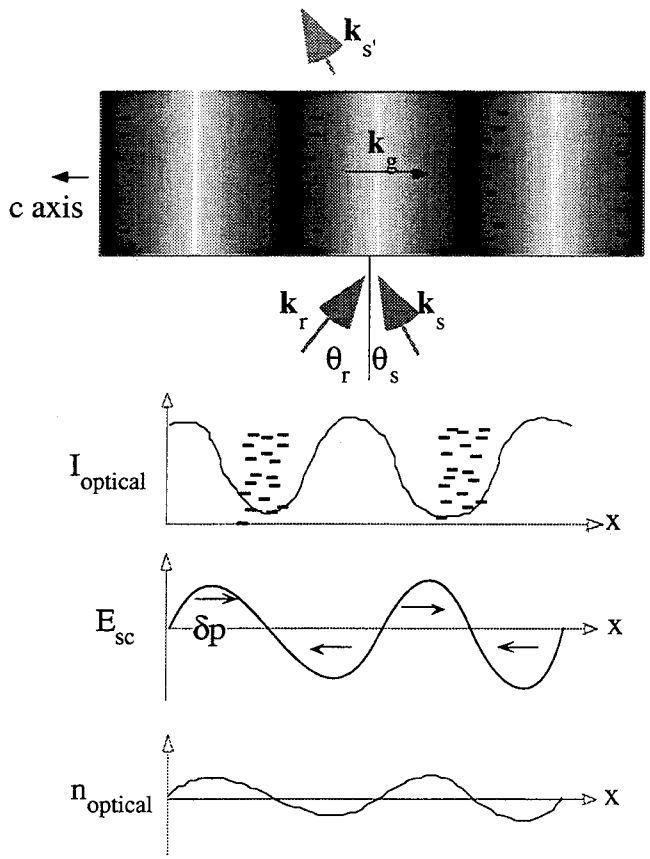

Figure 1.2: Optical interference pattern spatially modulates the density of ionized donors, producing a space charge field E_{sc} which modulates the index of refraction through the electrooptic effect.

The electric field can be determined analytically by modeling the charge transport occurring under the periodic illumination described by equation 1.1. A rate equation describes the density of excited donor atoms N_d^+ under illumination and in the presence of recombination:

$$\frac{\partial N_D^+(x,t)}{\partial t} = \alpha \eta \frac{I(x)}{h\nu} - \frac{n_e}{\tau_r}. \qquad 1.3$$

α is the absorption cross section, η is the quantum efficiency of optical excitation, ν is the frequency of the incident light intensity pattern $I(x)$, n_e is the density of electrons in the conduction band and t_r is the recombination time. This produces a photocurrent J_x composed of drift and diffusion terms:

$$J_x = \mu e n_e E_x + k_B T \mu \frac{\partial n_e}{\partial x}. \qquad 1.4$$

μ is the electron mobility in the conduction band. Note that the photovoltaic charge transport mechanism is negligible in ferroelectrics such as SBN [5], so it is ignored in this treatment. The current continuity equation relates this current to the rate of excitation of ionized donors:

$$\frac{\partial J_x}{\partial x} = -e \frac{\partial}{\partial t}\left(N_D^+ - n_e\right). \qquad 1.5$$

The electric field is obtained by integrating the charge density according to Gauss' law:

$$\frac{\partial E_x}{\partial x} = \frac{e}{\varepsilon}\left(N_d^+ - n_e - N_a\right). \qquad 1.6$$

The crystal is assumed to be initially charge neutral so the spatial average of the total charge density $\rho = N_d^+ - n_e - N_a$ is zero:

$$\langle \rho(x) \rangle_x = 0. \qquad 1.7$$

By solving equations 1.1 through 1.7 for small intensity modulation (i.e., $I_1/I_o << 1$), the steady state, photorefractive space charge field with spatial periodicity Λ_g is:

$$E_{sc} = \frac{i E_d}{1 + \frac{E_d}{E_q}} \left[\frac{1 + i \frac{E_o}{E_d}}{1 + i \left(\frac{E_o}{E_d + E_q} \right)} \right] \frac{I_1}{I_o}, \qquad 1.8$$

where the diffusion field E_d is defined as

$$E_d = k_g \frac{k_B T}{q} \quad . \qquad 1.9$$

The limiting space charge field E_q is

$$E_q = \frac{q N_a}{k_g \varepsilon}, \qquad 1.10$$

and the grating vector k_g is defined as

$$k_g = \frac{2\pi}{\Lambda_g} \, . \qquad 1.11$$

E_o is the external, uniform electric field parallel to k_g. Equation 1.8 predicts the grating period dependence of the space charge field. Qualitatively, this dependence is illustrated in figure 1.3. The upper curves depict the diffusion and limiting space charge fields. The bottom curve indicates the net space charge field given by equation 1.8, whose maximum value is typically less than 10 kV cm^{-1}.

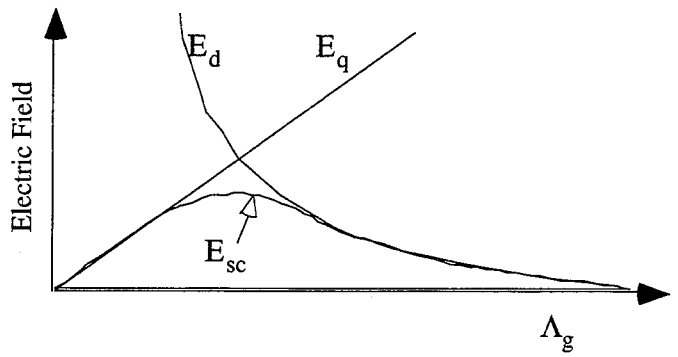

Figure 1.3: Grating period dependence of photorefractive space charge field.

The band transport equations can be solved in the transient regime, before the space charge field reaches the steady-state value described by equation 1.8. The transient space charge field at the fundamental grating component is [6]:

$$E_{sc}(t) = E_{sc}\left[-\cos\left(k_g z + \phi\right) + \exp\left(-t/\tau_g\right)\cos\left(k_g z + \omega_g t + \phi\right)\right] \quad . \qquad 1.12$$

The constants of equation 1.12 are:

$$E_{sc} = \frac{I_1}{I_o} E_q \left[\frac{E_o^2 + E_d^2}{E_o^2 + (E_d + E_q)^2}\right]^{1/2}, \qquad 1.13$$

where ϕ is the photorefractive phase shift, defined as the phase difference between the intensity and index maxima:

$$\phi = \tan^{-1}\left[\frac{(E_d + E_q)\,E_d + E_o^2}{E_o\,E_q}\right], \qquad 1.14$$

and

$$\tau_g = \tau_d \frac{\left(1 + \frac{E_d}{E_\mu}\right)^2 + \left(\frac{E_o}{E_\mu}\right)^2}{\left(1 + \frac{E_d}{E_q}\right)\left(1 + \frac{E_d}{E_\mu}\right) + \frac{E_o}{E_\mu}\frac{E_o}{E_q}}, \qquad 1.15$$

$$\omega_g = \frac{1}{\tau_d} \frac{\frac{E_o}{E_q} - \frac{E_o}{E_\mu}}{\left(1 + \frac{E_d}{E_\mu}\right)^2 + \left(\frac{E_o}{E_\mu}\right)^2}. \qquad 1.16$$

τ_d is the Maxwellian or dielectric relaxation time:

$$\tau_d = \frac{\varepsilon}{\sigma_d}, \qquad 1.17$$

and

$$E_\mu = \frac{\gamma_R N_A}{\mu\, k_g}. \qquad 1.18$$

These relations indicate that the space charge field grows approximately linearly with time until the onset of saturation. When an external electric field is applied parallel to the grating vector, the space charge field may "ring" like an underdamped simple harmonic oscillator.

1.3 Diffraction From Volume Phase Holograms

For a medium of thickness L with a sinusoidal index perturbation of amplitude n_1, as in figure 1.2, the diffraction efficiency η is obtained by solving the two beam coupled wave equations for transmission gratings in the symmetric configuration (depicted in figure 1.2 with $\theta_r = \theta_s$). If diffraction from a fixed transmission grating is considered in the absence of self-enhancement [7], the diffraction efficiency [8]:

$$\eta = \frac{I_2(L)}{I_1(0)}, \qquad 1.19$$

is equal to:

$$\eta = \exp\left(-\frac{\alpha L}{\cos\theta}\right)\sin^2\left(\frac{\pi n_1 L}{\lambda \cos\theta}\right). \qquad 1.20$$

α is the absorption coefficient and $\theta = \theta_r = \theta_s$. Note that for weak diffraction, the diffraction efficiency is proportional to the square of the index modulation n_1. Therefore, for a linear electrooptic material, the diffraction efficiency is proportional to the square of the photorefractive space charge field. In chapter five, the space charge field is computed from the measured diffraction efficiency using equation 1.20.

1.4 Permanent Fixing of Photorefractive Gratings

Volume phase holograms have been stored in a wide range of materials: silver halide photographic emulsions, dichromated gelatin films, photosensitive glass, photorefractive polymers, organic materials and ferroelectric crystals [9]. Each of these materials poses a unique set of technological problems when attempting to record optical interference patterns as permanent index gratings. These issues include dimensional stability, optical sensitivity,

scattering, shrinkage after development, dynamic range (i.e., maximum index change), and the hologram lifetime.

Two common ferroelectric oxide crystals for recording volume phase holograms are $LiNbO_3$ and $Sr_xBa_{1-x}Nb_2O_6$ (SBN:x). When these materials are doped to optimize their photoconductive properties, optical interference patterns redistribute charge among traps to generate local electronic space charge fields which are replicas of optical interference patterns (but generally shifted in phase and spatially distorted because of electron/hole diffusion). An index change typically arises from the spatially modulated space charge field through the linear electrooptic effect. The complex microscopic details of this process are absorbed within a measured electrooptic tensor r_{ijk} which relates the index change to the space charge field. These index gratings are electronic in origin, so they are bleached by the same optical field that reconstructs them. This dynamic property is extremely useful for real time holography applications; however, for applications such as holographic data storage, permanent index gratings are desirable.

The goal of hologram fixing techniques in ferroelectrics is to transform the grating composed of a spatially modulated density of optically active species (electrons, holes) into a modulated density of optically inactive species (ion cores, vacancies, defects). This has been achieved with varying degrees of success in $LiNbO_3$, $LiTaO_3$, $Ba_2NaNb_5O_{15}$, SBN, $KNbO_3$, KLTN, and $BaTiO_3$. The common fixing stage in these oxides is the conversion of a dynamic grating composed of electrons and/or holes into its replica composed of stable, displaced ions. Upon reconstruction of the hologram, the electronic grating is partially erased and the ionic grating persists. These ions are typically optically inactive and have a relatively low mobility. The obstacle to fixing is the simultaneous requirement that ions must be mobile enough to redistribute under the influence of local space charge fields, yet be resistant to optical erasure. In addition, mobile charge tends to redistribute to

minimize electric fields within the crystal, leading to compensation of the revealed, fixed grating. This effect reduces the net diffraction efficiency from the grating.

One technique to achieve fixing is to uniformly heat the crystal during or after the hologram recording process so that ions can drift under the influence of electronic space charge fields. A second technique uses the hysteresis associated with the reversal of ferroelectric domains to provide memory even after the electronic space charge fields are diminished. This hysteresis may be increased to a significant level by applying external electric fields or by recording near the ferroelectric Curie temperature. In contrast to a ferromagnetic memory, in which the magnetization can be reversed locally on a surface by a magnetic recording head, periodic electric fields can modulate the polarization locally throughout the entire volume of the ferroelectric.

1.5 Fixing by Thermally Assisted Ionic Drift

Fixing by ionic drift was first demonstrated in $LiNbO_3$ in 1971 by Amodei and Staebler [10]. They discovered that by heating the crystal to 100-200 ^oC either during or after the hologram exposure and by subsequently cooling, a permanent grating 180 degrees out of phase with the electronic grating was generated. They proposed that at elevated temperatures, the electronic space charge field generated by optically excitable ions causes optically inactive ions or vacancies to drift under the force of the local space charge grating to compensate the local fields. The electronic grating remains trapped in the absence of light and at the elevated temperatures because electrons recombine at sufficiently deep traps (> eV). When the crystal is cooled to room temperature in the dark, the ionic grating is rendered immobile. The electronic grating is subsequently depleted by uniform illumination, causing the diffraction efficiency to vanish when the electronic and ionic

grating are equal in magnitude and opposite in sign. Further erasure of the electronic grating reveals the fixed ionic grating.

Thermal fixing has been demonstrated in $LiNbO_3$ samples of various doping combinations, such as Cu, Fe, Mn, Si (see, for example, [11] and references therein) as well as $LiTaO_3$:Fe [12] and $Ba_2NaNb_5O_{15}$:(Fe,Mo) [10]. Similar thermal fixing results under an external ac electric field have been reported in the non-ferroelectric $Bi_{12}TiO_{20}$ [13]. Several subsequent studies have followed Amodei and Staebler's original work to determine the ionic species responsible for the fixed grating. It is believed that the drift of protons are primarily responsible for fixing in $LiNbO_3$ [14]. The 1.1 eV activation energy of OH^- ions [15] agrees with the those values (1.1 eV [16] to 0.93 eV [17]) determined from fixed hologram lifetimes, based on an Arrhenius type thermal activation process. The role of protons is further supported by the change in the OH^- infrared absorption band in thermally fixed regions [18]. The OH^- is believed to enter the crystal lattice during crystal growth [14]. Subsequent proton migration induced by the space charge field takes place at about 140 °C, well below the temperature at which electron modulation in deep traps is thermally degraded ($\geq$ 180 °C) [14]. At room temperature, the probability of ion redistribution by an Arrhenius type activation process is exceeding low (10^{-17}). The dark storage time is estimated to be approximately 10^5 years [19]. A comprehensive discussion of experimental results related to thermal fixing in $LiNbO_3$ may be found in reference [17].

Fixed diffraction efficiencies as large as 32% have been obtained by recording the electronic grating at the elevated fixing temperature [20]. This allows mobile protons to continuously neutralize the electronic space charge field. Since the recording beams remain on, the electronic grating continues to grow until it reaches the limiting space charge value. This technique is effective at grating periods larger than the Debye screening length (i. e., in the diffusion limited regime of the photorefractive band transport model). A large

enhancement in fixing efficiency is produced by short circuiting the crystal while exposing, then developing the grating under open circuit conditions. The largest fixed diffraction efficiency reported in $LiNbO_3$ is 98% for a reflection spectral filter [21].

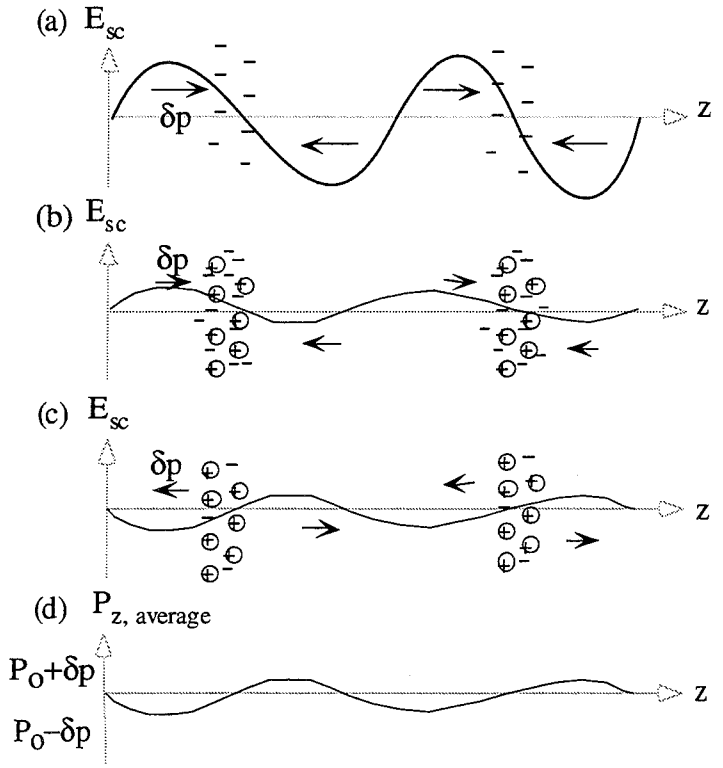

Figure 1.4: Ionic drift fixing method: (a) Generation of spatially modulated electronic space charge field, which induces an index grating through the distortion δp. (b) Upon heating, ions drift to compensate the electronic space charge field. (c) After cooling, crystal is uniformly illuminated to erase the electronic grating and reveal 180 degree out of phase, permanent ionic grating. (d) The permanent modulation of the polarization arising from the net space charge field (ionic - electronic) produces the index grating.

The ionic drift fixing method is illustrated schematically in figure 1.4. In this case the initial buildup of the space charge grating is described by the conventional band transport equations, with the addition of the photovoltaic charge transport mechanism. An electronic space charge grating is recorded under spatially periodic illumination at a sufficiently low

temperature so that ions are immobile (figure 1.4(a)). δp is the change in polarization due to a change in position of the transition metal ion under the influence of the space charge field. This polarization change by definition produces the electrooptic index grating. This is discussed in detail in chapter three. Following electronic hologram recording, the crystal is heated to a temperature at which the ions are mobile while electrons remain immobile in the dark. At elevated temperatures ions compensate the electronic space charge field by drift (b). The net space charge field is diminished. The crystal is cooled and subsequently the hologram is uniformly illuminated, partially erasing the electronic grating and revealing the out-of-phase ionic grating (c). The permanent index modulation arises from the net space charge field (ionic - electronic) perturbing the lattice polarization (d). This polarization grating caused by ionic drift (not domain switching) is 180 degrees out of phase with the initial electronic index grating. Note that the space charge field and polarization as depicted in figure 1.4 are spatially averaged on a scale much larger than a unit cell, yet smaller than the optical wavelength of interest.

1.6 Fixing by Ferroelectric Domain Reversal

Fixing by ferroelectric domain switching is based on the almost binary displacement of ferroelectric ions associated with the spontaneous polarization, rather than the drift of hydrogen impurities. That is, the electrooptic grating exhibits hysteresis. The ions responsible for the electrooptic index change not only distort slightly, but also switch to produce inverted domains. Figure 1.5 illustrates an idealized ferroelectric hysteresis curve for a voltage applied across the c faces of the crystal. P_s is the spontaneous or saturated polarization, P_r is the remnant polarization in the absence of an applied field, and E_c is the coercive field. The coercive field is that field required to invert the spontaneous polarization within half the volume. This hysteresis diagram motivates the fixing methodology only on the most basic level. The electronic space charge field ΔE creates a

replica modulation of the local spontaneous polarization, $\Delta P_{dynamic}$. Upon optical erasure of the electronic space charge field, a remnant polarization modulation $\Delta P_{remnant}$ persists. This produces the fixed hologram. The goal of ferroelectric hysteresis fixing methods is to maximize the memory. Note that the polarization hysteresis diagram represents a *macroscopic* polarization. Since the photorefractive space charge field modulation has a period of microns, which is much greater than the unit cell, the macroscopic picture is applied to a small region in the crystal corresponding to a single grating period. There are two issues to keep in mind when applying this diagram. First, the scale of the hysteresis curve may depend on the size of the domain region under consideration. Second, figure 1.5 is experimentally measured with a voltage source which provides an effectively infinite amount of charge. The photo induced space charge fields provide only limited charge, so charge compensation requirements at domain walls will be a limiting factor in the polarization modulation depth (see chapter three).

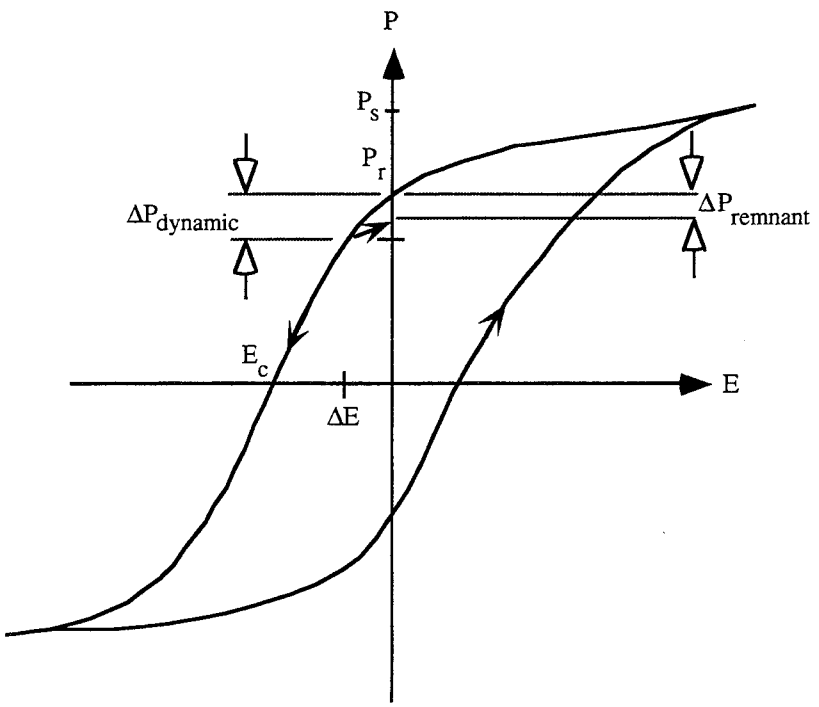

Figure 1.5: Typical polarization hysteresis curve.

Evidence for polarization fixing can be traced back to the early work on optical damage, a phenomenon now synonymous with the photorefractive effect yet actually arising from a variety of photoferroelectric phenomenon. For instance, Ashkin et al. [1] observed antiparallel domains in $BaTiO_3$ following the illumination of an initially poled crystal. Rudyak [22] reported the optical generation of needle shaped 180 degree domains in $LiNbO_3$:Fe following illumination with a single beam at 440 nm, at room temperature. Kovalevich et al. [23] observed a distortion of the crystal structure in the region of illumination in $LiNbO_3$:Fe by the method of x ray diffraction. Following optical erasure, the strain of 0.03% disappears. Apparently, this strain indicates the coupling of the space charge field to the lattice constant through the piezoelectric effect.

These experimental observations suggest that the interaction of light and domains is indeed a common phenomenon shared by many photoferroelectrics. To date, however, efficient ferroelectric domain gratings have been reported only in La doped lead zirconate-titanate (PLZT), SBN and $BaTiO_3$. The results may be classified into the following representative classes: (1) cooling through a ferroelectric phase transition, (2) electrical fixing and (3) photoassisted domain switching. These techniques will be described in this order.

Micheron and Trotier [24] reported on the formation of domain replicas of electronic volume holograms in SBN:75 single crystals while cooling through the paraelectric-ferroelectric phase transition (T_c = 45 °C in their sample). They proposed that in the paraelectric phase, local ionic displacements cancel the photoinduced electronic space charge field. This is expected in the vicinity of the ferroelectric phase transition, where the low frequency dielectric constant is extremely large (~10,000). Upon cooling to the ferroelectric phase, the orientation of the nucleating domains is influenced by the light-induced space charge field, to produce a permanent domain grating. Similar fixing results

were obtained by illuminating with very high optical energy densities (100 W cm^{-2}), apparently because of optical heating.

Electrical fixing of volume holograms in both SBN:75 and $BaTiO_3$ in the head-to-head domain configuration has been demonstrated during the early work on volume holographic memories [25-27] and has been confirmed by more recent work [28, 29]. In principle, this technique has the desirable characteristic that the crystal need not be heated as in thermal fixing and the process can be performed in a relatively short time (~ 1 second) with low intensity optical beams. The electrical field fixing threshold is nearly equal to the average coercive field E_c = - 970 V cm^{-1} (negative values represent depoling fields) and the minimum fixing time is practically limited by the maximum current i_{max} supplied by the voltage source [26]:

$$t_{min} = 2\, Q_r / i_{max} \,, \qquad 1.21$$

where $Q_r = A\, P_r$, A is the area of the electrode and P_r is the remnant polarization. Typically, t_{min} is 10 msec. A fixed efficiency of 52% was achieved with a fixing pulse of 1.25 kV cm^{-1} applied for 0.5 seconds. This domain grating was stable for more than 10 hours during continuous reconstruction with a 1 W cm^{-2} reference beam. The domain pattern is unstable when the fixing voltage is too large compared to the coercive voltage or when the fixing pulse is applied for a time much longer than t_{min}, because significant depolarization of the entire crystal bleaches out the grating modulation. The fixed hologram can be erased by applying a field much larger than the coercive field.

In these experiments the grating vector is oriented nearly parallel to the c axis, so the space charge field is parallel to the c axis. The applied depoling field biases the space charge field near the negative coercive field, increasing the ferroelectric hysteresis. As apparent from

the hysteresis diagram (figure 1.5), the slope dP/dE is a maximum at this point, so significant polarization modulation is expected in this region.

The method to generate ferroelectric domain gratings by space charge fields is illustrated schematically in figure 1.6. The crystal is exposed to spatially periodic illumination (figure 1.6(a)). A depoling field may be applied parallel to the c axis to assist in the domain reversal process after exposure. The internal field can then be estimated to be the sum of the external and space charge field. The initial electronic space charge field (b) induces an index change through the lattice distortion δp. This distortion, unlike the case of ionic drift fixing, also consists of dipoles switching orientations, so a dynamic domain grating is also present. This observation is described in detail in chapter five. Under uniform illumination (c), the electronic space charge field is partially depleted. The polarization perturbation relaxes, but ferroelectric hysteresis prevents the switched dipoles from returning to their pre-exposure locations.

Figure 1.6(a) depicts the resulting inverted microdomains in the regions of negative space charge field, which produce a spatially averaged remnant polarization modulation as shown in figure 1.6(d). The polarization modulation is biased about the spontaneous polarization. Note that the remnant polarization grating is in phase with the initial electronic grating. Thus the spatial phase shift $\Delta\phi$ between adjacent maxima of the two index gratings is zero. Clearly, the same ionic displacements are responsible for both the electrooptic index change and the ferroelectric polarization. This phase relationship is apparent upon reconstruction of the hologram (figure 1.7) while the dynamic grating is optically erased. If the two gratings are in phase ($\Delta\phi = 0$), the diffraction efficiency does not pass through zero upon reconstruction, but decays to the remnant value. However, if the dynamic and remnant gratings are out of phase ($\Delta\phi = \pi$) and the dynamic grating is stronger than the remnant grating, then the diffraction efficiency will go through zero when the two gratings are equal

in strength but opposite in sign, and will thereafter grow as the dynamic grating is further extinguished. Note that this latter case corresponds to the revealing characteristic exhibited following ionic fixing, where the electronic grating is compensated by an ionic grating of opposite sign and smaller magnitude during the heating stage.

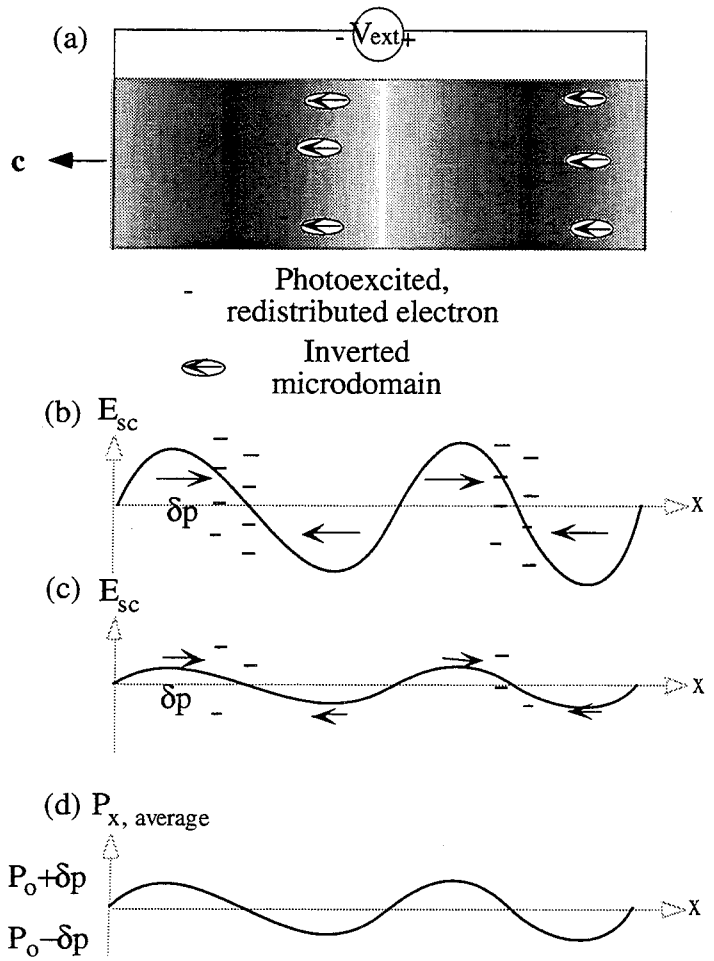

Figure 1.6: Polarization fixing by photoinduced space-charge fields: (a) Experimental setup (b) Generation of spatially modulated electronic space-charge field and resulting index grating caused by distortion δp. (c) Uniform illumination partially erases electronic space charge field; however, a remnant polarization modulation δp persists due to ferroelectric hysteresis. (d) Remnant polarization modulation responsible for fixed domain grating.

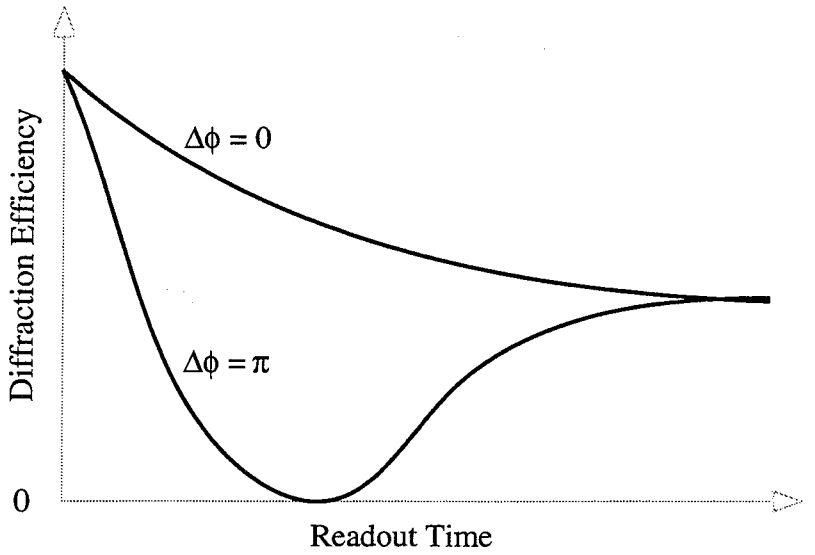

Figure 1.7: Revealing characteristics, depending on relative phase, $\Delta\phi$, of electronic and fixed index gratings.

Another method to fix gratings based on ferroelectric hysteresis is called photoassisted domain switching. This effect plays a dominant role in the formation of ferroelectric domain gratings in configurations where the photoinduced space charge field is perpendicular to the c axis (figure 1.8). In this geometry external electric fields are essential to reverse domains, since the photorefractive space charge fields have a negligible projection along the c axis, the poling direction.

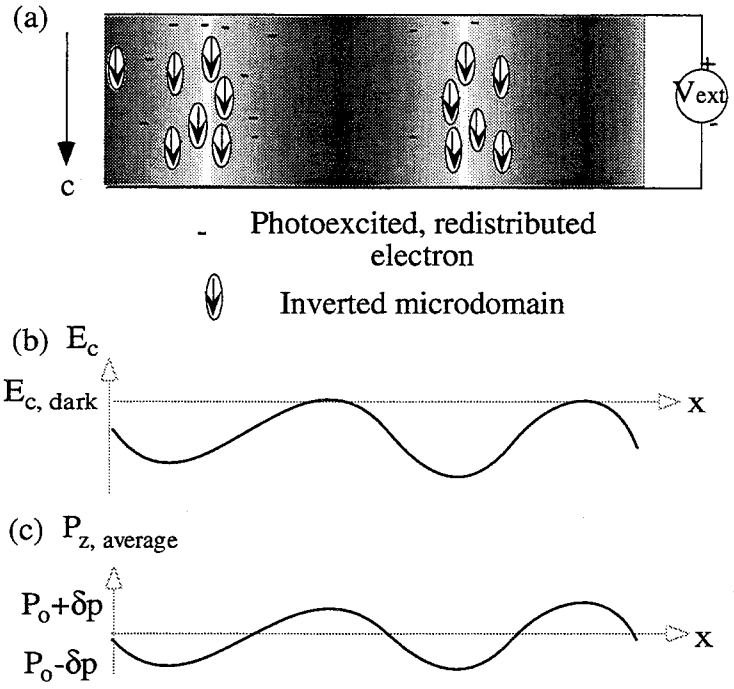

Figure 1.8: Polarization fixing by photoassisted domain reversal. (a) Experimental setup and overview (b) Light intensity pattern modulates the crystal coercive field. (c) An external depoling electric field reduces the spontaneous polarization more significantly along grating planes with low coercive field. As in figure 1.6(d), this remnant polarization modulation produces a fixed domain grating.

The photoassisted domain switching mode of electrical fixing was first demonstrated in photoconductive PLZT ceramics by Smith and Land [30]. They found that uniform illumination assisted both the poling and depoling of the sample. That is, the coercive field was reduced in the illuminated regions. The regions of maximum illumination were completely depoled following the simultaneous exposure and application of a depoling field. A photograph was stored in the poled plate by imaging it onto the ceramic while a depoling electric field was simultaneously applied. The depoled regions produce transmittance minima because the formation of 71° and 109° domain walls enhances the light scattering, creating a negative of the original image. This device was used as a primitive spatial light modulator.

Photoassisted domain switching has also been observed in SBN:60 by Kahmann et al. [31]. In agreement with Smith and Land, they observed depolarization in the illuminated regions following the application of a negative fixing pulse. Because antiparallel domain walls are relatively narrow in SBN, they do not scatter light as strongly as PLZT. The grating is instead revealed by beam coupling topography [32]. Similar observations of polarization gratings in SBN:75 appear to be related to this effect [33, 34].

In regions of illumination, the field required to invert domains is reduced, due to the presence of photoexcited charge which screens the ferroelectric dipole interaction and provides charge to screen the depolarization fields generated upon domain inversion. This lowers the local coercive field in the illuminated regions. Domain reversal is expected in the illuminated regions, and the polarization modulation is exactly out of phase with the intensity pattern.

1.7 Summary

The mechanisms of dynamic hologram grating formation in photorefractives is described by the band transport model. To develop these gratings into permanent replicas, a fixing process must be applied. Fixing has been achieved in a large number of ferroelectric crystals over the past twenty five years. The only technique of practical importance thus far is ionic fixing in $LiNbO_3$. However, there are several promising techniques in SBN based on ferroelectric domain reversal. A fixed grating has been observed in SBN:75 following the application of a depoling electric field along the c axis. This external applied field was believed to convert the photorefractive space charge field into a permanent modulation of the spontaneous polarization. As will be described later, ferroelectric domains automatically orient under the photorefractive space charge even in the absence of an applied field. The presence of this dynamic domain grating has been unappreciated in the

early work on photorefractives, despite the fundamental theoretical and practical implications.

References for chapter one

[1] A. Ashkin, G. D. Boyd, J. M. Dziedzic, R. G. Smith, A. A. Ballman, J. J. Levinstein, K. Nassau, *Appl. Phys. Lett.* **9**, 72-74 (1966).

[2] F. S. Chen, J. T. LaMacchia, D. B. Fraser, *Appl. Phys. Lett.* **13**, 223-225 (1968).

[3] N. V. Kukhtaerev, M. B. Markov, S. G. Odulov, M. S. Soskin, V. L. Vinetsky, *Ferroelectrics* **22**, 949 (1979).

[4] J. F. Nye, *Physical Properties of Crystals Their Representations by Tensors and Matrices.* (Oxford University Press, Oxford, 1964).

[5] B. I. Sturman, V. M. Fridkin, *The Photovoltaic and Photorefractive Effects in Noncentrosymmetric Materials*. G. W. Taylor, Ed., Ferroelectricity and Related Phenomena (Gordon and Breach, Philadelphia, 1992), vol. 8.

[6] P. Yeh, *Introduction of Photorefractive Nonlinear Optics.*, Wiley Series in Pure and Applied Optics (Wiley, New York, 1993).

[7] M. Segev, A. Kewitsch, A. Yariv, G. Rakuljic, *Appl. Phys. Lett.* **62**, 907-909 (1993).

[8] H. Kogelnik, *Bell Syst. Tech. J.* **48**, 2909 (1969).

[9] H. M. Smith, Ed., *Holographic Recording Materials* , vol. 20 (Springer-Verlag, Berlin, 1977).

[10] J. J. Amodei, D. L. Staebler, *Appl. Phys. Lett.* **18**, 540-542 (1971).

[11] R. A. Rupp, *Appl. Phys. B* **41**, 153 (1986).

[12] E. Krätzig, R. Orlowski, *Appl. Phys.* **15**, 133 (1978).

[13] S. W. McCahon, D. Rytz, G. C. Valley, M. B. Klein, B. A. Wechsler, *Appl. Opt.* **28**, 1967-1969 (1989).

[14] R. Müller, L. Arizmendi, M. Carrascosa, J. M. Cabrera, *Appl. Phys. Lett.* **60**, 3212-3214 (1992).

[15] W. Bollmann, H. J. Stöhr, *Phys. Status Solidi (a)* **39**, 477 (1977).

[16] D. L. Staebler, J. J. Amodei, *Ferroelectrics* **3**, 107-113 (1972).

[17] R. Matull, R. A. Rupp, *J. Phys. D: Appl. Phys.* **21**, 1556-1565 (1988).

[18] H. Vormann, G. Weber, S. Kapphan, E. Krätzig, *Solid State Commun.* **40**, 543 (1981).

[19] D. L. Staebler, W. J. Burke, W. Phillips, J. J. Amodei, *Appl. Phys. Lett.* **26**, 182-184 (1975).

[20] R. Müller, M. T. Santos, L. Arizmendi, J. M. Cabrera, *J. Phys. D: Appl. Phys.* **27**, 241-246 (1994).

[21] V. Leyva, G. A. Rakuljic, B. O'Conner, *Appl. Phys. Lett.* **65**, 1079-1081 (1994).

[22] V. M. Rudyak, *Soviet Physics Uspekhi* **13**, 461-479 (1971).

[23] V. I. Kovalevich, L. A. Shuvalov, T. R. Volk, *Phys. Stat. Sol. (a)* **45**, 249-252 (1978).

[24] F. Micheron, J. C. Trotier, *Ferroelectrics* **8**, 441-442 (1974).

[25] F. Micheron, G. Bismuth, *Appl. Phys. Lett.* **20**, 79-81 (1972).

[26] F. Micheron, G. Bismuth, *Appl. Phys. Lett.* **23**, 71-72 (1973).

[27] J. B. Thaxter, M. Kestigian, *Appl. Opt.* **13**, 913-924 (1974).

[28] Y. Qiao, S. Orlov, D. Psaltis, R. R. Neurgaonkar, *Opt. Lett.* **18**, 1004-1006 (1993).

[29] R. S. Cudney, J. Fousek, M. Zgonik, P. Günter, M. H. Garrett, D. Rytz, *Appl. Phys. Lett.* **63**, 3399-3401 (1993).

[30] W. D. Smith, C. E. Land, *Appl. Phys. Lett.* **20**, 169-171 (1972).

[31] F. Kahmann, R. Pankrath, R. A. Rupp, *Opt. Comm.* **107**, 6-10 (1994).

[32] F. Kahmann, R. Matull, R. A. Rupp, J. Seglins, *Europhys. Lett.* **13**, 405 (1990).

[33] M. Horowitz, A. Bekker, B. Fischer, *Appl. Phys. Lett.* **62**, 2619-2621 (1993).

[34] M. Horowitz, A. Bekker, B. Fischer, *Opt. Lett.* **18**, 1964-1966 (1993).

Chapter Two

Ferroelectric Materials

2.1 Introduction

Fixing has been most thoroughly studied in three common photorefractive ferroelectrics: $LiNbO_3$, SBN:75 and $BaTiO_3$. Samples doped to maximize the density of ionized donors exhibit dramatic photorefractive responses. In addition, they display a broad range of optical and ferroelectric properties, which is responsible for the rich diversity of fixing phenomena reported. The two main classes of fixing are based on (1) the drift of hydrogen impurities and (2) the switching of the spontaneous polarization. Some defining material properties of relevance to these fixing techniques will be highlighted in this chapter.

2.2 Material Properties of Photoferroelectrics

$LiNbO_3$ is the primary material displaying the ionic drift thermal fixing mechanism. Photorefractive charge transport in lithium niobate is dominated by the photovoltaic effect [1]. Photovoltaic fields can exceed 100 $kVcm^{-1}$. Lithium niobate possesses an extremely large coercive field (3 10^5 V cm^{-1}) [2] and spontaneous polarization (70 $\mu C\ cm^{-2}$) [3] . It

exhibits a second order ferroelectric-paraelectric phase transition at the Curie temperature of 1200 °C, so the domain structure is relatively stable even at elevated temperatures. Therefore, the low frequency dielectric constant is relatively small at room temperature (ε_{33} = 32). Lithium niobate belongs to the 3m symmetry class, with two orientations of the spontaneous polarization (±180°) [3].

The perovskite $BaTiO_3$ belongs to the 4mm symmetry class and undergoes three successive first order ferroelectric phase transitions at 120, 5 and -90 °C. It possesses 4 possible orientations of polarization (±90°, ±180°) and a strong electrooptic effect ($r_{42} \approx$ 1600 pm V^{-1}) at room temperature. In contrast to $LiNbO_3$, it has a large low frequency dielectric constant, ε_{33} = 3600 [3].

SBN was first identified as a ferroelectric by Francombe [4]. It belongs to the 4mm symmetry class but exhibits a disordered tungsten bronze structure [5]. SBN:75 is highly electrooptic ($r_{33} \approx$ 1400 pm V^{-1}) with only two allowed spontaneous polarization directions (±180°). The remnant polarization is 15 to 25 μC cm^{-2}. The large low frequency dielectric constant (ε_{33} = 3400) reduces the limiting space charge field (equation 1.10), so the net photorefractive space charge field is typically less than 1 kV cm^{-1}. The optical quality of SBN generally suffers from growth striations, while $LiNbO_3$ and $BaTiO_3$ possess relatively good optical quality.

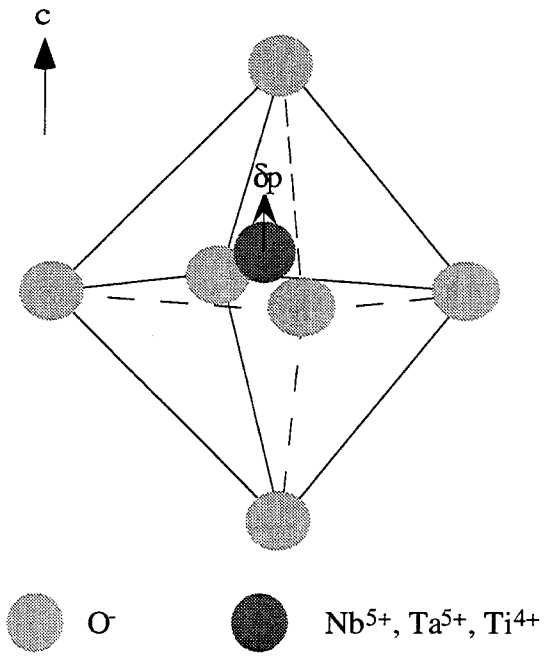

Figure 2.1: Octahedral cage surrounding the transition metal ion, a characteristic unit of ferroelectric oxides. The spatially varying space charge field repolarizes the lattice, introducing a perturbation δp in the local polarization.

SBN:75 is a relaxor [6, 7] ferroelectric characterized by a diffuse phase transition and a low coercive field (of the order of 1 kV cm^{-1}). Microdomains of polar phase exist above T_c, while below T_c microdomains coalesce into macrodomains. The tungsten bronze structure of SBN exhibits disorder in the occupancy of Ba and Sr along the five-fold and four-fold tunnels in the structure [8]. These microscopic compositional fluctuations induce local strain fields which cause a diffuse phase transition. That is, the dielectric constant shows a pronounced broadening at the Curie temperature, as each small micro-polar region has a different T_c.

In the ferroelectric phase, the Nb^{5+}, Sr^{2+} and Ba^{2+} ions occupy one of two stable positions along the c axis (figure 2.1). In the paraelectric phase the Nb, Sr, and Ba ions are centrally located between the two stable positions [9]. A ferroelectric domain consists of a region of homogeneous polarization or coherent displacement of these ions. The energy barrier separating the two equivalent polarization orientations scales with the volume of the microscopic domain, so a typical microdomain of characteristic length on the order of 10 nm thermally fluctuates between polarization states, analogous to a superparaelectric [8]. These thermal fluctuations are believed to freeze out as competing interactions (ferroelectric and antiferroelectric ordering) frustrate the fluctuations. One implication of these glassy properties is an enhanced domain grating lifetime below the freezing temperature.

2.3 Photoferroelectric Phenomena

Fixing techniques encompass several photoferroelectric phenomena in addition to the photorefractive effect [10]. Some relevant examples are photoassisted domain switching and the photodomain effect. These phenomena occur in a special class of ferroelectrics which are also photoconductive, hence the term photoferroelectric. These materials share several properties in common with semiconductors (e.g. optically excitable impurity centers), yet are distinct from semiconductors because of their relatively low values of electronic mobility (~ 1 $cm^2\ s^{-1}\ V^{-1}$) and relatively large band gaps (> 3 eV).

Photoferroelectric phenomena are dealt with theoretically by including the electronic and lattice contributions to the thermodynamic free energy. By minimizing this free energy, the equilibrium configuration of the system can be determined. The effect of optical

illumination on the ferroelectric properties, such as the spontaneous polarization, Curie temperature and domain structure, can then be predicted [10]. Needless to say, the expression for the free energy is extremely complicated [3] and is still a topic of research. Qualitatively, optically excited electrons partially screen the Coulomb interaction among lattice ions, from which the long range ferroelectric order originates.

Numerous observations of photoferroelectric phenomena have been reported in the literature. For instance, the external electric fields required to pole and depole SBN decrease under illumination [11]. Accordingly, light increases the number of Barkhausen pulses [12, 13] observed in the ferroelectric SbSI [14] under applied fields. These pulses are current transients measured across the crystal as domains invert, which are described in detail in chapter six. The kinetics of domain nucleation and growth can be deduced [15] from the shape, duration, amplitude and number of these current pulses. This phenomenon, in which light reduces the coercive field, is called photoassisted domain switching.

Uniform illumination alters the ferroelectric structure in the absence of external fields. For instance, light reduces the tetragonal to cubic phase transition temperature by 2.6 ^{o}C in $BaTiO_3$ [16]. Illumination of SbSI at a wavelength of strong optical absorption accelerates the transition from a monodomain to a polydomain state [17]. This latter phenomenon is called the photodomain effect and is attributed to screening of the ferroelectric polarization by nonequilibrium, optically excited carriers.

The photorefractive effect discussed in chapter one is perhaps the most familiar example of a photoferroelectric effect. In the case of a ferroelectric oxide, as represented in figure 2.1, a space charge field directed along the c axis perturbs the position of the transition metal ion within the oxygen octahedral cage, introducing a polarization perturbation δp. The position of this ion along the c axis contributes to the remnant polarization, so there is a close relationship between the space charge fields and the magnitude and sign of the unit cell polarization. This polarization perturbation alters the index of refraction by typically 10^{-5} to 10^{-3} through the electrooptic effect.

2.4 Summary

Fixing techniques in ferroelectrics encompass a broad range of photoferroelectric phenomenon. Simplified models to describe the dielectric response of these materials upon illumination have been developed. These models assist in a qualitative understanding of domain hysteresis fixing, but quantitative predictions of these highly nonlinear dielectrics are still highly speculative.

References for chapter two

[1] B. I. Sturman, V. M. Fridkin, *The Photovoltaic and Photorefractive Effects in Noncentrosymmetric Materials*. G. W. Taylor, Ed., Ferroelectricity and Related Phenomena (Gordon and Breach, Philadelphia, 1992), vol. 8.

[2] S. H. Wemple, M. Di Domenico, *Appl. Phys. Lett.* **12**, 209 (1968).

[3] M. E. Lines, A. M. Glass, *Principles and Applications of Ferroelectrics and Related Materials*. (Clarendon Press, Oxford, 1977).

[4] M. H. Francombe, *Acta Cryst.* **13**, 131 (1960).

[5] L. Bursill, P. Lin, *Philos. Mag. B* **54**, 157 (1986).

[6] A. S. Bhalla, R. Guo, L. E. Cross, G. Burns, F. H. Dacol, R. R. Neurgaonkar, *J. Appl. Phys.* **71**, 5591 (1992).

[7] W. H. Huang, D. Viehland, R. R. Neurgaonkar, *J. Appl. Phys.* **76**, 490-496 (1994).

[8] L. E. Cross, *Ferroelectrics* **76**, 241 (1987).

[9] P. B. Jamieson, S. C. Abrahams, J. L. Bernstein, *J. Chem. Phys.* **48**, 5048 (1968).

[10] V. M. Fridkin, *Photoferroelectrics*. M. Cardona, P. Fuldeand H.-J. Queisser, Eds., Springer Series in Solid State Sciences (Springer-Verlag, Berlin, 1979), vol. 9.

[11] F. Kahmann, R. Pankrath, R. A. Rupp, *Opt. Comm.* **107**, 6-10 (1994).

[12] H. Barkhausen, *Physikalische Zeitschrift* **20**, 401 (1919).

[13] V. M. Rudyak, *Soviet Physics Uspekhi* **13**, 461-479 (1971).

[14] A. A. Bogomolov, V. V. Ivanov, V. M. Rudyak, *Sov. Phys.-Cryst.* **14**, 894-896 (1970).

[15] A. G. Chynoweth, *Phys. Rev.* **110**, 1316-1332 (1958).

[16] T. R. Bolk, A. A. Grekov, N. A. Kosonogov, A. I. Rodin, V. M. Fridkin, *Sov. Phys.-Cryst.* **16**, 198-200 (1971).

[17] V. M. Fridkin, I. I. Groshik, V. A. Lakhovizkaya, M. P. Mikhailov, V. N. Nosov, *Appl. Phys. Lett.* **10**, 354-356 (1967).

Chapter Three

Ferroelectric Domain Gratings

3.1 Introduction

Photoferroelectric phenomena encompass a broad range of effects which induce structural and index of refraction changes in these materials. These effects are difficult to model quantitatively from first principles, so realistic simplifying approximations are adopted. In the context of optical diffraction from domain holograms, the linear electrooptic contribution to the index change is dominant and the domains are treated as ideal dipoles of homogeneous polarization. A simple theoretical framework for the optical properties of domain gratings will be developed based on these two approximations.

3.2 Theory of the Electrooptic Effect

Photorefractive diffraction gratings are produced by a modulated space charge field that alters the index of refraction through the electrooptic effect. The index change created by the total polarization field may be expressed as a linear electrooptic effect or equivalently as a quadratic electrooptic effect "biased" by the remnant polarization [1]. The tensor relation for the Fourier component of the index change at the grating vector $\mathbf{k}_g$ is:

$$\Delta\left(\frac{1}{n^2}\right)_{ij}(\mathbf{k}_g) = 2\, g_{ijkl}\,(P_o)_k\,\Delta P(\mathbf{k}_g)_l \quad , \qquad 3.1$$

where g_{ijkl} is the quadratic electrooptic tensor, P_o is the average remnant polarization and $\Delta P(\mathbf{k}_g)$ is the Fourier component of the static ($\omega = 0$) polarization modulation at $\mathbf{k}_g$. This polarization modulation may be generated by a static space charge field $\Delta E(\mathbf{k}_g)$, for instance. The modulation of the polarization $\Delta P(\mathbf{k}_g)$ is expressed as the Fourier transform of the spatial variation of polarization $\Delta P(\mathbf{r})$:

$$\Delta P(\mathbf{k}) = \frac{1}{(2\pi)^{3/2}} \int_{-\infty}^{\infty} \Delta P(\mathbf{r})\, e^{-i\,\mathbf{k}\cdot\mathbf{r}}\, d\mathbf{r}\ , \qquad 3.2$$

where the polarization perturbation includes three contributions:

$$\Delta P(\mathbf{r}) = \Delta P^{\text{optical excitation}}(\mathbf{r}) + \Delta P^{\text{charge transport}}(\mathbf{r}) + \Delta P^{\text{ferroelectric distortion}}(\mathbf{r})\,. \qquad 3.3$$

These three terms may be estimated analytically from:

$$\Delta P(\mathbf{r}) = \sum_{i}^{N} \int (\mathbf{R}_i + \mathbf{r}' - \mathbf{r})\, \Delta\rho_i\, (\mathbf{R}_i + \mathbf{r}' - \mathbf{r})\ d\mathbf{r}'\ , \qquad 3.4$$

where the sum is over the N lattice sites i, $\mathbf{r}'$ is the position relative to the address of the ith lattice site $\mathbf{R}_i$, and ρ_i is the total charge density of the atoms associated with the lattice site i.

The somewhat arbitrary decomposition of equation 3.3 makes three contributions to index changes explicit. The first term on the right represents the change in dipole moment of donors and acceptors upon optical excitation. The second term represents the change in polarization arising from both electron transport (due to drift, diffusion, pyroelectric or photovoltaic mechanisms producing photorefractive space charge fields) and ionic transport (typically due to drift induced by electronic space charge fields). The charges undergo

transport between distant lattice sites (a distance on the order of the grating spacing, typically ~ μm). The third term represents the change in lattice polarization arising from the displacement of ions. In this case the center of charge is displaced only slightly within the unit cell from the unperturbed position (typically << 1 Å). The electric dipole generated by the first two terms polarizes the lattice through this third term. Note that the polarization is understood to be spatially averaged on a scale much larger than a unit cell, yet smaller than the optical wavelength of interest.

The standard electrooptic effect described by equation 3.1 treats only that polarization perturbation corresponding to the third term of equation 3.3. That is, measurements of the electrooptic effect are performed by applying an external electric field to the crystal and measuring the resulting net index change. The external electric field will modify the crystalline polarization by slightly displacing the positions of ions. As long as negligible current from the external source flows through the crystal, the drift of electrons across the crystal will also be negligible. Therefore, the electrooptic effect will not include the direct index changes resulting from electron and ion optical excitation or drift; namely, the first two terms of equation 3.3.

The electrooptic effect describes the interaction of a low frequency electric field E^{Ω} and an optical field E^{ω}, generating an optical polarization $\Delta P^{\omega,\Omega}$ that is shifted in phase relative to the incident optical wave:

$$\Delta P^{\omega,\Omega} = \chi^{\omega,\Omega} E^{\omega} E^{\Omega}. \qquad 3.5$$

The proportionality constant is a nonlinear susceptibility $\chi^{\omega,\Omega}$ defined as

$$\chi^{\omega,\Omega} = \left[\frac{\partial^2 P^{\omega,\Omega}}{\partial E^{\omega} \partial E^{\Omega}} \right]_{E_0^{\omega}, E_0^{\Omega}} . \qquad 3.6$$

To determine the coefficient $\chi^{\omega,\Omega}$ responsible for the linear electrooptic effect, the changes ΔP due to optical frequency electric fields E^{ω} must be considered. Electron clouds in the vicinity of ion cores will feel very strong attractive Coulombic forces with the nucleus. These electron orbitals will be weakly perturbed by the optical field, which is typically much weaker than the ion core attraction. Electrons which spend a greater fraction of their time far from the core and experience a screened core potential will exhibit stronger polarizability at optical frequencies.

Bonds can be separated into two archetypes: purely covalent or ionic [2]. The character of bonds between elements with different electronegativities falls between these two extremes. The stronger the covalent character of the bond, the greater fraction of the time the electron will be found between the ion cores where the core attraction is significantly weaker. Therefore, covalent bonding orbitals are more highly polarizable than ionic bonding orbitals under moderate optical fields. A familiar example is that purely covalent crystals (i. e., diamond) have larger indices of refraction than ionic crystals (i. e., NaCl).

The nonlinear optical properties of the ferroelectric niobates arise from the distorted NbO_6 octahedron [1]. The contributions to the linear and nonlinear optical polarizabilities can be determined by decomposing the crystal bond-by-bond into individual dipole radiators. The highly ionic Li-O bond susceptibility [3] makes a negligible contribution, since the valence electrons are tightly bound to the oxygen. For $LiNbO_3$ and SBN, it is a good approximation to consider only the Nb-O bond contribution to the nonlinear polarizability (similarly for $BaTiO_3$ and $LiTaO_3$, the dominant contribution to the susceptibility arises from the covalent Ti-O and Ta-O bonds [3]). This contribution to the electrooptic effect can

be estimated by considering the dependence of the linear optical susceptibility of the Nb-O bond on rotation and stretch [4, 5].

$$p_t(t) = 2\beta^{(1)} e(t)$$

$$p_1(t) = \beta^{(1)} e(t) + \beta^{(2)} e^2(t) \qquad p_2(t) = \beta^{(1)} e(t) - \beta^{(2)} e^2(t)$$

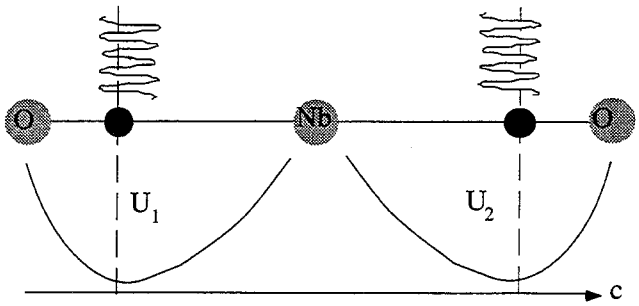

(a) inversion symmetry

$$p_t(t) = \left(\alpha^{(1)} + \gamma^{(1)}\right) e(t) + \left(\alpha^{(2)} - \gamma^{(2)}\right) e^2(t)$$

$$p_1(t) = \alpha^{(1)} e(t) + \alpha^{(2)} e^2(t) \qquad p_2(t) = \gamma^{(1)} e(t) - \gamma^{(2)} e^2(t)$$

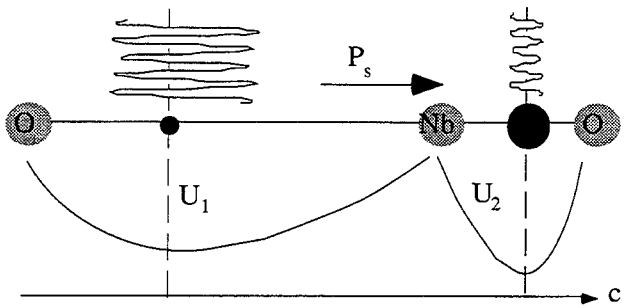

(b) no inversion symmetry

Figure 3.1: Microscopic model of the origin of nonlinear optical susceptibility in typical ferroelectric oxides.

When the crystal is in the paraelectric phase, the niobium ion is equidistant from the oxygen atoms along the c axis (figure 3.1). The nonlinear polarizability from these two bonds is the vector sum of the individual bonds. As indicated in figure 3.1(a), despite the *individual*

bond polarizability dependence on both even and odd powers of the optical field e(t), only the even order terms to the *total* nonlinear polarizability p_t remain. In contrast, in the ferroelectric phase (figure 3.1(b)), the Nb ionic displacement breaks the symmetry of the two bonds along the c axis, so the total polarizability depends on both even and odd powers of the electric field. The dependence of p_t on the square of the field $e^2(t)$ is manifest in the linear electrooptic effect and second harmonic generation.

From this microscopic viewpoint, the displacement of the Nb ion along the c axis changes the polarization $\Delta P(\mathbf{k}_g)$ and induces an index change through the electrooptic effect. Note that the distortion of this Nb-O bond length also produces the ferroelectric polarization in materials such as $LiNbO_3$ and SBN. Thus, the ferroelectric and nonlinear optical properties are intimately related. The decomposition of equation 3.3 on the atomic bonding level links the third term, describing ferroelectric distortion, to the electrooptic effect in these materials. This association is fundamental to understanding the relationship between nonlinear optical and ferroelectric properties, and as will be discussed later, the distinction between dynamic and remnant ferroelectric domain gratings.

The origins of index gratings induced by internal space charge fields are microscopically more complicated than the phenomenon described by the electrooptic effect, in which external fields rather than space charge densities modulate the index of refraction. Indeed, from equation 3.3 there are two other contributions. The first term represents the change of dipole of the ions upon optical excitation, the excited state dipole moment being an example. This makes a negligible contribution to the steady state index change because the density of electrons in the conduction band at any instant in time is very small relative to the cumulative charge redistribution that occurs upon the generation of steady state photorefractive space charge fields. This is true at moderate optical intensities ($< kW\ cm^{-2}$) in the highly resistive ferroelectric oxides described here.

The second term describes the change in polarization due to the optical redistribution of electrons among deep traps. By definition, since these photorefractive traps are deep, the electrons are strongly bound to their host atom, and as a consequence we assume that these trapping sites make a small contribution to the nonlinear susceptibility relative to the highly covalent Nb-O bonds. Note that in a strained, centrosymmetric crystal this contribution can play an important role through a Jahn-Teller distortion [6]. However, the materials under consideration possess a strong linear electrooptic effect, so the second term is neglected. The third term also has a contribution from the motion of ions (such as protons in the case of $LiNbO_3$ thermal fixing) to new lattice sites by drift induced by electronic space charge fields. These ions compensate the electronic grating to reduce the net internal field.

The first two contributions of equation 3.3 polarize their surroundings and perturb the lattice polarization through the third term to produce an index change. In effect, the photogenerated space charge fields and ionic space charge fields can be treated as *external* fields, which modify the index of refraction through the standard electrooptic effect. This justifies a description of the index change arising from a modulation of the spontaneous polarization in terms of the linear electrooptic effect.

3.3 Ferroelectric Domain Structure

The ferroelectric domain structure is intimately linked to the nonlinear optical properties of the material. From the microscopic description of the electrooptic effect, it is apparent that an electrooptic grating corresponds to a modulation of the ferroelectric polarization. As described latter, this modulation may correspond not only to small perturbations of the Nb-O bond length, but to actual switching between the two stable polarization orientations.

From electrostatic considerations, the potential and field of a polarized object is equivalent to that field produced by a bound volume charge density ρ_b:

$$\rho_b = - \nabla \cdot \mathbf{P}, \qquad 3.7$$

and a bound surface charge density σ_b

$$\sigma_b = \mathbf{P} \cdot \hat{\mathbf{n}}, \qquad 3.8$$

where $\mathbf{P}(r)$ is the macroscopic polarization averaged over a volume much larger than a unit cell, and $\hat{\mathbf{n}}$ is the unit normal vector to the surface of the crystal. The bound charge can not be removed from a domain interface (where $\mathbf{P}$ changes); it is permanently attached to the ions responsible for the spontaneous polarization. In contrast to this bound charge, free charge can be optically excited and redistributed, producing photorefractive space charge fields, for instance. Note that this free charge spends the great majority of its time trapped, since the recombination time (~ 10 ps) in oxide ferroelectrics such as SBN is extremely short (in this sense, the term *free* charge is misleading). If sufficient mobile charge is available, the bound charge is compensated by an equal and opposite free charge density ρ_f and surface charge density σ_f. Compensating charge is electrostatically trapped at domain walls for which the divergence of the polarization $\mathbf{P}$ is non-zero (i.e. head-to-head rather than antiparallel).

Compensating electric charge plays an important role in minimizing depolarization fields at domain walls in ferroelectrics, analogous to the closure requirements of ferromagnetic domains. To analyze charge compensation at domain walls consider the simplest case of a normal ferroelectric phase in which there are only two allowed polarization directions (0 and 180 degrees to the c axis). The polarization within an individual domain is assumed to

be homogeneous. Figure 3.2(a) illustrates an idealized volume grating configuration in which the grating vector is parallel to the c axis. The free carrier density required to compensate the non-zero divergence of the polarization for a domain grating composed of head-to-head domain walls is given by

$$N_{comp} = \frac{\Delta P}{q \Lambda_g} \qquad 3.9$$

and the carrier density required to produce a field equal to the coercive field is

$$N_{coercive} = \frac{2 \pi \varepsilon E_{coercive}}{q \Lambda_g} . \qquad 3.10$$

Λ_g is the grating period, q is the charge of an electron, and ε is the dielectric permittivity. For grating periods of 1 micron, P_s equal to 25 $\mu C\ cm^{-2}$ and $E_{coercive}$ equal to 1 $kV\ cm^{-1}$ (typical for SBN:75), the compensating charge density required on the domain walls for bipolar modulation ($\Delta P = 2\ P_s$) is $N_{comp} \sim 2.5 \times 10^{18}\ cm^{-3}$, and the coercive charge density is $10^{17}\ cm^{-3}$. Therefore, significant charge densities are required to completely screen depolarization fields at head-to-head domain walls and canted domain walls making small angles with the c axis. Thermally ionized shallow acceptors and illumination in the intrinsic or extrinsic bands contribute to these screening fields. In general, the average modulation ΔP may be much smaller than the spontaneous polarization, which reduces the compensating charge requirements described by equation 3.9.

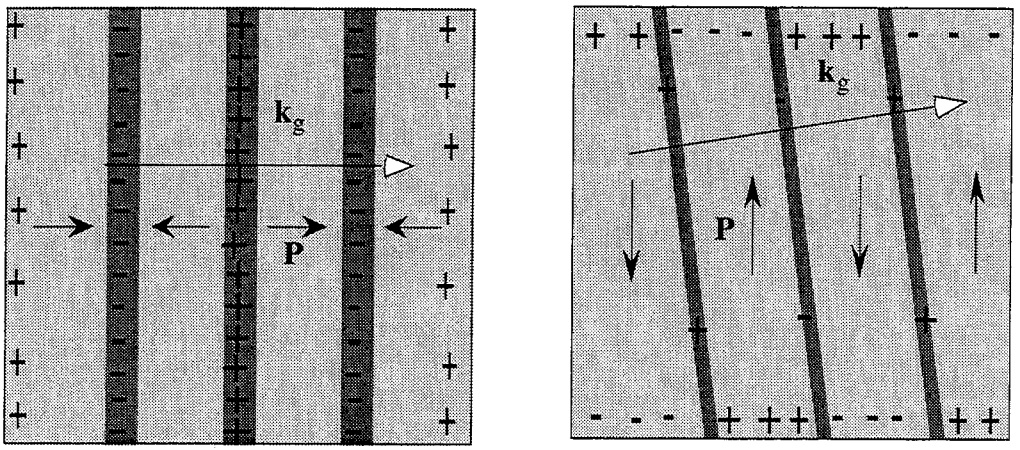

(a) (b)

Figure 3.2: (a) Head-to-head and (b) canted domain wall configuration.

The divergence of the polarization at a domain wall is reduced by a factor of sin θ for canted domain walls, where θ is the angle between the direction of spontaneous polarization and the domain interface (figure 3.2(b)). Therefore, for θ = 0, no charge is required at the wall for perfect bipolar modulation of the spontaneous polarization. These antiparallel walls are expected to be relatively stable. For this domain microstructure, charge compensation occurs only at the crystal c faces. These electrostatic considerations influence the shape and size of individual ferroelectric domains. Domains in SBN are dagger-like in shape and oriented along the c axis, which reduces depolarization fields at the head-to-head domain interface. A grating composed of these dagger-like domains is depicted graphically in figure 3.3.

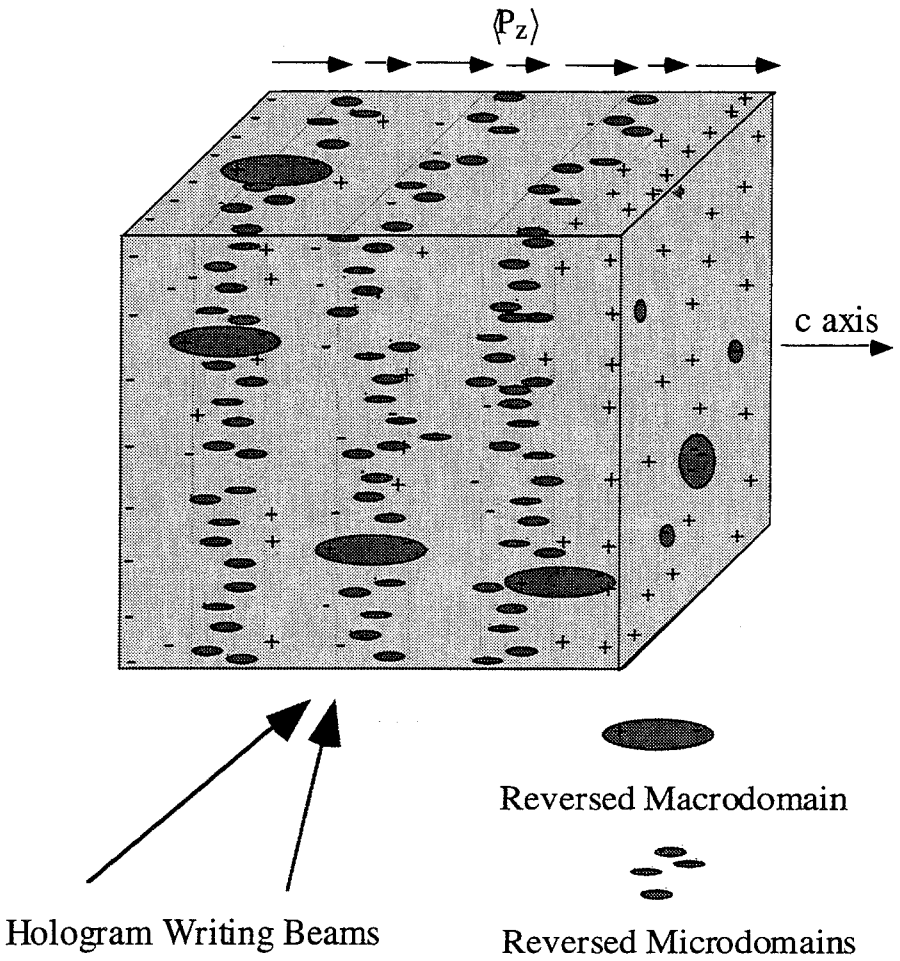

Figure 3.3. Model of glassy domain grating consisting of inverted microdomains and macrodomains in regions of negative space charge field.

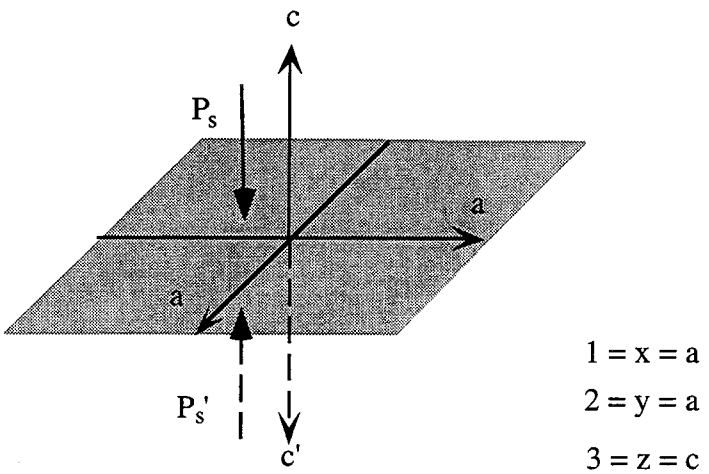

Figure 3.4: Shaded box indicates reflection plane through which spontaneous polarization is reversed upon domain inversion.

3.4 Transformation of Nonlinear Optical Tensor Under Domain Inversion

The signs of the second order nonlinear optical tensor elements d_{ijk} depend on the orientation of the ferroelectric domain. By spatially modulating the ferroelectric polarization, the nonlinear coefficients are also modulated. In general, the inversion of a third rank tensor is not a trivial undertaking. Therefore, for illustrative purposes, consider the relevant example of SBN with nonzero elements $d_{33} = d_{333}$, $d_{31} = d_{311}$ and $d_{15} = d_{131} = d_{113}$. The orientation of the crystalline axes is illustrated in figure 3.4. The nonlinear media is assumed to be lossless in the wavelength region of interest to satisfy Kleinman's conjecture [7] . Before inversion, the induced optical polarizability at the second harmonic is:

$$P_3 = d_{333} E_3 E_3 + d_{311} E_1 E_1 \qquad 3.11$$

$$P_1 = d_{113} E_1 E_3 + d_{131} E_3 E_1 \ . \qquad 3.12$$

If the ferroelectric domain is inverted, the induced optical polarization and field along the c axis changes sign, because these quantities are now referenced to a new coordinate system: $P_3 \rightarrow -P_3$, $P_1 \rightarrow P_1$, $E_3 \rightarrow -E_3$, $E_1 \rightarrow E_1$. Substituting this change of variables into 3.11 and 3.12, the optical polarizability at the second harmonic for an inverted domain is:

$$-P_3 = d'_{333}\ (-E_3)(-E_3) + d'_{311}\ E_1 E_1 \qquad 3.13$$

$$P_1 = d'_{113}\ E_1 (-E_3) + d'_{131}\ (-E_3) E_1 \quad . \qquad 3.14$$

The primes on the nonlinear coefficients d_{ijk} indicate that the domain is inverted. Rearranging coefficients, equations 3.11 and 3.12 become:

$$P_3 = \left(-d'_{333}\right) E_3 E_3 + \left(-d'_{311}\right) E_1 E_1 \qquad 3.15$$

$$P_1 = \left(-d'_{113}\right) E_1 E_3 + \left(-d'_{131}\right) E_3 E_1 \quad . \qquad 3.16$$

By comparing equations 3.11, 3.15 and 3.12 and 3.16, it is apparent that domain inversion changes the sign of all three nonlinear optical coefficients d_{33}, d_{31}, d_{15}. This fact will be used in chapter seven to select the proper crystalline orientation for optimal second harmonic generation.

3.5 Summary

The modulation of the spontaneous polarization in domain gratings modulates both the index of refraction through the linear electrooptic effect and the nonlinear optical susceptibility. This provides two methods of studying and utilizing this optically induced

microstructure: optical diffraction and quasi-phase matched second harmonic generation. This first application, ferroelectric hysteresis fixing, is described in chapter four.

References for chapter three

[1] M. DiDomenico Jr., S. H. Wemple, *J. Appl. Phys.* **40**, 720 (1969).

[2] J. C. Phillips, *Bonds and Bands in Semiconductors*. A. M. Alperand, A. S. Nowick, Eds., Materials Science and Technology (Academic Press, New York, 1973).

[3] C. R. Jeggo, G. D. Boyd, *J. Appl. Phys.* **41**, 2741-2743 (1970).

[4] C. Shih, A. Yariv, *Phys. Rev. Lett.* **44**, 281-284 (1980).

[5] C. Shih, A. Yariv, *J. Phys. C: Solid State Phys.* **15**, 825-846 (1982).

[6] R. Hofmeister, A. Yariv, S. Yagi, A. Agranat, *Phys. Rev. Lett.* **69**, 1459-1462 (1992).

[7] D. A. Kleinman, *Phys. Rev.* **126**, 1977 (1962).

Chapter Four

Ferroelectric Hysteresis Fixing of Volume Holograms

4.1 Introduction

This chapter will focus on hologram fixing based on ferroelectric domain reversal. This fixing process is the manifestation of hysteresis in the electrooptic effect near the ferroelectric/paraelectric phase transition. This is demonstrated in SBN:75, at a temperature 20° C below the phase transition. First, high intensity fixing using optical heating to assist the domain switching process is described [1, 2]. Next, short exposure fixing using a dark development stage is demonstrated [3]. The lifetimes of these remnant domain gratings are found to be highly temperature dependent.

4.2 High Intensity Fixing

The crystals used in this experiment are Cr doped SBN:75 single crystals, 6x6x6 mm, grown at the Rockwell International Science Center. Sample A has facets cut normal to the principal axes, whereas the axes of sample B are rotated 45° about the y axis in the x-c plane. The crystals are poled by application of a dc electric field of 5 kV cm^{-1} while uniformly heated to 80 °C in a high dielectric-strength oil bath. With the field on, the samples are cooled at a rate of 0.5 °C min^{-1} to 25 °C. The poling field is then removed.

Note that the 45° cut of sample B makes the task of poling difficult; hence, the diffraction efficiencies for this sample are very small.

The experimental setup is depicted in Figure 4.1. During the writing process, A_1 and A_2 are the signal and reference beams, respectively. During the coherent reconstruction with A_2, B_1 and B_2 are the reconstructed signal and remnant reference beams, respectively. Since the holograms are sufficiently weak, the diffraction efficiency is defined as B_1/B_2, to include reflection and absorption losses (absorption coefficient 1.9 cm^{-1}). The transmission holograms are written in the image plane at 488 nm, with equal angles of incidence ($\theta = 16^o$). The experiments are performed at or near room temperature (25 - 30 °C) in the ferroelectric phase.

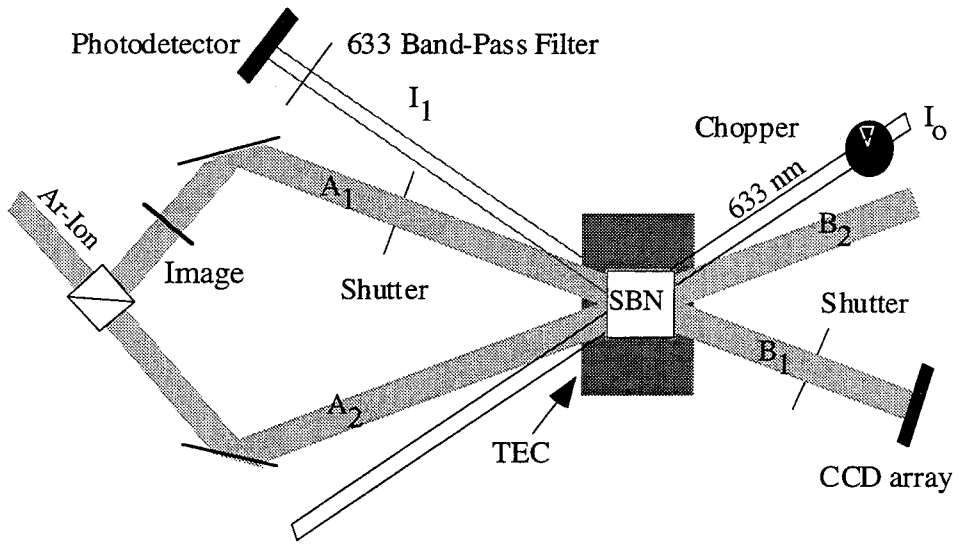

Figure 4.1: Experimental setup for domain fixing.

The fixing process occurs simultaneously with the dynamic hologram writing process; no thermal development cycle or electrical fixing pulse is required. However, increases in incident intensity, temperature (while well below $T_c = 56$ °C), or write time all tend to enhance the diffraction efficiency of the fixed hologram. The hologram is composed of a

dynamic component, with a characteristically fast response time, and a fixed component, with a lifetime that is several orders of magnitude larger than the dynamic grating. This dependence of relaxation rate on exposure level was first reported by Thaxter and Kestigian [4], who measured a fixed component with a lifetime of several minutes. A significant fixed component is obtained simply by writing holograms with an incident intensity greater than 1 W cm^{-2} for 2 minutes or more, an exposure in excess of 100 J cm^{-2}. For a total intensity of signal and reference beams of 100 mW cm^{-2}, only a significant dynamic grating is present. By increasing the intensity to 4 W cm^{-2}, a significant remnant hologram is recorded automatically.

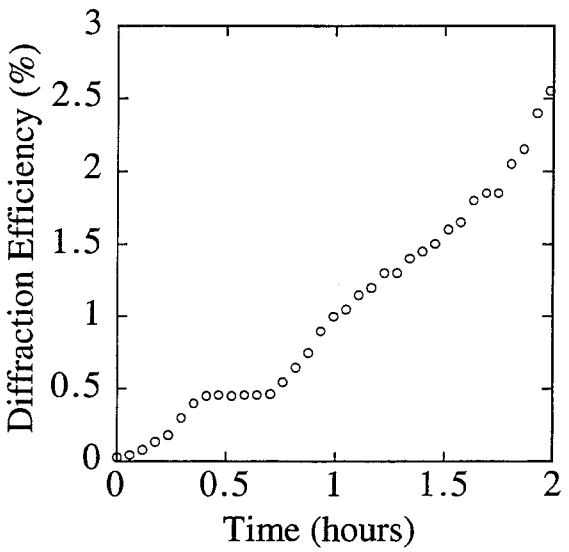

Figure 4.2: Diffraction efficiency during high intensity writing process.

The diffraction efficiency of the remnant hologram grows by a factor of 25 from the initial value of 0.1 % during the writing process of 2 hours (figure 4.2). While it is exceedingly difficult to maintain fringe stability during these long write times, the diffraction efficiency

increases for approximately 20 hours, until saturation occurs at a maximum diffraction efficiency of 3%. This long exposure optically fatigues the crystal by increasing the volume of charge compensated microdomains. This reduces the viscosity of the dipoles so domains will subsequently align more rapidly and readily under the influence of the space charge field. Response times of hours are uncharacteristically slow for photorefractive phenomenon and suggest the presence of a slow domain relaxation phenomenon.

The monatonic increase in fixed diffraction efficiency occurs because domains continuously orient to produce bound charge in opposition to the electronic space charge. The net internal field, arising from sum of the free and bound charge, is then reduced. Since the spatially modulated charge density decreases, charge transport by diffusion is also reduced. Diffusion limits the build-up of space charge for grating periods larger than the Debye screening length, given by:

$$\Lambda_D = \frac{2\pi}{q}\sqrt{\frac{\varepsilon k_B T}{N_d^+}} \quad . \qquad 4.1$$

The space charge field in figure 1.3 attains a maximum for a grating period equal to Λ_D. For SBN:75 Λ_D is of the order of 1 μm. Domain reversal allows the electronic grating to exceed the diffusion limit and reach the limiting space charge value at grating periods greater than the Debye length, given by the curve labeled E_q in figure 1.3. Nevertheless, the typical fixed diffraction efficiency is a modest 3%, because a large fraction of domain reversal is random, which reduces the linear electrooptic coefficients responsible for diffraction.

The hologram written at high exposure levels is automatically fixed during the writing stage. Prior to the curves of figure 4.3, a hologram is recorded for 100 seconds at either 0.1, 1, 2, or 3 W cm^{-2} total incident intensity. Upon readout with the same intensity, the

strength of the remnant hologram is found to increase in proportion to the incident intensity (figure 4.3).

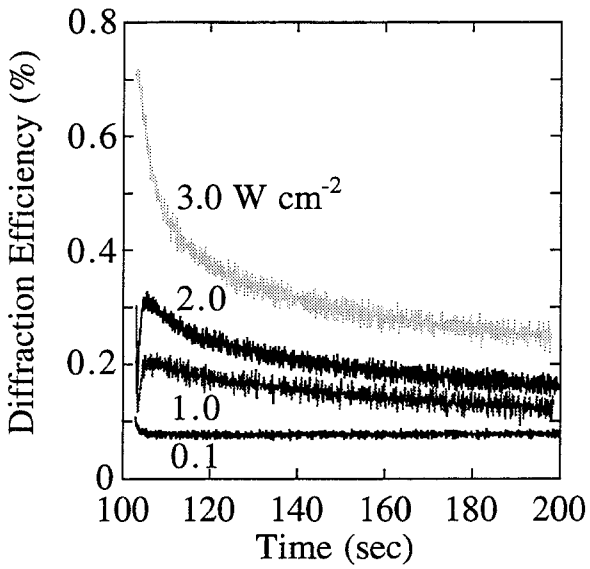

Figure 4.3: Revealing of remnant domain grating following 100 second exposure for writing and readout intensities 0.1, 1, 2, and 3 W cm^{-2}.

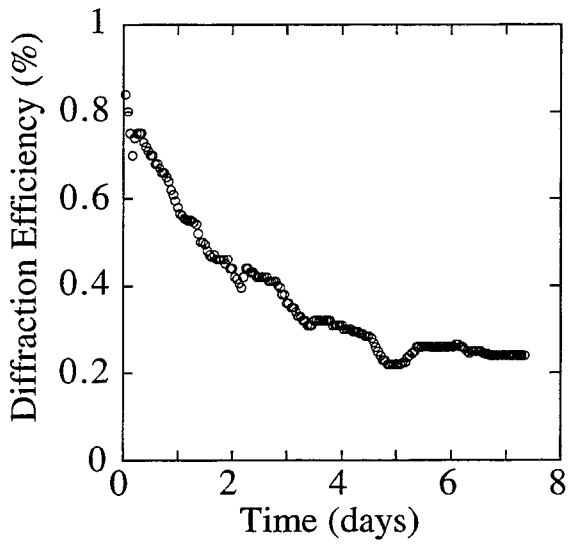

Figure 4.4: Lifetime of remnant domain grating during continuous readout with a high-intensity beam at 488 nm (I = 1 W cm^{-2}).

Figure 4.4 illustrates the long term decay of a fixed hologram written at room temperature with a total intensity of 4 W cm^{-2} for 1 hour. Extrapolating this curve, the hologram is expected to survive at least several hundred days during continuous readout at 25 °C. By cooling the crystal to below 20 °C, the domain grating is permanently frozen-in. The lifetime is enhanced for readout with a weak plane wave, which minimizes undesirable domain reversal due to the accumulation of space charge on the periphery of a focused reference beam and local heating which reduces the polarization viscosity. A fixed page written for 15 minutes has been monitored intermittently for over 1 month without any degradation in image quality.

These high intensity recordings are performed in initially poled crystals. Following a continuous optical exposure for two days, the macroscopic spontaneous polarization as measured from the electrooptic coefficient decreased by a factor of 10. This severe depolarization results from optical exposures on the order of 10^5 J cm^{-2}.

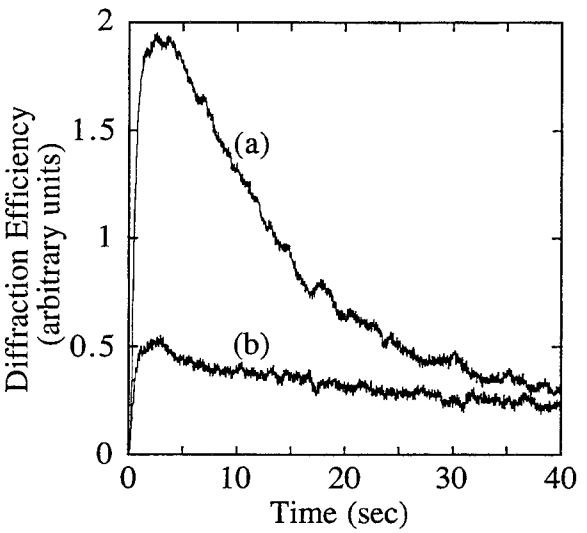

Figure 4.5: Recording of domain grating in canted wall configuration; (a) poled crystal (b) optically depoled crystal following exposure.

Domain gratings may also be optically recorded in the canted wall configuration discussed in reference to figure 3.3(b). This is demonstrated by recording a domain grating at an angle of $\theta = 7$ degrees to the c axis, so the charge compensation requirements at domain walls are significantly reduced. The total diffraction efficiency while writing the grating is illustrated in figure 4.5. Curve (a) illustrates the diffraction efficiency while the first grating was written. Following this recording, the half-wave voltage, which is inversely proportional to the effective linear electrooptic coefficient r_c, increased by a factor of 3 in the region where the hologram was recorded. Thus, the macroscopic polarization in the region of the hologram has decreased by 3. This is the reason why the diffraction efficiency of curve (a) in figure 4.5 decreases after 4 seconds of exposure. A second hologram was subsequently recorded in the same volume and the diffraction efficiency (b) decreased dramatically because of the depolarization of the crystal.

In this canted domain grating configuration, with $\mathbf{k}_g$ nearly perpendicular to c, the crystal rapidly depolarizes in the region of illumination. More rapid depolarization is indeed expected because of the reduced compensating charge requirements for canted domain gratings. By re-poling the crystal with 3 kV cm^{-1} for approximately 1 minute, the crystal is refreshed and a third hologram recorded in the same volume displays the same diffraction efficiency as curve (a). In this geometry the space charge field is nearly perpendicular to the c axis, so the photorefractive space charge fields do not play a central role in domain reversal. These gratings are produced by a combination of optical heating and photoassisted domain reversal.

4.3 Short Exposure Fixing

While high intensities enhance the fixing efficiency, low intensities and short optical exposures can also produce fixed holograms of significant diffraction efficiency if the

recording stage is followed by a dark development stage. The longer the photorefractive space charge field is applied in the dark, the greater the ferroelectric hysteresis or memory. The short exposure hologram fixing technique isolates the role of the space charge field from thermo-optic effects and random depolarization, which play a dominant role in high intensity fixing. Obviously, a fixing technique that significantly depoles the crystal during recording is of little value if multiple holograms are to be stored, because the reduction of the average electrooptic coefficient leads to weak diffraction. The short exposure technique reduces this random depolarization. Nevertheless, the primary utility of this technique is that it provides a means to characterize the domain fixing technique. The dependence of the domain modulation on the photorefractive space charge field alone can be determined.

The amplitude of this periodic space charge field is controlled by interfering two plane waves, each of 50 mW cm^{-2} intensity, for a variable amount of time (1 to 5 seconds). The space charge field amplitude increases with exposure until saturation occurs after 5 seconds. The short exposure is followed by a dark development stage of typically minutes, during which time the domains stabilize in their reversed orientation. The development stage is effective because the space charge fields persist in the dark due to the low dark conductivity, which is verified in separate experiments by monitoring the decay of uniform pyroelectric fields in the dark. Following a dark development stage of 10 minutes, the dynamic polarization grating is erased with a 1 W cm^{-2} non-Bragg matched plane wave (488 or 515 nm) and the remnant diffraction efficiency is monitored with a low intensity, Bragg matched He-Ne probe. This remnant diffraction corresponds to the fixed or remnant domain hologram.

The amplitude of the spatially periodic electric field can be estimated from the measured diffraction efficiency of the grating during Bragg-matched reconstruction. In the symmetric transmission grating configuration with the grating vector $\mathbf{k}_g$ parallel to the c axis, the

amplitude of the net space charge field, for small diffraction efficiencies and small half angle of the writing beams, is from equation 1.20:

$$E_{sc}(\mathbf{k}_g) = \frac{2\,\lambda\, e^{\alpha L/2}\sqrt{\eta(\mathbf{k}_g)}}{\pi\, L\, n_o^3\, r_{33}}\ , \qquad 4.2$$

where $\mathbf{k}_1$ and $\mathbf{k}_2$ are the wave vectors of the signal and reference plane waves in the medium, α is the absorption at the reconstruction wavelength λ in vacuum, L the interaction length between the readout beam and the volume grating, n_o the unperturbed index of refraction of the medium, r_{33} the dominant electrooptic coefficient for SBN:75 and η the Bragg matched diffraction efficiency defined as I_1/I_o, where I_1 and I_o are the intensities of the diffracted and incident He-Ne beams, respectively. The HeNe is used to readout the hologram rather than the Ar-ion because the SBN sample exhibits negligible absorption at red wavelengths, reducing the buildup of fanning noise.

The remnant polarization modulation exhibits a linear dependence on the initial field modulation (figure 4.6(a)). This is expected since the photogenerated field lies in the small field, linear region of the hysteresis loop. The polarization modulation depicted in figure 4.6 is expressed in terms of an equivalent bound charge field to permit a quantitative comparison to the photorefractive space charge field. The fixing efficiency, defined as the ratio of the bound charge field to the initial space charge field, is typically 1%. These light induced domain patterns are produced in the absence of external electric fields or thermal effects, thus providing conclusive evidence that the photogenerated space charge fields *alone* induce the periodicity in the ferroelectric polarization.

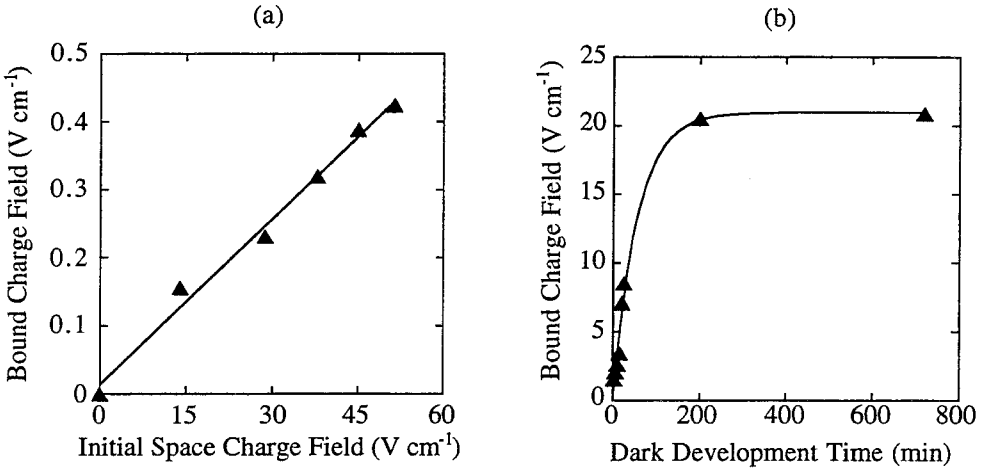

Figure 4.6: Short exposure fixing (a) Dependence of remnant polarization grating (expressed in terms of an equivalent bound charge field) on initial space charge field (b) Dependence of remnant polarization grating on dark development time.

The hysteresis is further enhanced by increasing the time duration of the dark development stage and/or applying an external depoling field during the development stage. For instance, a one second depoling field pulse of 3 kV cm^{-1} applied after the optical exposure increases the fixed diffraction efficiency by a factor of two. Increasing the dark development time from 2 to 200 minutes increases the diffraction efficiency of fixed holograms by more than a factor of 100, as illustrated in figure 4.6(b). For this set of experimental conditions (grating period ≈ 4 μm, T = 25 °C), the remnant polarization modulation saturates at approximately 0.02 % of the spontaneous polarization. These experiments confirm a general characteristic of ferroelectrics: the induced polarization change increases in proportion to the product of the depoling space charge field and the time the field is applied (until the onset of saturation) according to the empirical relationship:

$$\Delta P = \Delta P_o \left[1 - \exp\left(\frac{-E_{ext}\, t}{\beta}\right)\right] . \qquad 4.3$$

A thermodynamic study of glassy domain reversal offers some further interesting conclusions. Although it is conventional to apply Gibb's free energy equilibrium arguments to evaluate the stability of domains, the stable glassy domain configuration may not be the equilibrium configuration. In fact, a non-equilibrium domain grating may be stable below a freezing temperature where the glassy polarization phase is inherently non-ergodic. At these temperatures the viscosity of the dipoles increases dramatically and freezes-in the polarization modulation. Therefore, one experimental approach to evaluate the thermodynamics of this process is to study the temperature dependence. Figure 4.7(a) illustrates the thermally activated erasure of the domain grating at 35 °C. The temporal response of the decay follows a $t^{-\beta}$ law (as is common in spin glasses), were β is a measure of the polarization viscosity [5]. The decay of the polarization grating was monitored continuously for 10^4 to as long as $7x10^5$ seconds. The lifetime is defined as the time in which the polarization modulation amplitude decays to 10% of its value at t = 1 second, to avoid the unphysical singularity of the power law at t = 0. The lifetime of the grating at 20 °C extends well beyond measurable times, yet the onset of freezing was readily apparent from the absence of grating decay after only 4000 seconds. By fitting a $t^{-\beta}$ curve to the decay, the lifetime is estimated to be 10^{15} seconds. The uncertainty of this value, while very large, does not influence the fit parameters significantly because of the divergence of the lifetime near the freezing temperature renders it relatively insensitive to uncertainties in lifetime.

The hologram lifetime data is summarized in figure 4.7(b). Data indicated by triangles correspond to measured lifetimes, the circle to an extrapolated lifetime. Each data point corresponds to two independent yet identical experiments. The functional fit (i) is the

Arrhenius relation for the characteristic time τ for thermal excitation out of a potential well of depth E_a for a system at temperature T:

$$\frac{1}{\tau} = \frac{1}{\tau_o} \exp\left(\frac{-E_a}{k_B T}\right). \qquad 4.4$$

For a system that exhibits a polarization freezing temperature T_f (typical of glassy ferroelectrics), the Vogel-Fulcher law [6-8] is a more accurate empirical relationship between the decay time (i. e. the lifetime of the remnant domain hologram) and the temperature:

$$\frac{1}{\tau} = \frac{1}{\tau_o} \exp\left(\frac{-E_a}{k_B(T-T_f)}\right) , \qquad 4.5$$

where T is greater than or equal to T_f, the dipolar freezing temperature. The freezing behavior is readily apparent for temperatures below 30 °C in figure 4.7(b), where the inverse lifetimes asymptotically approach zero. Fit (ii) illustrates the Vogel-Fulcher fit, with T_f = 19 °C, E_a = 5 meV and τ_o = 1 sec, and displays excellent agreement with the data. This indicates that polarization gratings can be permanently frozen-in at sufficiently low temperatures.

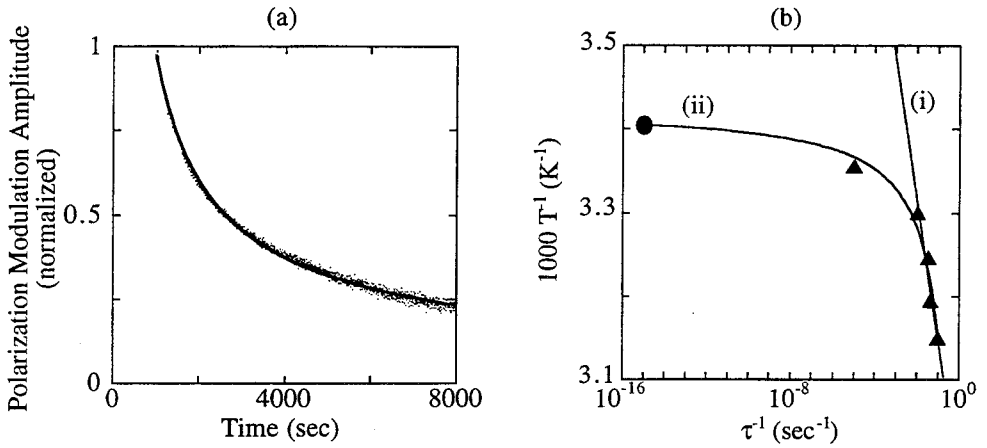

Figure 4.7: (a) Power law decay of remnant polarization modulation amplitude at 35 °C. (b) Lifetime of remnant polarization modulation amplitude for different temperatures. Curve fit (i) describes an Arrhenius and (ii) a Vogel-Fulcher thermal activation process.

The magnitude of the remnant polarization modulation shows a temperature resonance for recording stages conducted between 30 to 37 °C (figure 4.8). The weak response at low temperatures is due to the large viscosity of the glassy polarization. On the other hand, at temperatures above 35 °C, the decrease of the electrooptic coefficient and the thermal scrambling of the domain grating conspire to reduce the diffraction efficiency. A two-stage fixing process, in which the domain grating formation is thermally assisted at elevated temperatures (30 to 35 °C) and then frozen-in at slightly lower temperatures (25 to 20 °C), enhances both the grating modulation and lifetime.

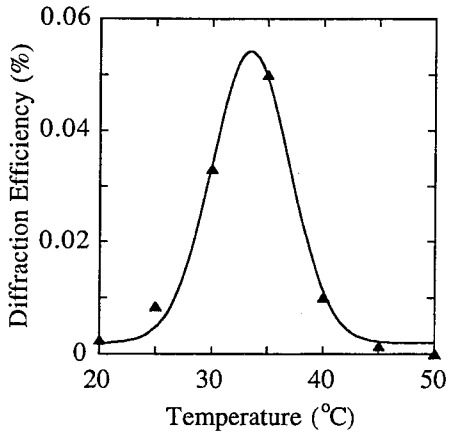

Figure 4.8: Resonance in the diffraction efficiency of remnant polarization grating for holograms recorded between 30 and 37 °C.

The mechanism of optically induced domain reversal by space charge fields is an example of the macro-to-microdomain transformation observed under external electric fields [4]. External depoling fields in the presence of illumination have reportedly produced a microdomain state in SBN [9]. In the experiments described in this chapter, the periodic space charge is the source of the depoling field. By cooling the crystal from above the Curie temperature to the freezing temperature T_f, in the absence of an applied field, the ferroelectric is in a zero-field-cooled state in which long range ferroelectric order is absent. However, by cooling under an applied poling field, long range order can be frozen-in below T_f. This is conventionally called the field-cooled state. Depoling electric fields E, applied parallel to the c axis, lower the local freezing temperature through the deAlmedia-Thouless relationship [6, 10]:

$$T_f(E) = T_f(0)\left[1 - \left(\frac{E}{A}\right)^{2/3}\right], \qquad 4.6$$

where A is a constant defined as $A = k_B T/p_s$ and p_s is the freezing dipole moment. The photogenerated space charge field is the source of this applied field. The periodic field spatially modulates the freezing temperature. In those regions where the freezing temperature is perturbed downward, the relaxation rate of the glassy polarization to the unpoled state increases dramatically. Therefore, in regions where the space charge field is parallel to the c axis, the long range order (or frozen-in polarization) will "thaw out" and reduce the polarization locally.

A microphotograph of the domain grating recorded using high intensity fixing is illustrated in figure 4.9. This photograph is obtained by illuminating the crystal with an extraordinarily polarized plane wave at 488 nm. The index perturbation causes the incident beam to waveguide along the grating planes. This produces the intensity contrast evident in figure 4.9. This technique has been analyzed in detail by Rupp [11]. The crystal is initially uniformly poled and in the field-cooled state (figure 4.9, left). A permanent domain grating with a period of 10 microns is subsequently recorded (center) and then electrically erased (right) with 3000 V cm^{-1} for 10 seconds under weak illumination. The intensity maxima correspond to grating planes of larger index relative to the minima. The SBN crystal is negative uniaxial, so the dark fringes correspond to regions of depolarization.

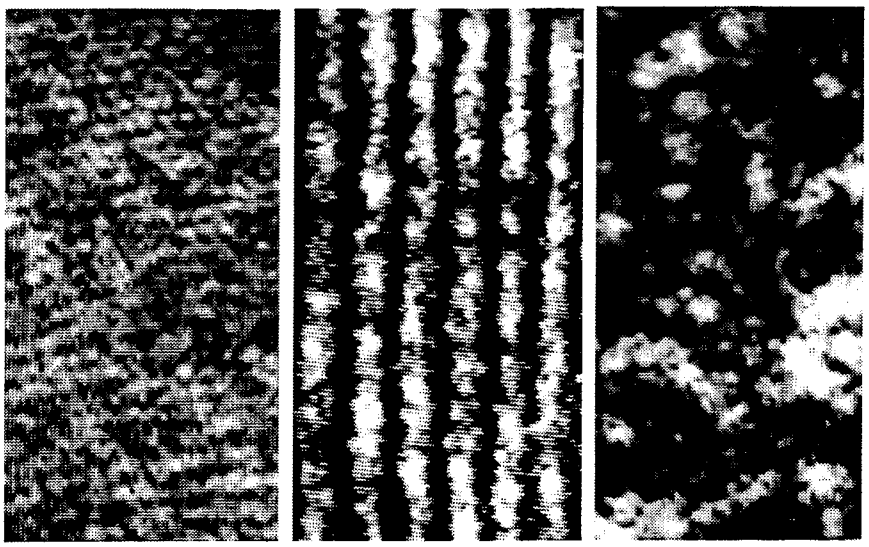

Figure 4.9: Microphotometrically revealed domain grating with period of 10 microns in SBN:75. left: poled crystal; center: domain grating; right: electrically erased grating.

4.4 Summary

Optically induced domain reversal enables light to modulate the symmetry of a bulk crystal over distances on the order of optical wavelengths. The role of the space charge field in the local domain reversal is isolated by performing low intensity experiments in the absence of optical heating or external fields. A qualitative thermodynamic description of the fixing process based on spin glasses elucidates the kinetics of domain reversal. These kinetics are studied in greater detail by measuring Barkhausen current noise, as discussed in the next chapter.

References for chapter four

[1] A. S. Kewitsch, M. Segev, A. Yariv, R. R. Neurgaonkar, *Opt. Lett.* **18**, 1262-1264 (1993).

[2] A. S. Kewitsch, A. Yariv, M. Segev, in *The Photorefractive Effect* D. Nolte, Ed. (Kluwer Academic, New York, 1995).

[3] A. S. Kewitsch, M. Segev, A. Yariv, G. J. Salamo, T. W. Towe, E. J. Sharp, R. R. Neurgaonkar, *Phys. Rev. Lett.* **73**, 1174-1177 (1994).

[4] J. B. Thaxter, M. Kestigian, *Appl. Opt.* **13**, 913-924 (1974).

[5] K. Binder, A. P. Young, *Rev. Mod. Phys.* **58**, 801 (1986).

[6] D. D. Viehland, Dissertation, The Pennsylvania State University (1991).

[7] H. Vogel, *Phys. Z.* **22**, 645 (1921).

[8] G. J. Fulcher, *J. Am. Cer. Soc.* **8**, 339 (1925).

[9] M. Horowitz, A. Bekker, B. Fischer, *Appl. Phys. Lett.* **62**, 2619-2621 (1993).

[10] J. R. de Almedia, D. J. Thouless, *J. Phys. A.* **11**, 983 (1978).

[11] R. A. Rupp, *Appl. Phys. B* **41**, 153 (1986).

Chapter Five

Barkhausen Noise

5.1 Introduction

The dynamics of domain grating formation are readily studied by measuring the displacement current or Barkhausen noise across the crystal as domains invert [1]. These measurements isolate the role of photorefractive space charge fields from thermal effects in the generation of ferroelectric domain gratings. They also demonstrate that the domain grating has a large dynamic component displaying a time response similar to the photorefractive space charge field.

The Barkhausen effect was first observed in the early work on ferromagnetic domain reversal [2]. Subsequently, electrical Barkhausen noise was linked to ferroelectric domain switching in barium titanate [3, 4]. As a domain inverts, the changing electric dipole induces charge on the surface electrodes. This time varying charge produces a current transient which is conventionally called a Barkhausen jump.

Barkhausen currents have been measured in numerous photorefractive ferroelectrics under external fields. These jumps have been observed in $LiNbO_3$ under intense illumination and at elevated temperatures, and were used as evidence for a domain switching contribution to hologram fixing in this material [5]. Current transients in $BaTiO_3$ during electrical fixing

[6, 7] have also been observed. However, these experiments did not isolate the noise caused by both external fields and heating from that noise originating from photoinduced space charge fields. That is the purpose of this chapter.

5.2 Theory

The early measurements and analyses of Barkhausen noise are generally restricted to crystals in the form of thin c plates (~100 μm thickness). Domains typically nucleate below an electrode evaporated on the crystal surface and subsequently grow to the other electrode [8]. The crystal is also assumed to be non-conducting, appropriate for crystals such as $BaTiO_3$ in the dark. However, to investigate photoinduced domains, measurements are performed under illumination and in the presence of mobile charge. It is necessary to relate the volume of the inverted domains deep within the illuminated region of the crystal to the measured Barkhausen current noise. This relationship is established by drawing on the electrostatic theory of a polarized dielectric. The central theoretical problem is to relate the measured short circuit current across the crystal to the free and bound charges moving within the crystal. To simplify this analysis, the electrodes across the ferroelectric crystal are treated as infinite conducting sheets short-circuited by an ideal current meter $i(t)$ (figure 5.1). Only the center of the crystal is illuminated, so charge carriers do not flow directly from the illuminated region to the electrodes. Thus, the induced current is the displacement current $\varepsilon\, \partial E/\partial t$ alone. A quasi-electrostatic approach is adopted since the frequencies of interest are below 100 KHz. Thus, currents induced by the magnetic fields associated with moving charges are ignored.

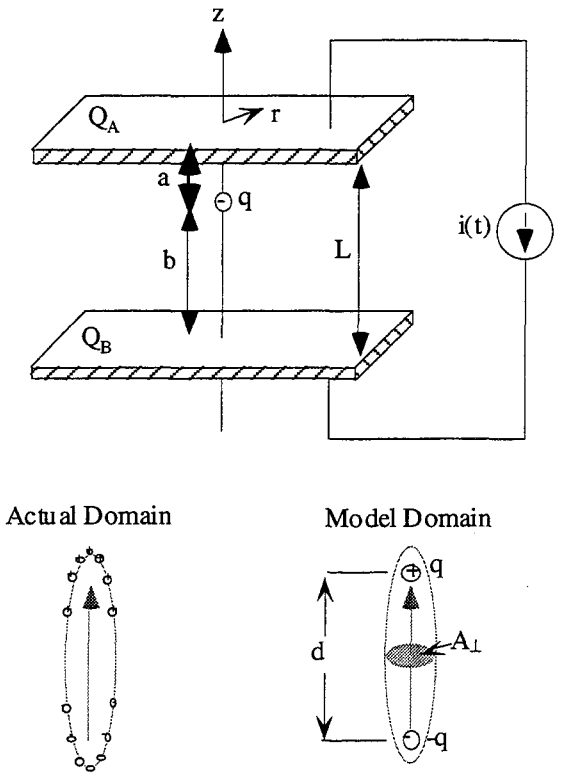

Figure 5.1: Barkhausen noise current theoretical model.

Both free and bound charge will contribute to the displacement current measured across the crystal. For example, the free electronic charge is photoexcited and spatially redistributed under illumination. By using the method of images from electrostatics (figure 5.2) [9], an analytical expression is derived for the charge Q_A and Q_B induced on the conducting plates by the electric field of a point charge q_f embedded in a medium with a low frequency dielectric constant ε:

$$Q_A = - q_f \frac{b}{L}, \; Q_B = - q_f \frac{a}{L} \; . \qquad 5.1$$

a is the distance from electrode A to the point charge and b is the distance from electrode B to the point charge, and a+b = L, the distance between the electrodes. From the above

analysis, it is apparent that the displacement current generated within the crystal under illumination is composed of a free charge component, even in the absence of domain reversal:

$$i(t) = \frac{\partial}{\partial t}(Q_B - Q_A) = - q_f \frac{2}{L}\frac{\partial a}{\partial t} \quad . \qquad 5.2$$

$\partial a/\partial t$ gives the component of the free charge velocity parallel to the surface normal of the electrodes. In general, this free charge contribution to the displacement current arises from the transport of free charge due to drift, diffusion, and the photovoltaic effect. Note that the current given by equation 5.2 is independent of the low frequency dielectric constant ε.

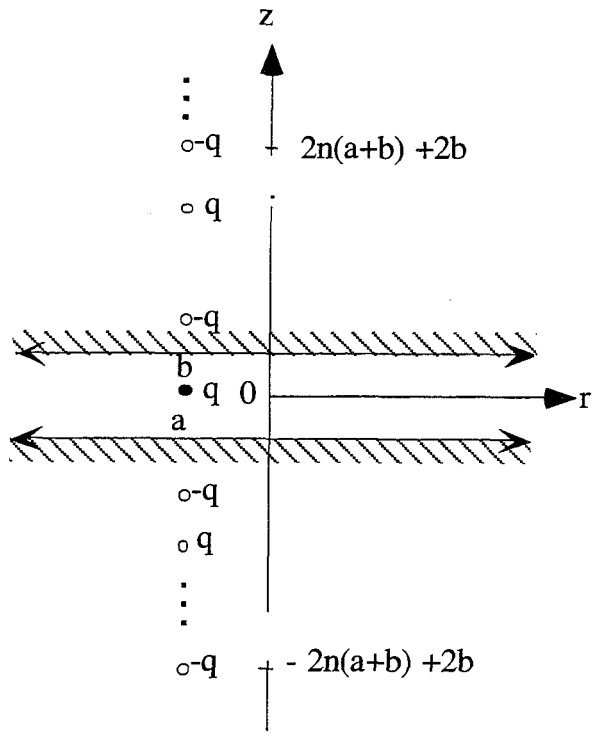

Figure 5.2: Model of displacement current by method of images.

A second source of current noise in addition to the motion of photoexcited electronic charge is domain switching. The inversion of ferroelectric domains creates characteristically sharp current transients due to the collective displacement of ferroelectric ions. This distinguishes domain switching from slowly varying space charge effects. As an inverted domain nucleates and subsequently grows, bound charge is created, generating current noise. To relate the measured current across the crystal to the volume of the inverted domain(s) associated with each current spike, the charge Q_A and Q_B induced on the conducting plates as a function of the location and size of the inverted, ellipsoidal domain is computed. The domain is treated theoretically as charges q and -q separated by a distance d, as in figure 5.1. Note that d is slightly smaller than the physical domain length. The charge is distributed along the entire domain wall for which $\mathbf{P}_s$ is not parallel to the interface. To simplify the analysis, the charge is treated as if it were all localized near the foci of the ellipsoidal domain. The induced charge at the electrodes is then:

$$Q_A = -q\frac{d}{L},\quad Q_B = q\frac{d}{L}, \tag{5.3}$$

where d is the distance between the opposite centers of total charge q and -q along the **c** axis. The induced charge as given by equation 5.3 is independent of the location of the domain within the crystal and independent of ε. In practice, the charge induced by domains near the edges of the finite electrodes does depend on position. This effect is neglected because the crystal is illuminated only at the center in our experiments. The current across the crystal is computed by differentiating the induced charge on the electrodes with respect to time:

$$i(t) = \frac{d}{dt}(Q_B - Q_A) = \frac{2}{L}\left(d\frac{\partial q}{\partial t} + q\frac{\partial d}{\partial t}\right). \tag{5.4}$$

q is composed of both the bound charge q_b and free charge q_f. The free charge is generated upon optical illumination and compensates the bound charge at the domain walls:

$$q_b = \Delta P\, A_\perp = 2\, P_d\, A_\perp\,, \qquad 5.5$$

where $A_\perp$ is the cross sectional area indicated in figure 5.1. P_d is the average polarization of the individual domain, typically larger than the macroscopic spontaneous polarization. By substituting equation 5.5 into equation 5.4, the transient displacement current due to domain switching is:

$$i(t) = \frac{4}{L} P_d\, A_\perp\, d\left(\frac{\partial \ln A_\perp}{\partial t} + \frac{\partial \ln d}{\partial t} + \frac{\partial \ln P_d}{\partial t}\right) + \frac{2}{L}\left(d\frac{\partial q_f}{\partial t} + q_f \frac{\partial d}{\partial t}\right)\,. \qquad 5.6$$

The first term of equation 5.6 represents the sideways growth of domains (perpendicular to **c** axis), the second term represents nucleation and forward growth (parallel to **c** axis), and the third term represents the change in the individual dipole moment (arising from heating, for example). The last two terms describe the free charge compensation of bound charge. They are present in photoconductors because illumination and thermal excitation provide mobile compensating charge.

The subtle temporal sequence of events in the formation of the space charge field, lattice distortion, domain switching and free charge compensation can be revealed by examining the transients in displacement current. Upon writing a domain grating with photorefractive space charge fields, the domains may invert when the field is larger than the local coercive field. However, upon inversion, significant depolarization fields equal to $2\, P_d/\varepsilon$ are generated at the head-to-head domain walls. For the resulting domain configuration to be stable, the depolarization fields must also be screened. In fact, the screening of depolarization fields requires significantly more charge (on the order of $P_d/\varepsilon E_c \sim 10$ times

more, where $P_d \sim P_s$ is the spontaneous polarization and E_c the coercive field) than the initial charge required to establish the coercive field. The primary source of this compensating charge is expected to be the photorefractive space charge. However, additional charge may be provided by thermally or optically excited carriers unrelated to the original spatially periodic photorefractive space charge field, or at pre-existing domain walls. The important role of this later contribution is supported by the observation of increased domain switching in optically fatigued crystals

The depth of spatial modulation of the spontaneous polarization is highly dependent on the optical exposure. This effect results from accelerated free charge compensation and screening of the ferroelectric dipole interaction [10] in the presence of illumination. The response time of compensation is the dielectric relaxation time τ_{diel} for diffusion dominated charge transport (i. e., for grating periods > Debye screening length, which is on the order of μm). Under illumination with light of intensity I,

$$\tau_{diel} = \frac{\varepsilon}{\sigma_d + I\,\sigma_{ph}}, \qquad 5.7$$

where σ_d is the dark conductivity and σ_{ph} is the photoconductivity. For optical intensities of 1 W cm^{-2} at 45 °C, τ_{diel} is 8 seconds for Cr doped SBN:75, while in the dark, τ_{diel} is effectively infinite because of the extremely low dark conductivity. These decay times are measured by monitoring the decay of uniform pyroelectric fields due to conduction through the crystal (figure 5.3). The pyroelectric fields are measured with a Trek Inc. non-contact electrostatic voltmeter with an input impedance of 10^{14} ohms. Thus, at high optical intensities, the conductivity is sufficient to screen out some fraction of Barkhausen noise events.

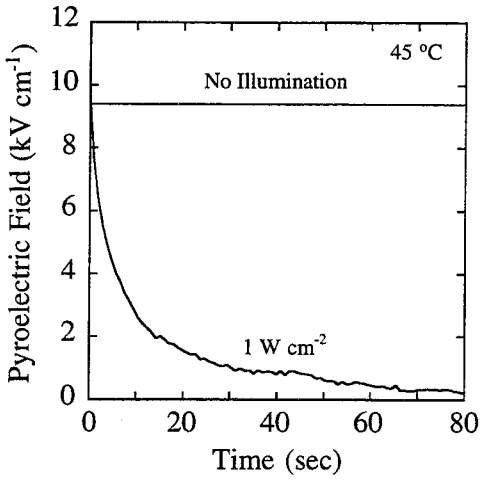

Figure 5.3: Decay of pyroelectric fields in the dark and under illumination. The dielectric relaxation time of Cr doped SBN:75 at 45 °C is 8 sec at I_o = 1 W cm^{-2}.

The volume of the inverted region is estimated by integrating the total charge Q_{tot} under a current spike. The current event is assumed to correspond to the switching of a single ellipsoidal domain of volume V:

$$V = \frac{Q_{tot}\, L}{6\, P_d}. \qquad 5.8$$

Equation 5.8 also assumes that the compensating free charge exhibits a buildup time (proportional to the dielectric relaxation time of equation 5.7) which is much slower than the domain switching transient. This is a good assumption for intensities below 100 W cm^{-2}, a regime where Barkhausen noise frequency components greater than the inverse dielectric relaxation time are unscreened by photoexcited charge. For 10 W cm^{-2}, this lower cutoff frequency is estimated to be 1.25 Hz from equation 5.7.

5.3 Domain Nucleation Energy Requirements:

The energy decrease upon reorientation of spontaneous polarization $\mathbf{P}_s$ in an electric field $\mathbf{E}$ is given by:

$$\Delta W_v = -2\, \mathbf{P}_s \cdot \mathbf{E}\, \Delta V, \qquad 5.9$$

where ΔV is the volume of the inverted domain. The increase in surface energy (including ferroelastic coupling and depolarization fields) is:

$$\Delta W_s = \sigma\, \Delta A, \qquad 5.10$$

where ΔA is the change in surface area of the domain wall with surface energy density σ. To simplify the analysis, the domain is treated as a cylinder of radius r and height h. Then the total change in crystal energy upon domain nucleation is:

$$\Delta W = 2\pi\, r\, h\, \sigma - 2\, P_s E\, \pi\, r^2\, h\ . \qquad 5.11$$

The equilibrium domain radius r_o, assuming a typical domain aspect ratio h/r = 10, is:

$$r_o = \frac{2\,\sigma}{3\,P_s E}\ . \qquad 5.12$$

This relates the size of the inverted domain to the surface energy, spontaneous polarization and external field.

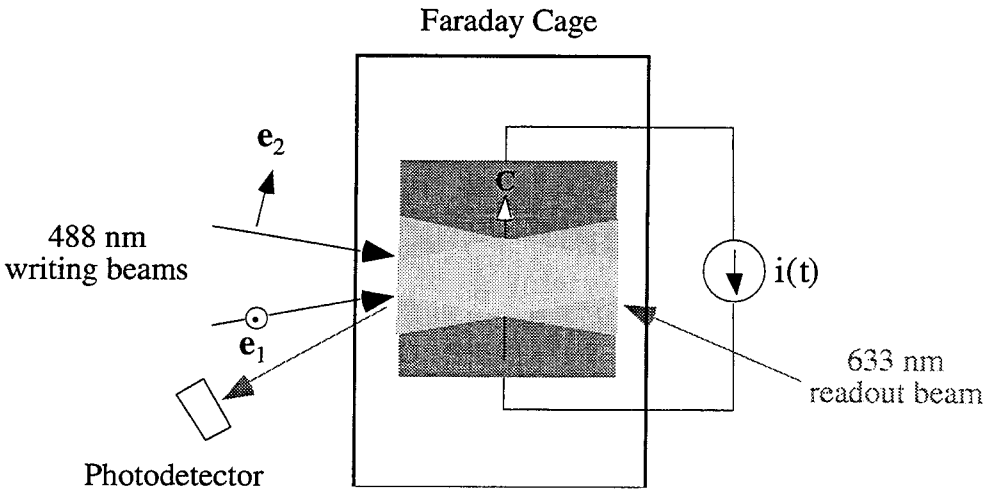

Figure 5.4: Experimental setup to measure Barkhausen current noise.

5.4 Experimental Results

The experimental setup to measure the diffraction efficiency and current noise is schematically represented in figure 5.4. The experiments are performed on room temperature poled, Cr-doped SBN:75 and SBN:61 single crystals. The **c** faces of the crystal are electroded with silver paint and thermally annealed. To maintain reproducibility, the saturated spontaneous polarization is periodically restored by thermallizing the domain structure (heat treating at 350 to 450 ^{o}C in air) and subsequently electrically poling with 10 KV cm^{-1} at room temperature. The current noise is measured by the input preamplifier of a Stanford Research Systems SR830 Lock-in amplifier (1 KΩ input impedance) or by an oscilloscope (1 MΩ input impedance, 500 MHz bandwidth). A Tektronix 2440 digital storage oscilloscope is used for high temporal resolution studies, and a computer data-acquisition system is used for low temporal resolution studies.

The volume holograms are recorded with two collimated TEM_{00} single frequency (488 nm) beams (diameter 1.5 mm). The holographic grating (typical period 1.1 μm) is simultaneously reconstructed with a counter-propagating, 50 mW cm^{-2}, 633 nm HeNe laser to monitor the diffraction efficiency. The relative polarization of the two recording beams is mechanically adjusted by rotating a half wave plate in the optical path of one of the beams. The photorefractive space charge field can then be tailored without changing the total optical intensity. This is essential to isolate the Barkhausen noise generated by space charge fields from that generated by optical heating.

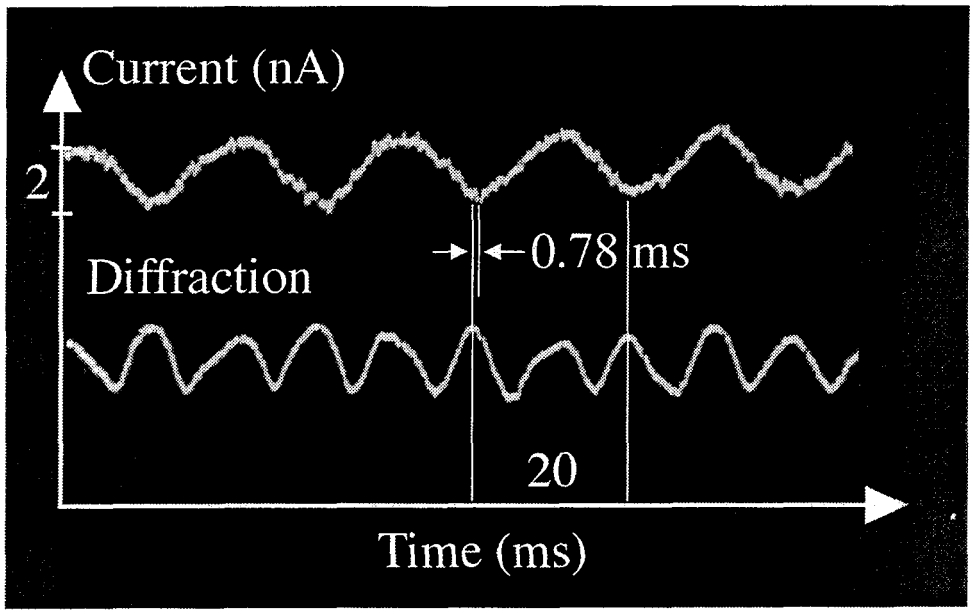

Figure 5.5: Noise in current (50 Hz) induced by oscillating space charge field (modulation in diffraction ~ 0.5%). The current lags diffraction by 0.78 ms (SBN:61, I_o ~ 1 W cm^{-2}, T = 22 °C, thermal steady state).

The first contribution to the displacement current arises from the moving space charge directly. By inducing a periodic phase shift between the two recording beams at 50 Hz, the spatial phase of the interference pattern is modulated by ~ 20°. 50 Hz noise in the current

is observed (figure 5.5). The noise in diffraction efficiency occurs at twice the modulation frequency. This effect is apparent in both SBN:61 and SBN:75. At these low current levels, a fraction of the noise current may also result from microdomain alignment in glassy ferroelectrics such as SBN. Since the microdomains are believed to possess extremely small volumes (~100 nm^3), the current induced by inverting microdomains would also produce an apparently smoothly varying signal.

A non-steady-state current has also been reported in the photoconductors BSO and BGO upon temporal modulation of the space charge field [11, 12]. In these experiments, the displacement current is believed to be negligible compared to the charge transport across the crystal and through the external circuit. The entire crystal is illuminated, so indeed the high photoconductivity of these materials facilitates charge transport from the crystal bulk to the electrodes. In contrast, in the experiments of this chapter the displacement current is measured because only the center of the crystal is illuminated.

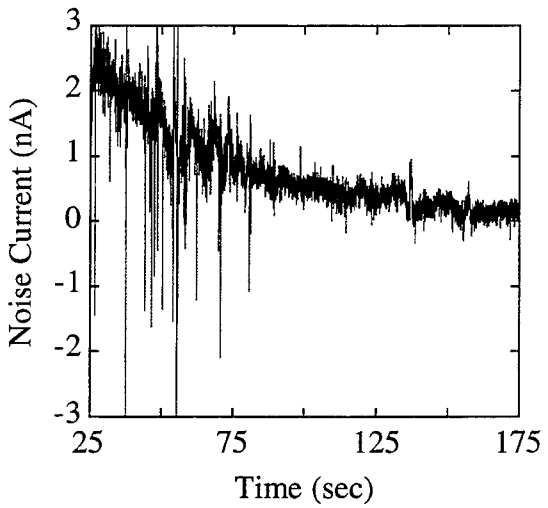

Figure 5.6: Pyroelectric and Barkhausen current due to optical heating (SBN:75, I_o ~ 20 W cm^{-2}, $T_{ambient}$ = 22 °C, prior to thermal steady state).

The second and most interesting contribution to the noise current is unambiguously linked to the moving bound charge created upon domain switching. Figure 5.6 illustrates the noise generated across the crystal during the initial stage of intense optical illumination (~ 20 W cm^{-2}) with two orthogonally polarized recording beams. One beam is extraordinary, the other ordinary, so the electric field vectors of the beams remain orthogonal as they propagate through the uniaxial crystal. At this stage the beams do not produce a spatially modulated electron density. Illumination begins at t = 0, and the peak pyroelectric current reaches a value of 250 μA on the time scale of ms. The current decays exponentially with a time constant of 400 ms. Figure 5.6 illustrates the subsequent decay, the vertical scale magnified to reveal individual Barkhausen jumps.

If the polarizations of the two beams instead have a component parallel to one another, producing a photorefractive grating, the noise current does not change significantly. This indicates that most of the current noise during the *initial* stage of hologram recording with high intensity beams is thermal in origin. Local heating due to non-uniform illumination generates local pyroelectric fields. These fields cause domains to invert and produce Barkhausen current spikes (described by the first two terms of equation 5.6). Heating also reduces the intrinsic polarization of the individual domains (described by the third term of equation 5.6) to produce a smoothly varying pyroelectric current. Current jumps are superimposed on the exponential decay of the pyroelectric current until thermal steady state is reached (figure 5.6).

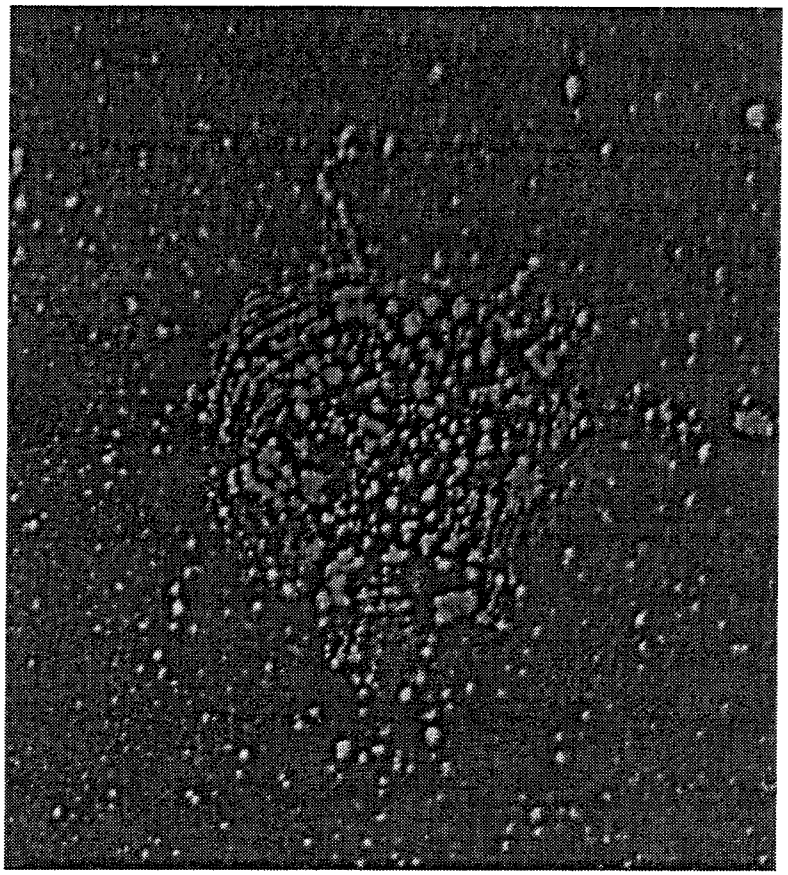

Figure 5.7 Etched **a** face of crystal following high intensity optical exposure

The rapid increase in current during the first seconds of exposure and the subsequent exponential decay is consistent with the expected pyroelectric current generated along the **c** axis by optical heating. The heating partially depolarizes the crystal in the region of intense illumination. This depolarization is revealed by etching the entrance **a** face of the SBN crystal (figure 5.7) for 15 minutes in a concentrated solution (37%) of HCl at room temperature. The origin of domain contrast is believed to be the selective etching of domain walls. Walls possess a high concentration of trapped electronic charge that enhances the rate of etching. This is analogous to the contrast mechanism in $BaTiO_3$, in the sense that +c domains (charge compensated by "free" electrons) etch at a faster rate than -c domains

(electrons depleted) [13]. The sample was subsequently viewed under a transmission optical microscope using polarized, incoherent light. The circular etched region corresponds to the 1.5 mm beam diameter. The spatially periodic domain grating is not apparent, but has been revealed within the bulk by optical means in figure 4.9.

Barkhausen jumps arising from the spatially periodic space charge field *alone* are also observed. The role of the space charge field in domain switching is isolated from thermal effects by maintaining a constant illumination level while tailoring the modulation depth of the interference pattern. First, the crystal is illuminated with two beams of orthogonal optical fields and total intensity of 1 W cm^{-2} for 10 minutes. The noise current up to this point is thermal in origin. After thermal steady state is reached, the electric field vector of one of the writing beams is then rotated by 90°, establishing the interference pattern. A periodic space charge grating builds up at t = 0, as illustrated in the upper trace of figure 5.8. This data reveals the initiation of Barkhausen current events (lower trace) upon hologram exposure. The peak magnitude of the space charge field is ~ 50 V/cm, as estimated from the measured diffraction efficiency at t = 2 seconds (for r_{33} = 1000 pm V^{-1}, appropriate for a partially depoled crystal). These measurements are repeated with the grating vector perpendicular to the c axis, and the Barkhausen noise transients then vanish. In this geometry, the space charge fields are unable to orient domains periodically.

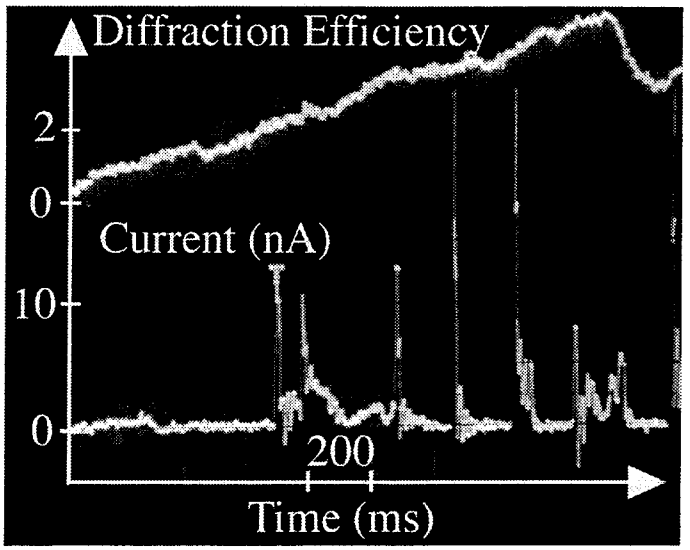

Figure 5.8: Noise in current (bottom) and diffraction efficiency in % (top) as photorefractive space charge grating is recorded (SBN:75, $I_o \sim 1$ W cm^{-2}, T = 30 °C, thermal steady state).

The domain grating rapidly follows the photoinduced space charge field on the time scale of the photorefractive buildup time. This is labeled the *dynamic* domain grating, in contrast to the more typical *remnant* domain grating used to permanently fix domain holograms. The dynamic domain grating relaxes immediately upon the removal of the space charge field. Ferroelectric hysteresis provides memory so that a fraction of the dynamic domain grating survives as a remnant grating. It is important to note that the dynamic domain grating is an inextricable part of the photorefractive effect in SBN. Fundamentally, domain fixing is a manifestation of hysteresis in the electrooptic effect.

5.5 Domain Switching Dynamics

The microscopic mechanisms of domain reversal can be deduced from the form of the current transients. Barkhausen current jumps have been classified into two groups [3] in the early literature: The first type are dome shaped, with a transient characterized by a gentle rise and fall. The second type are spikes, with a very sharp leading edge (duration of 10 μs) followed by an exponential decay to zero. Jumps of the first type appear for all values of the switching field, while jumps of the second type typically appear under strong fields. Both types have smaller average dimensions in aged rather than restored crystals because of domain wall pinning. According to Rudyak [14], the first type of jump is expected during the relatively slow sideways growth of domains. The sharp leading edge of the second type of pulse is associated with a fast nucleation event, and the subsequent exponential decay is associated with the growth of the domain [3]. The velocity of sideways domain wall motion (parallel to an **a** axis) is believed to be slower than the forward velocity of domain walls (parallel to a **c** axis) because of the large depolarization fields established in the former case. The rate of sideways domain growth is expected to increase with optical intensity because of the availability of mobile charge to screen these depolarization fields.

Single domain switching events of both the first and second type are observed under illumination. The first type, characterized by a gradual rise and fall of 5 ms duration, are associated with the slow sideways growth of a domain (figure 5.9(a)). The second type have durations of typically 1 ms and rise times on the order of 10 μs (figure 5.9(b)). The sharp rise is attributed to domain nucleation and the subsequent decay to domain growth. This rise time is in agreement with measurements of single domain events in $BaTiO_3$ [3]. Temporal and spatial correlation of domain switching events is also present in SBN. The

majority of optically induced current transients in an unfatigued SBN sample display multiple sharp peaks occurring over a period of 100 ms (figure 5.9(c)).

(a)

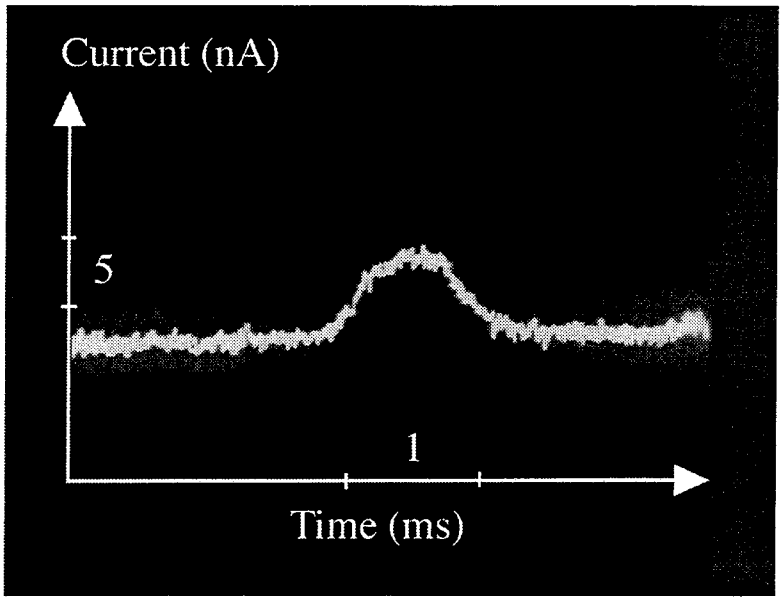

(b)

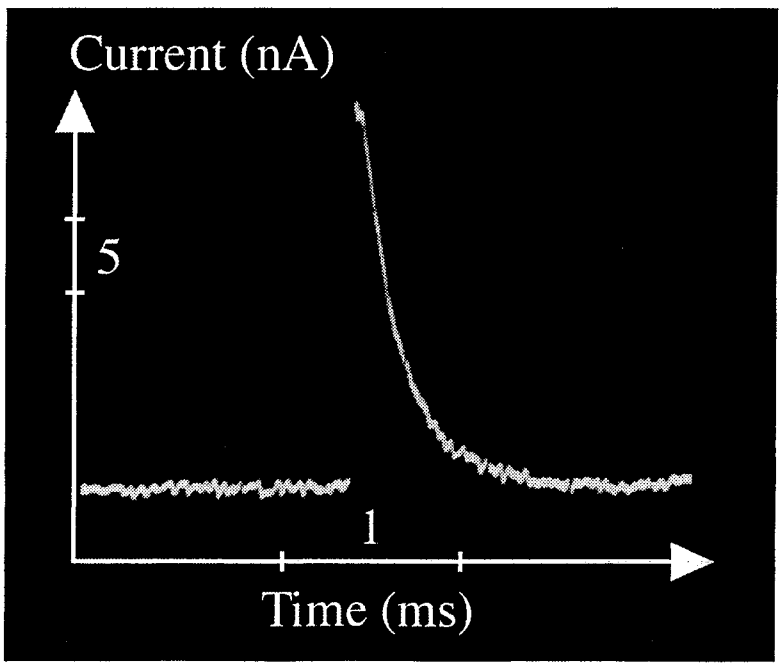

(c)

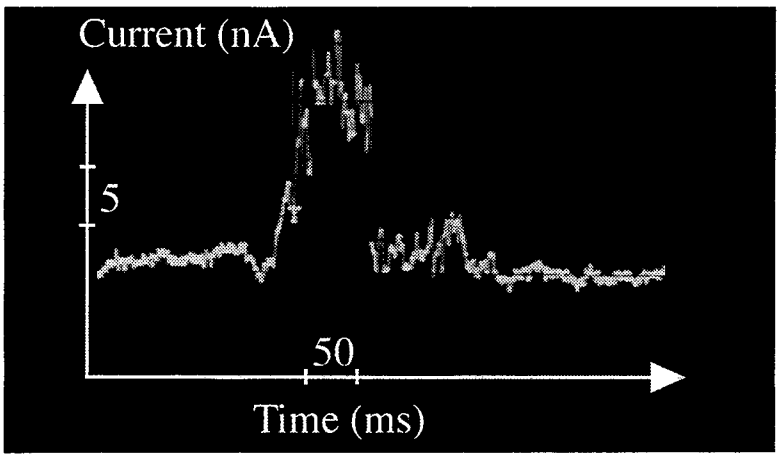

Figure 5.9:

Barkhausen current events: single domain events of (a) type I and (b) type II, and (c) multiple domain switching event (SBN:75, $I_o \sim 8$ W cm^{-2}, $T_{ambient} = 22$ °C, prior to thermal steady state).

From equation 5.8 the volume of an individual inverted domain associated with a typical current spike in SBN:75 (1 ms duration, 10 nA height and $P_d \sim P_s \sim 20$ μC cm^{-2}) is 7×10^4 μm^3. This volume increases dramatically (by about two orders of magnitude) when multiple domain switching events occur simultaneously. At ambient temperatures, current spikes with peak heights as large as 100 nA have been observed in SBN:75, while in the SBN:61 sample the spikes are typically 5 to 10 times smaller in amplitude.

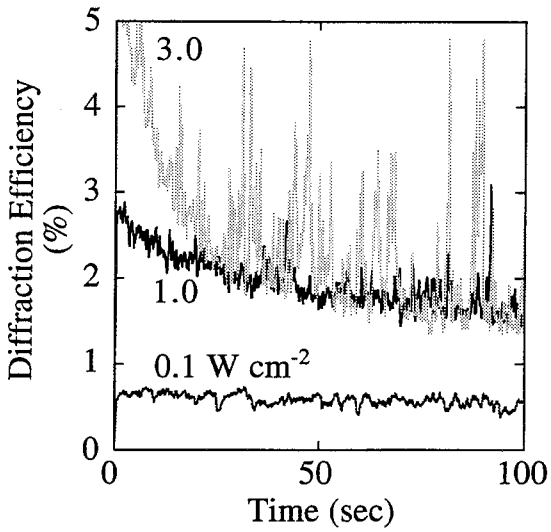

Figure 5.10: Intensity dependence of diffraction efficiency noise (SBN:75, $T_{ambient}$ = 22 °C, prior to thermal steady state).

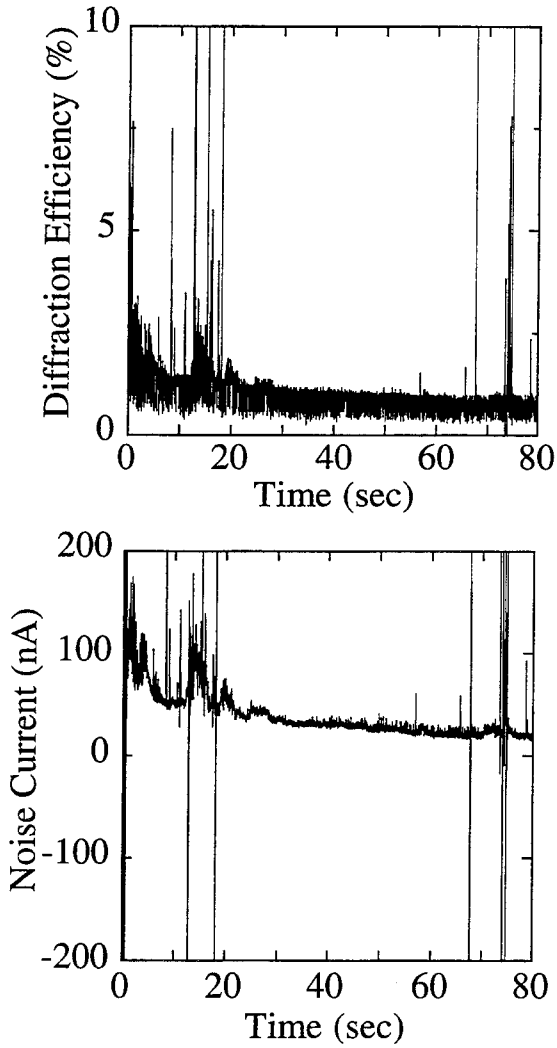

Figure 5.11: Long-time temporal correlation of current and diffraction efficiency noise (SBN:75, $I_o \sim 20$ W cm^{-2}, $T_{ambient} = 22$ °C, prior to thermal steady state).

5.6 Optical Barkhausen Noise

In addition to the strong current noise upon high intensity recording, a previously unreported intensity dependent noise in diffraction efficiency is also apparent (figure 5.10). Above intensities of 1 W cm^{-2}, the noise in diffraction efficiency increases dramatically. To deduce the origin of this effect, the current and diffraction efficiency are measured simultaneously (figure 5.11). The degree of correlation between these two signals is computed numerically. The correlation coefficient function between the diffraction d(t) and the Barkhausen current i(t) is defined as [15]:

$$\rho_{id}(\tau) = \frac{R_{id}(\tau) - \mu_i\mu_d}{\sqrt{\left[R_{ii}(0) - \mu_i^2\right]\left[R_{dd}(0) - \mu_d^2\right]}}, \qquad 5.13$$

where μ_i and μ_d denote the mean values of current and diffraction, respectively, and the cross-correlation function $R_{id}(\tau)$ is defined as

$$R_{id}(\tau) = \lim_{T\to\infty} \frac{1}{T}\int_0^T i(t)\, d(t-\tau)\, dt. \qquad 5.14$$

The autocovariance functions for current $R_{ii}(\tau)$ and diffraction $R_{dd}(\tau)$ are defined as:

$$R_{ii}(\tau) = \lim_{T\to\infty} \frac{1}{T}\int_0^T i(t)\, i(t-\tau)\, dt \qquad 5.15$$

and

$$R_{dd}(\tau) = \lim_{T\to\infty} \frac{1}{T}\int_0^T d(t)\, d(t-\tau)\, dt. \qquad 5.16$$

These correlation integrals may be evaluated in the frequency domain if the data is stationary and ergodic. The noise current is low pass filtered prior to digital sampling to prevent aliasing. This retains frequency components lower than approximately 50 Hz, which comprise the dominant contribution to the signal in an electrically restored crystal. The sample time window is 16 seconds, beginning at t = 64 seconds in figure 5.11. This data consists of 2048 points sampled every 8 ms. The calculated correlation coefficient function is illustrated in figure 5.12. The large correlation peak at $\tau = 0$ indicates that the noise in current and diffraction is correlated for simultaneous events. The series of smaller peaks between $\tau = 0$ and 3 seconds indicates a weaker correlation between an initial diffraction peak and later current transients.

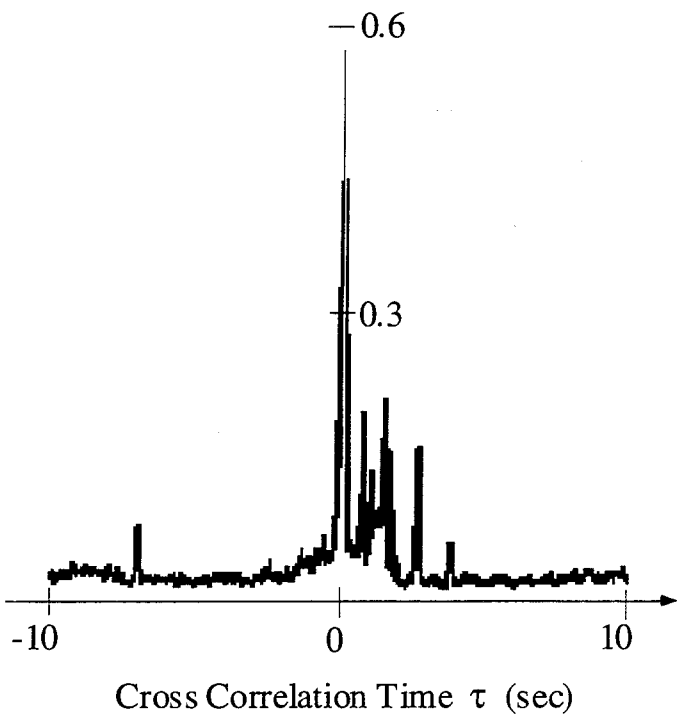

Figure 5.12: Correlation coefficient function of current and diffraction efficiency (for data from t = 64 to 80 seconds in figure 5.11).

The origin of the noise correlation is two-fold. The first source of noise correlation arises from domain switching induced by a changing space charge field, as already discussed in reference to figure 5.8. In this case, a change in diffraction efficiency *triggers* a domain switching event. For instance, for the first correlated noise event in figure 5.13, the space charge field perturbation induces domain switching approximately 200 ms later. This class of events display smooth jumps in diffraction efficiency, followed at some later time by sharp jumps in current. The temporal relationship is apparent in figure 5.12 by the delayed sequence of correlation peaks between $\tau = 0$ and 3 seconds. This figure indicates that if it were possible to apply a delta function in diffraction efficiency to the crystal, a series of noise spikes in current would be observed, whose probability of occurrence decays within a characteristic time of about 3 seconds. That is, figure 5.12 is the impulse response of the ferroelectric distortion under periodic space charge fields. A primary source of this noise is the instability in the spatial phase and amplitude of the optical interference pattern during optical heating. These noise events vanish once thermal steady-state is reached. However, if the optical interference pattern is subsequently perturbed, a sequence of current spikes will be generated as the new domain grating is recorded.

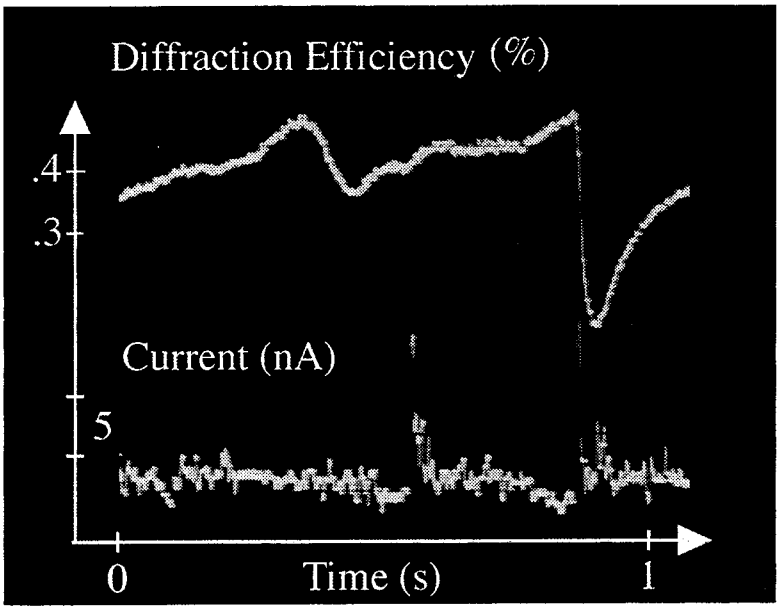

Figure 5.13: Two characteristic noise events in current and diffraction efficiency. The first event is characteristic of a fluctuation in the space charge field initiating domain reversal. The second event is characteristic of noise in diffraction efficiency induced by domain switching (SBN:75, $I_o \sim 8$ W cm^{-2}, $T_{ambient} = 22$ °C, prior to thermal steady state).

Secondly, a large fraction of correlated noise events in current and diffraction occur simultaneously. In this case, the Barkhausen current jump is initiated before the space charge field has changed, so the noise in diffraction efficiency is *triggered* by domain switching (e. g., the second event of figure 5.13). Accordingly, this class of events is not initiated by noise in the optical interference pattern. They are represented by a strong correlation peak ($\rho_{id} = 0.55$ at $\tau = 0$ in figure 5.12) and characterized by abrupt transients in both diffraction efficiency and current. This noise also vanishes after thermal steady state is reached, indicating that the domain switching responsible for noise in diffraction efficiency is initiated by random depolarization due to optical heating, rather than periodic space charge fields. This is expected, since the domain switching arising from optical heating is much more significant than that induced by the space charge fields. The relative contributions are apparent by noting the much stronger Barkhausen noise in figure 5.11

compared to figure 5.8. Note that this interpretation regarding noise triggering is not proven by the limited sample of noise events presented here. However, a large number of individual noise correlation events in the spirit of figure 5.13 have been observed, providing unequivocal evidence.

This second source of noise correlation is primarily the result of the displacement current noise perturbing the free charge transport during dynamic hologram formation. This is analogous to the noise in dynamic beam coupling induced by a fluctuating external applied field. Indeed, the photorefractive band transport model predicts that moderate electrical noise fields across the grating volume will introduce noise in the dynamic beam coupling. Once thermal steady state is reached, this noise current driven by non-uniform optical heating vanishes. In addition, the domain volume passes through the paraelectric phase for a short period of time upon switching between the two ferroelectric orientations, which results in a large transient index change (estimated to be ~ 0.02 at 25 °C from Ref. [16]). The entire domain volume becomes an efficient scatterer of light for a fraction of the switching time. In a separate experiment, the beam fanning during these high intensity exposures is monitored. An identical correlation in the total intensity of the fanning beam and the noise current is observed.

5.7 Summary

Barkhausen current noise associated with ferroelectric domain reversal is induced by photorefractive space charge fields. A strong correlation between the current and diffraction efficiency noise under high intensity optical exposures is present. Furthermore, the rapid buildup of current noise upon hologram recording indicates that a dynamic domain grating is formed. This characterization technique isolates the primary factors responsible for optically induced domain reversal; namely, high intensities and space

charge fields.

References for chapter five

[1] A. S. Kewitsch, A. Saito, A. Yariv, M. Segev, R. R. Neurgaonkar, *JOSA B* , in press (1995).

[2] H. Barkhausen, *Physikalische Zeitschrift* **20**, 401 (1919).

[3] A. G. Chynoweth, *Phys. Rev.* **110**, 1316-1332 (1958).

[4] V. M. Rudyak, *Soviet Physics Uspekhi* **13**, 461-479 (1971).

[5] V. I. Kovalevich, L. A. Shuvalov, T. R. Volk, *Phys. Stat. Sol. (a)* **45**, 249-252 (1978).

[6] R. S. Cudney, J. Fousek, M. Zgonik, P. Günter, M. H. Garrett, D. Rytz, *Appl. Phys. Lett.* **63**, 3399-3401 (1993).

[7] R. S. Cudney, J. Fousek, M. Zgonik, P. Günter, M. H. Garrett, D. Rytz, *Phys. Rev. Lett.* **72**, 3883-3886 (1994).

[8] R. C. Miller, *Phys. Rev.* **111**, 736-739 (1958).

[9] J. D. Jackson, *Classical Electrodynamics*. (Wiley, New York, 1975).

[10] V. M. Fridkin, *Photoferroelectrics*. M. Cardona, P. Fulde, H.-J. Queisser, Eds., Springer Series in Solid State Sciences (Springer-Verlag, Berlin, 1979), vol. 9.

[11] M. P. Petrov, I. A. Sokolov, S. I. Stepanov, G. S. Trofimov, *J. Appl. Phys.* **68**, 2216-2225 (1990).

[12] I. A. Sokolov, S. I. Stepanov, *JOSA B* **10**, 1483-1488 (1993).

[13] J. A. Hooton, W. J. Merz, *Phys. Rev.* **98**, 409-413 (1955).

[14] V. M. Rudyak, A. Y. Kudzin, T. V. Panchenko, *Sov. Phys.- Solid State* **14**, 2112-2113 (1973).

[15] J. S. Bendat, A. G. Piersol, *Engineering Applications of Correlation and Spectral Analysis*. (Wiley-Interscience, New York, 1993).

[16] A. S. Bhalla, R. Guo, L. E. Cross, G. Burns, F. H. Dacol, R. R. Neurgaonkar, *J. Appl. Phys.* **71**, 5591 (1992).

Chapter Six

Application of Domain Microstructure to Holographic Data Storage

6.1 Introduction

Two critical technical issues in a permanent holographic data storage system are high efficiency fixing and a convenient multiplexing scheme. One drawback of the ionic fixing technique in $LiNbO_3$ is a single development stage at elevated temperatures in which all space charge holograms are simultaneously fixed. While this is an acceptable method of production for a pre-mastered holographic ROM, it makes it difficult to incrementally add data to the memory. Each fixing process requires heating of the entire hologram volume. For applications such as a holographic random access memory, the ability to add and update fixed holograms in a rapid manner is highly desirable. Domain gratings have this desirable property of being both permanent and updatable at room temperature [1].

Multiple holograms are accessed within the volume by angle or wavelength multiplexing. Over a limited tuning range, wavelength multiplexing can also be accomplished with a single wavelength source by tuning the Bragg law with an applied electric field [2]. This chapter will describe work on both domain fixing and electric field multiplexing for holographic data storage systems.

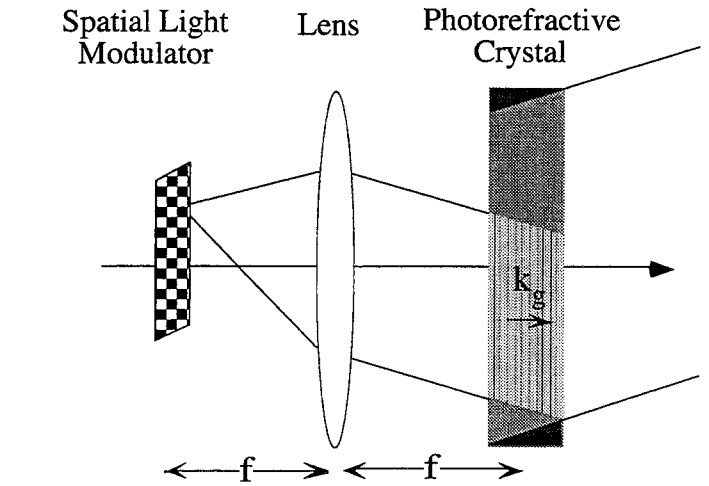

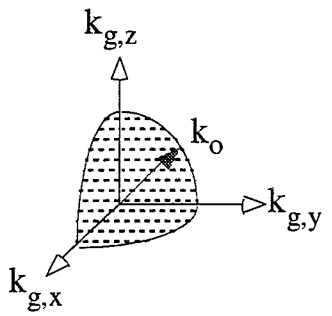

$$N_{modes} = \frac{\frac{\pi k_o^3}{6}}{\frac{\pi}{L_x L_y L_z}}$$

$$N_{bits}^{max} = \frac{64\pi}{3}\frac{V}{\lambda_o^3}$$

Figure 6.1: Theoretical storage capacity of a typical volume holographic memory system.

6.2 Volume Holographic Memory

The motivation for storing data in the form of volume holograms is the potential data storage capacity and rapid, parallel access. The classic expression for the memory capacity of a volume hologram is derived by summing the independent plane wave modes within a cavity the size of the crystal [3, 4]. This predicts a data capacity of 1 TByte cm^{-3} (figure 6.1). This number corresponds to the number of independent sinusoidal gratings that can be stored in the crystal, which is equivalent to the number of bits. The throughput of data in a holographic memory is potentially very high because an entire image may be read out

in parallel. For a binary image with 1000 by 1000 pixels, the number of bits that may accessed in parallel is 1 Mb. The performance goals of a volume holographic random access memory are ambitious: 1 TB capacity, 50 GBps data rate, 10 msec page write, and 100 nsec access time [5].

Angular [4, 6], wavelength [7] and phase-coded [8, 9] multiplexing are the three common techniques for storing multiple holograms in a common volume. These techniques exploit the dependence of the Bragg condition on the angle and wavelength of the writing beams:

$$\mathbf{k}_g = \mathbf{k}_1 - \mathbf{k}_2 \,, \qquad 6.1$$

where $k_g = 2\pi/\Lambda_g$ is the magnitude of the grating vector, $k_1 = k_2 = 2\pi n/\lambda$ are the magnitudes of the reference and signal beam wave vectors, respectively, Λ_g is the grating period, n is the index of refraction and λ is the wavelength in vacuum. Angle multiplexing typically requires mechanical or acoustooptic beam deflectors. Wavelength multiplexing requires a tunable, narrow linewidth laser source. It is desirable to eliminate some of these requirements to reduce the system complexity. One alternative, called electric field multiplexing, offers some potential design flexibility.

6.3 Electric Field Multiplexing

Wavelength multiplexing can be implemented by employing a single wavelength source while tuning the index of refraction in the medium. For instance, an external electric field will change the index through the electrooptic effect. This concept has been demonstrated in SBN:75 [2] and $LiNbO_3$ [10-12]. For ferroelectric crystals, the index change is due to a

combination of the electrooptic, elastooptic, and piezoelectric effects. Table 6.1 lists different first order field-induced effects which play an important role in multiplexing.

Effect:	Response Pairs:
electrooptic	electric field, index
elastooptic	strain, index
piezoelectric	stain, electric field
photoelastic	stress, index

Table 6.1: Optical and electrical effects in pyroelectric crystals [13].

If a dc electric field is applied across the crystal, both the electrooptic and piezoelectric effects contribute to Bragg detuning. In fact, a simple relation can be derived to illustrate the formal equivalence between electric field and wavelength multiplexing. This analysis is restricted to the case of counter-propagating signal and reference beams, both normally incident on the crystal. The Bragg condition becomes $\Lambda_g = \lambda/2n$. The selectivity of the hologram is related to the angular, wavelength, or index detuning required to move off the Bragg diffraction peak. For reflection holograms, the Bragg wavelength and index selectivity are maximal. If the configuration displays inherently high selectivity, then the magnitude of the multiplexing field is reduced. This allows more holograms to be electrically accessed for a given maximum electric field.

The electric field required to detune from Bragg diffraction peak can be determined analytically. Differentiating the Bragg condition at constant temperature T and mechanical

stress σ, a relation for the change $\Delta\lambda$ required to maintain Bragg matching under a field induced change $\Delta n[E]$ and $\Delta\Lambda_g[E]$ is obtained:

$$\frac{\Delta\lambda}{\lambda} = \frac{\Delta n[E,\lambda]}{n} + \frac{\Delta\Lambda_g[E]}{\Lambda_g} . \qquad 6.2$$

This result applies to the counter-propagating, reflection grating configuration. Since the index of refraction in the crystal depends on the electric field and wavelength, the field induced index perturbation is:

$$\Delta n[E,\lambda] = \Delta n[E] + \frac{dn[\lambda]}{d\lambda}\Delta\lambda . \qquad 6.3$$

Substituting equation 6.3 into equation 6.2, the relationship for the change in wavelength equivalent to a field induced change of the index of refraction and grating period is:

$$\frac{\Delta\lambda}{\lambda} = \frac{1}{\left(1 - \lambda/n\, dn/d\lambda\right)}\left(\frac{\Delta n[E]}{n} + \frac{\Delta\Lambda_g[E]}{\Lambda_g}\right). \qquad 6.4$$

In a non-centrosymmetric crystal, the field induces an index change through a combination of the electrooptic, elastooptic and piezoelectric effects [13] and may rotate the principal axes by a field dependent angle. Consider a simple yet common case, in which the optical and dc fields are parallel to the field-induced principal axes. In this configuration the principal axes do not rotate under applied fields. The change in index along a principal axis is [13]:

$$\Delta n_l[E_k] = -\frac{n_o^3}{2}[r_{lk}\, E_k + p_{lm}\, d_{km}\, E_k] \,, \qquad 6.5$$

where r_{lk}, p_{lm}, d_{km} are the electrooptic, elastooptic and piezoelectric tensors, respectively, and l = (ij), m = (np) in contracted notation. The field also induces a strain in the crystal, described by the piezoelectric effect:

$$\frac{\Delta\Lambda_g}{\Lambda_g} = d_{km}\, E_k \,. \qquad 6.6$$

In practice, both the clamped and unclamped electrooptic coefficients are measured. In a clamped crystal, the strain is by definition zero, so the second term on the right of equation 6.5 is zero. The clamped electrooptic coefficient therefore corresponds to r_{lk}. Most often, the unclamped electrooptic coefficient is measured, which is actually equal to $r_{lk} + p_{lm}\, d_{km}$. The unclamped value is typically about twice the clamped value.

The electrooptic, piezoelectric and elastooptic effects combine to produce a total field-induced detuning $\Delta\lambda$:

$$\Delta\lambda = \frac{\lambda}{\left(1 - \lambda/n\ dn/d\lambda\right)}\left(-\frac{n_o^2}{2}[r_{lk}\, E_k + p_{lm}\, d_{km}\, E_k] + d_{km}\, E_k \right). \qquad 6.7$$

Therefore, multiplexing is achieved by varying the indices of refraction and the lattice parameters. The material parameters are dependent not only on E but also on the

temperature T and mechanical stress σ. A relation analogous to equation 6.4 is obtained upon replacing E by T or σ for the cases of "temperature" or "stress" multiplexing. For constant E and σ:

$$\frac{\Delta\lambda}{\lambda} = \frac{1}{\left(1 - \lambda/n\ dn/d\lambda\right)}\left(\frac{\Delta n[T]}{n} + \frac{\Delta\Lambda_g[T]}{\Lambda_g}\right), \qquad 6.8$$

while for constant T and E:

$$\frac{\Delta\lambda}{\lambda} = \frac{1}{\left(1 - \lambda/n\ dn/d\lambda\right)}\left(\frac{\Delta n[\sigma]}{n} + \frac{\Delta\Lambda_g[\sigma]}{\Lambda_g}\right). \qquad 6.9$$

The following discussion will focus field multiplexing under constant temperature and stress.

To simplify the analysis of electric field multiplexing described by equation 6.4, the index dispersion $dn/d\lambda$ is neglected relative to n/λ. This results in an error of approximately 20% [14]. The second term on the right of equation 6.4, the strain term, is on the order of $\Delta n/n$. A scale factor ξ_E is defined as:

$$\frac{\Delta n[E]}{n} + \frac{\Delta\Lambda_g[E]}{\Lambda_g} \equiv \xi_E \frac{\Delta n[E]}{n}, \qquad 6.10$$

where ξ_E is assumed to be a slowly varying function of the field E in the range of $0 \le |\xi_E| \le 10$ [15], depending on the sign and magnitudes of the linear electrooptic and

piezoelectric coefficients. An analogous scale factor is defined for the temperature dependence:

$$\frac{\Delta n[T]}{n} + \frac{\Delta \Lambda_g[T]}{\Lambda_g} \equiv \xi_T \frac{\Delta n[T]}{n}, \qquad 6.11$$

where $\Delta\Lambda_g = \alpha\,\Delta T$ (α is the thermal expansion coefficient). For the stress dependence:

$$\frac{\Delta n[\sigma]}{n} + \frac{\Delta \Lambda_g[\sigma]}{\Lambda_g} \equiv \xi_\sigma \frac{\Delta n[\sigma]}{n}, \qquad 6.12$$

where the first term on the left is a piezo-optical contribution and the second term is the strain. Then the index selectivity or index half-power bandwidth, defined as $|\Delta n|_{FWHM}$, for constant T and σ, is related to the spectral half-power bandwidth of a Bragg peak $|\Delta\lambda|_{FWHM}$ [16] by equations 6.4 and 6.10:

$$\frac{|\Delta n|_{FWHM}}{n} \approx \frac{1}{\xi_E} \frac{|\Delta\lambda|_{FWHM}}{\lambda} \approx \frac{1}{\xi_E} \frac{\Lambda_g}{L}, \qquad 6.13$$

where L is the thickness of the crystal. The above expression relates the Bragg selectivity for field multiplexing to the familiar result for wavelength multiplexing. Since the grating period for two plane waves in this configuration is $\Lambda_g = \lambda/2n$, the minimum index change $\Delta n_{min} = 2\,|\Delta n|_{FWHM}$ between adjacent holograms written at the same wavelength is approximately

$$\Delta n_{min} \approx \frac{\lambda}{\xi_E L} . \qquad 6.14$$

The temperature and stress must be stabilized to within:

$$\Delta T << \frac{\xi_E}{\xi_T} \Delta n_{min} \left(\frac{dn}{dT}\right)^{-1} \qquad 6.15$$

and

$$\Delta \sigma << \frac{\xi_E}{\xi_\sigma} \Delta n_{min} \left(\frac{dn}{d\sigma}\right)^{-1} . \qquad 6.16$$

In practice, the stabilization of stress and temperature can be readily achieved by proper mounting of the medium. When these stability conditions are met, the number of holograms $N_{holograms}$ that can be multiplexed electrically is:

$$N_{holograms} = \frac{\Delta n_{max}}{\Delta n_{min}} \approx \frac{\xi_E L}{\lambda} \frac{dn}{dE} \Delta E_{max} . \qquad 6.17$$

To maximize $N_{holograms}$, two primary requirements must be satisfied. The material must have at least one large electrooptic coefficient that induces a significant index change for an electric field (1) along $\mathbf{k}_g$ to produce index gratings and (2) along $\mathbf{e}_1$, $\mathbf{e}_2$ (the polarization vectors of the reference and signal) for electrically biasing the index of refraction. In addition, there are three conditions of secondary importance: it is desirable that the external

field does not rotate (3) the optical field vectors of the incident beams or (4) the principal axes. Failure to satisfy conditions (3) and (4) will reduce the beam coupling because the polarization of the two beams will no longer remain parallel and in the desired direction of condition (2) as they propagate through the crystal. Finally, (5) the material should have a large piezoelectric tensor component d_{km} of the proper sign such that ξ_E is maximized

The counter-propagating reflection grating geometry is optimal for electric field multiplexing. This configuration has two primary advantages. First, the counter-propagating configuration exhibits inherently high wavelength selectivity [7]. Second, it maintains a strong index dependence in the Bragg law. That is, a given change of index does not induce as large a change in the grating vector for oblique incidence. In fact, for the transmission geometry with equal angles of incidence, the index dependence of the Bragg condition disappears:

$$2\,\Lambda_g\, n_{crystal}\, \sin\theta_{crystal} = 2\,\Lambda_g\, \sin\theta_{air} = \lambda. \qquad 6.18$$

Nevertheless, the Bragg condition retains its field dependence $\Lambda_g[E]$ even in this case through the piezoelectric term.

For typical parameters (λ_o = .5 μm, L = 1 cm, extraordinarily polarized signal and reference) and estimating $\xi_E \approx \xi_T \approx 1.25$, the minimum index separation Δn_{min} between independent holograms is $4\text{x}10^{-5}$. For a material such as SBN:75 with $dn/dT = 2.5\text{x}10^{-4}$ [9], the temperature must be stable to within $\Delta T << 0.16$ °C at 25 °C. Since r_{33} is the only significant electrooptic coefficient in SBN:75, the optimal geometry is a compromise to

simultaneously satisfy both conditions (1) and (2) (figure 6.2). This configuration also satisfies conditions (3) and (4). The total index tuning range in the "optimized" configuration is approximately $\Delta n_{max} = 0.0025$, half of $\Delta n_{max} = 0.005$ [17] for a material such as SBN:75. Then the number of holograms that can be electrically multiplexed about λ_o in SBN:75 is approximately 60. Obviously, this number is difficult to achieve if holograms are stored as domain gratings, since the applied fields will tend to erase the fixed holograms.

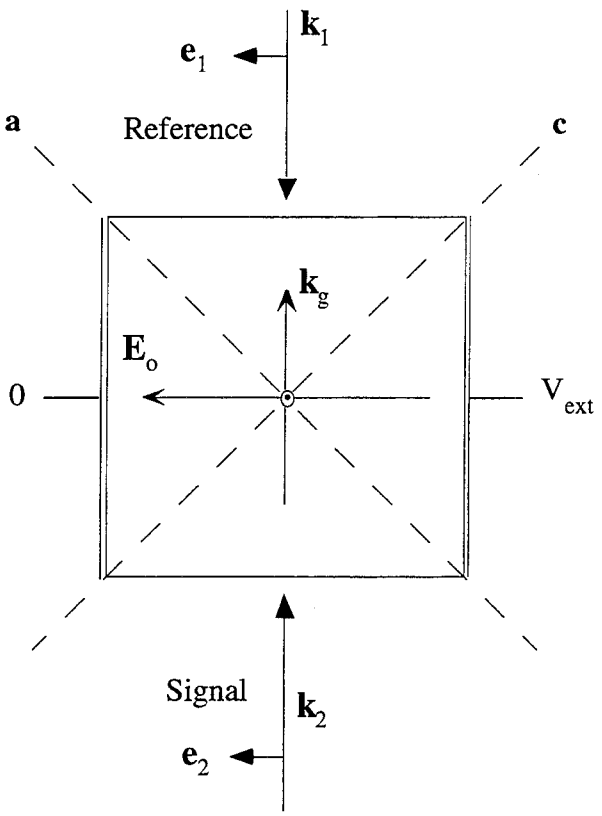

Figure 6.2: Optimum configuration for electric-field multiplexing in SBN:75, with dominant electrooptic coefficient r_{33}.

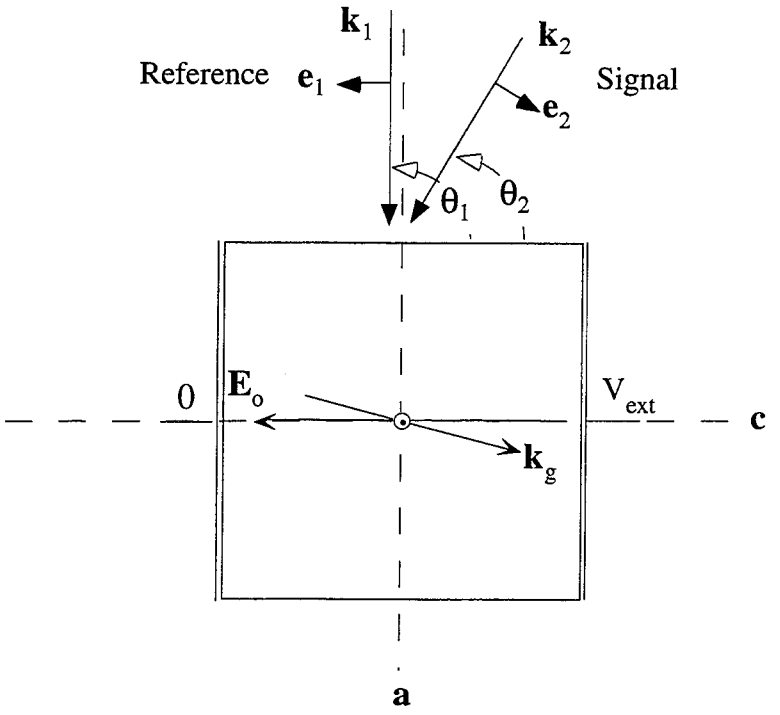

Figure 6.3: Transmission grating configuration for electric field multiplexing.

Non-standard, 45° cut crystals are required to implement electric field multiplexing in the counter-propagating configuration. Instead, a regular cut SBN:75 has been selected to experimentally demonstrate electric field multiplexing in the configuration of figure 6.3. This configuration prevents condition (1) from being satisfied in the counter-propagating geometry, since r_{33} is the only large electrooptic coefficient. As a tradeoff, the transmission grating configuration with $\theta_{1air} = 90^0$, $\theta_{2air} = 60^0$ and the external field applied parallel to the c axis is chosen.

A single hologram at 0 V cm^{-1} has been switched off its Bragg peak with a field increment as low as 500 V cm^{-1} and recovered when returning to 0 V cm^{-1}. The field increment for the optimum configuration is expected to be 100 V cm^{-1}, from equation 6.7. In addition,

two fixed holograms have been recorded (angular bandwidth of images ≈ 4 mrad), one written with no external field (figure 6.4(a)) and another written with a field of 2000 V cm^{-1} (figure 6.4(b)). Care must be taken to prevent this applied field from being screened by optically excited charges while recording the holograms. The holograms are selectively addressed by re-applying the field at which they were written. As seen in the figures, the two holograms exhibit little crosstalk. Their fixed diffraction efficiency is approximately 1%. The holograms have also been de-multiplexed by varying the angle of the reconstruction beam. These fixed holograms are domain gratings, so after approximately twenty switching cycles, the hologram quality degraded dramatically.

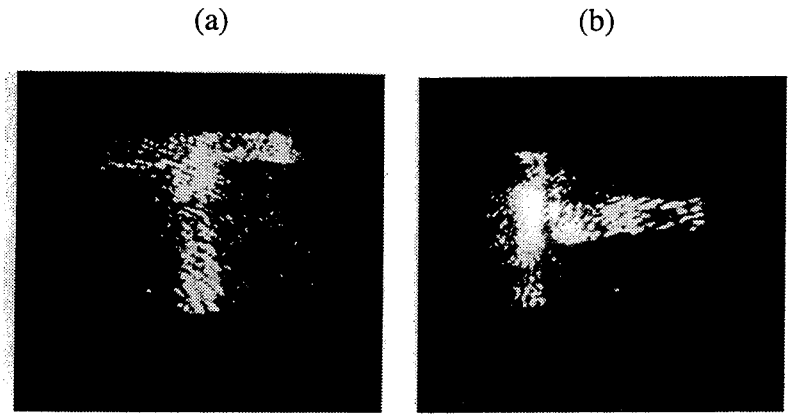

Figure 6.4: Experimental demonstration of electric field multiplexing of two fixed holograms (a) 0 V cm^{-1}, (b) 2000 V cm^{-1}.

6.4 Selective Fixing

An important application of domain fixing is holographic data storage. Domain gratings possess an inherent advantage that they can be individually and selectively fixed [1]. This property is desirable in applications such as holographic random access memories or reconfigurable optical interconnects, yet it is difficult to implement using conventional thermal fixing techniques in $LiNbO_3$. Figure 6.5 shows the selective overwriting of one of three fixed, angle multiplexed holograms. The reference beams of each hologram are separated by $\Delta\theta = 0.01$ rad. The crystal is not thermally stabilized during writing, so the Bragg peaks of the holograms are thermally broadened by a factor of 10. The three holograms, labeled (a)-(c), were individually written and automatically fixed with 4 W cm^{-2} for 30 min each. The index modulation of holograms at other addresses is nevertheless slightly degraded during the fixing process. Proper exposure scheduling during the selective overwriting process will minimize the degradation of adjacent fixed holograms. However, as is apparent in figure 6.5, the dynamic range of the recording media (i.e., the maximum index perturbation) is insufficient to perform several recording cycles. The hologram strength is close to the inherent noise floor arising from index inhomogeneities and scattering from domain interfaces. The dynamic range of the photorefractive crystal can be improved by optimizing the density of photorefractive traps, given by N_d^+ in chapter one.

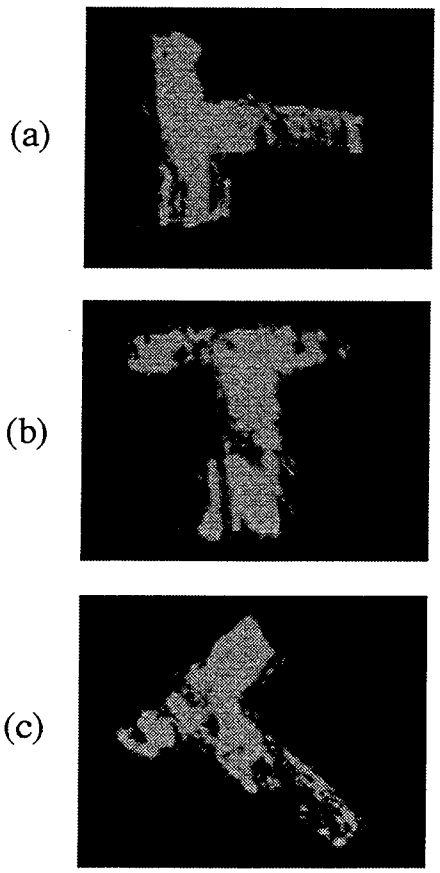

Figure 6.5: Selective, page addressable fixing of three angle multiplexed volume holograms (a)-(c). The poor image quality is the result of scattering from growth striations and domain walls.

6.5 Summary

Volume holograms can be electrically multiplexed. Based on a simple theory, we estimate that approximately 50 image carrying holograms are field addressable about each reference beam wavelength and angle. Alternately, electric fields may be applied to fine-tune the Bragg condition and compensate for wavelength drift of the reference beam, for instance. Individual holograms have been selectively fixed by ferroelectric hysteresis and a primitive

image storage device has been implemented. These techniques have potential benefits in a holographic memory, optical interconnect, or optical correlator. However, major progress must still be achieved to improve the optical quality and dynamic range of these holographic materials.

References for chapter six

[1] A. S. Kewitsch, M. Segev, A. Yariv, R. R. Neurgaonkar, *Opt. Lett.* **18**, 1262-1264 (1993).

[2] A. S. Kewitsch, M. Segev, A. Yariv, R. R. Neurgaonkar, *Opt. Lett.* **18**, 534-536 (1993).

[3] T. Jannson, *Optica Applicata* **IX**, 169-177 (1979).

[4] P. J. van Heerden, *Appl. Opt.* **2**, 393-400 (1963).

[5] R. G. Zech, *Optics & Photonics News*, August, 16-25 (1992).

[6] F. H. Mok, M. C. Tackitt, H. M. Stoll, *Opt. Lett.* **16**, 605-607 (1991).

[7] G. A. Rakuljic, V. Leyva, A. Yariv, *Opt. Lett.* **17**, 1471-1473 (1992).

[8] C. Denz, G. Pauliat, G. Rosen, *Opt. Comm.* **85**, 171-176 (1991).

[9] Y. Taketomi, J. E. Ford, H. Sasaki, J. Ma, Y. Fainman, S. H. Lee, *Opt. Lett.* **16**, 1774-1776 (1991).

[10] S. I. Stepanov, A. A. Kamshilin, M. P. Petrov, *Sov. Tech. Phys. Lett.* **3**, 36-38 (1977).

[11] M. P. Petrov, S. I. Stepanov, A. A. Kamshilin, *Ferroelectrics* **21**, 631-633 (1978).

[12] M. P. Petrov, S. I. Stepanov, A. A. Kamshilin, *Optics Communications* **29**, 44-47 (1979).

[13] J. F. Nye, *Physical Properties of Crystals Their Representations by Tensors and Matrices*. (Oxford University Press, Oxford, 1964).

[14] E. L. Venturini, E. G. Spencer, P. V. Lenzo, A. A. Ballman, *J. Appl. Phys.* **39**, 343-344 (1968).

[15] E. Nakamura, Ed., *Landolt-Börnstein Ferroelectric Oxides, New Series* , vol. III/28a (Springer-Verlag, Berlin, 1990).

[16] H. Kogelnik, *Bell Sys. Tech. J.* **48**, 2909-2947 (1969).

[17] J. B. Thaxter, M. Kestigian, *Appl. Opt.* **13**, 913-924 (1974).

Chapter Seven

Applications to Domain Microstructure to Quasi-Phase Matched Second Harmonic Generation

7.1 Introduction

Optical second harmonic generation is a process in which an optical wave at frequency ω induces a wave at frequency 2ω within a nonlinear optical medium. Classically, the medium is thought of as a collection of dipole radiators driven by the incident optical field. The polarizability of individual bonds typically exhibits a nonlinear dependence on the driving field. This bond charge oscillates not only at ω, but also at the higher harmonics. Under a condition called phase matching, these radiators each emit a field which adds constructively to efficiently produce light at a particular harmonic. This phase matching condition only occurs at particular frequencies and in certain materials. A technique to achieve phase matching at any optical wavelength is desired. This chapter describes a new way to phase match in the visible spectrum using dynamic ferroelectric domain gratings.

7.2 Nonlinear Optical Frequency Conversion

The nonlinear optical response of a medium is described by an expansion of the induced optical polarization P in powers of the electric field amplitude E [1]:

$$P_i(t) = \varepsilon_o \chi_{ij} E_j + d_{ijk} E_j E_k + 4\chi_{ijkl} E_j E_k E_l + \ldots \quad . \qquad 7.1$$

The term $d_{ijk}E_jE_k$ describes first order optical nonlinearities, typically the dominant nonlinear term in non-centrosymmetric materials. First order nonlinearities include second harmonic generation, sum/difference frequency generation, optical rectification and the electrooptic effect. Theoretically, these processes are described by the interaction of a monochromatic wave:

$$E_j^{\omega 1}(t) \equiv \mathrm{Re}\left(E_j^{\omega 1} e^{i\omega_1 t}\right) = \frac{1}{2}\left(E_j^{\omega 1} e^{i\omega_1 t} + E_j^{\omega 1 *} e^{-i\omega_1 t}\right), \qquad 7.2$$

with a medium whose response is given by equation 7.1. The electrooptic effect described in chapter two can equivalently be expressed as

$$P_i^{\omega+\Omega} = \sum_{j,k} d_{ijk}^{\omega,\omega,\Omega} E_j^{\omega} E_k^{\Omega} \quad . \qquad 7.3$$

Here Ω is a low frequency electric field, typically in the range of dc to MHz. Alternately, both fields can be optical. This interaction mixes the two waves to produce new waves at the sum and difference frequencies. Sum/difference frequency generation takes the form:

$$P_i^{\omega 3=\omega 1+\omega 2} = \sum_{j,k} d_{ijk}^{\omega 3,\omega 1,\omega 2} E_j^{\omega 1} E_k^{\omega 2} \quad . \qquad 7.4$$

The degenerate case of this process is second harmonic generation:

$$P_i^{2\omega} = \sum_{j,k} d_{ijk}^{2\omega,\omega,\omega} E_j^{\omega} E_k^{\omega} \quad . \qquad 7.5$$

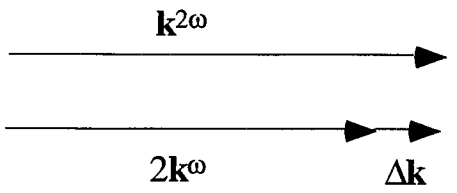

Figure 7.1: Momentum conservation relation for second harmonic process. Δk is the wavevector mismatch.

Second harmonic generation will be the focus of this chapter. The coupled wave equation describing the evolution of the second harmonic optical beam as it passes through the nonlinear medium is given by [1]:

$$\frac{dE^{2\omega}}{dz} = -i\,\omega\sqrt{\frac{\mu}{\varepsilon}}\; d_{eff}^{2\omega,\omega,\omega}\,[E^{\omega}(z)]^{2}\exp\left(i\,\Delta k\,z\right). \qquad 7.6$$

Integrating across the crystal length $z = 0$ to L for an input plane wave E^{ω},

$$P^{2\omega} = 2\,\frac{(P^{\omega})^2}{A}\left(\frac{\mu}{\varepsilon_0}\right)^{3/2}\frac{\omega^2\,\left(d_{eff}^{2\omega,\omega,\omega}\right)^2 L^2}{n^3}\,\mathrm{sinc}^2\left(\Delta k\,L/2\right). \qquad 7.7$$

To obtain significant second harmonic power it is necessary that the wavevector mismatch $\Delta k << \frac{2}{L}$, for L on the order of mm. This requires that $2\,\mathbf{k}^{\omega} = \mathbf{k}^{2\omega}$, or equivalently $n^{\omega} = n^{2\omega}$. This phase matching condition is equivalent to a momentum conservation relation for the nonlinear interaction. Figure 7.1 depicts the momentum conservation relation graphically.

When the wavevector mismatch is zero, the second harmonic power grows quadratically with distance as it propagates through the medium, according to equation 7.7.

$$P^{2\omega} \sim d^2 L^2 . \qquad 7.8$$

In general, the mismatch is nonzero because of normal dispersion at optical wavelengths. In this case, the mismatch can be compensated for by providing an additional momentum $\Delta k_g = \Delta k$. This is achieved by periodically poling the crystal. Fundamentally, a soft phonon mode ($\omega = 0$, $k = \Delta k_g$) associated with the spontaneous polarization of the crystal provides the additional momentum.

For a square wave modulation of the spontaneous polarization, the second harmonic power still grows quadratically as in equation 7.8; however, the nonlinear optical coefficient is replaced by an effective coefficient, d_{eff}. For the case of perfect square wave modulation of the spontaneous polarization,

$$d_{eff} = d \frac{2}{m \pi} . \qquad 7.9$$

For the case of sinusoidal modulation of the spontaneous polarization, the nonlinear coefficient is reduced by an additional factor of $\pi/4$:

$$d_{eff} = \frac{d}{2} \frac{1}{m} . \qquad 7.10$$

Since the photorefractive space charge fields are approximately sinusoidal, the modulation of the spontaneous polarization averaged over a fraction of the grating period is also expected to be sinusoidal.

7.3 Quasi-Phase Matching Using Dynamic Domain Gratings

Quasi-phase matching (QPM) [2, 3] is a technique to periodically compensate for the phase mismatch between the fundamental and second harmonic beams. This technique relaxes the stringent phase matching requirements based on birefringence [4] or modal dispersion in waveguides [5]. As in the previous section, QPM can be achieved by periodically poling a ferroelectric crystal so that the relevant nonlinear coefficients for SHG are spatially modulated with a period equal to twice the coherence length. For co-linear beams, the coherence length is $l_c = \lambda/4\ (n^{2\omega}-n^{\omega})$, where λ is the wavelength in vacuum of the fundamental beam, n^{ω} is the index of refraction at the fundamental wavelength and $n^{2\omega}$ is the index at the second harmonic. In the absence of periodic domain inversion, the coherence length is the maximum effective crystal length that contributes to the second harmonic power. Coherence lengths exceeding a few mm are needed in practice for efficient conversion. In ferroelectric crystals such as $LiNbO_3$ and $Sr_{.75}Ba_{.25}Nb_2O_6$ (SBN:75), the coherence length is on the order of a few microns for second harmonic generation in the visible; consequently, the non-phase matched conversion is negligibly small despite the relatively large nonlinear coefficients. For these and many other highly nonlinear yet dispersive materials , QPM is a means of increasing the effective interaction length to promote efficient frequency conversion.

QPM by periodic poling has been demonstrated during growth [6], by indiffusion [7, 8], by applying external electric fields [9, 10], electron beams [11], or SiO_2 masks [12]. Typically, only a very narrow frequency band is converted efficiently and it is difficult or impossible to tune the center frequency dynamically, except over a small range using temperature or angle tuning. Fabrication constraints often restrict the region of polarization modulation to a thin layer on the surface or to thin waveguides rather than throughout the

entire volume of the crystal. These periodic domain gratings are typically static and permanent.

7.4 Experimental Observation of QPM in SBN:75

We use dynamic domain gratings to demonstrate tunable QPM-SHG in SBN [13, 14]. This technique uses photoinduced space charge fields alone to modulate the ferroelectric polarization of the crystalline unit cell [15-17], rather than photoinduced screening of external electric fields [10]. Figure 7.2 illustrates the experimental setup for writing dynamic domain gratings and simultaneously generating the second harmonic. A tunable, mode-locked Ti-sapphire laser with 2 ps transform-limited pulses and 250 W peak power is frequency doubled within the Cr doped, 45 ^{o} cut SBN:75 crystal. The fundamental beam is loosely focused with a 20 cm lens to a 100 micron beam diameter at the center of the SBN crystal, producing a peak fundamental intensity of 0.8 MW cm^{-2}. The second harmonic is isolated from the fundamental with an infrared blocking filter, then collected and focused onto a photomultiplier tube (PMT). The far field intensity profile of the second harmonic is viewed simultaneously with a 240 by 240 element CCD array. The signal from the PMT is synchronously detected using a lock-in amplifier with a nominal 400 Hz reference signal generated by the chopper controller.

The average power of the Ti-sapphire laser is monitored with a photodetector and used to correct the second harmonic data for variations in the pump power during the wavelength scan (by dividing the second harmonic signal by the square of the pump power). The pulse duration (2 ps) is relatively constant over the entire wavelength range (880-990 nm). A 1.3 Watt argon-ion laser at 514.5 nm writes a domain grating throughout the crystal volume, and a third, non-Bragg matched beam erases the gratings. Both the argon-ion and Ti-sapphire lasers are extraordinarily polarized.

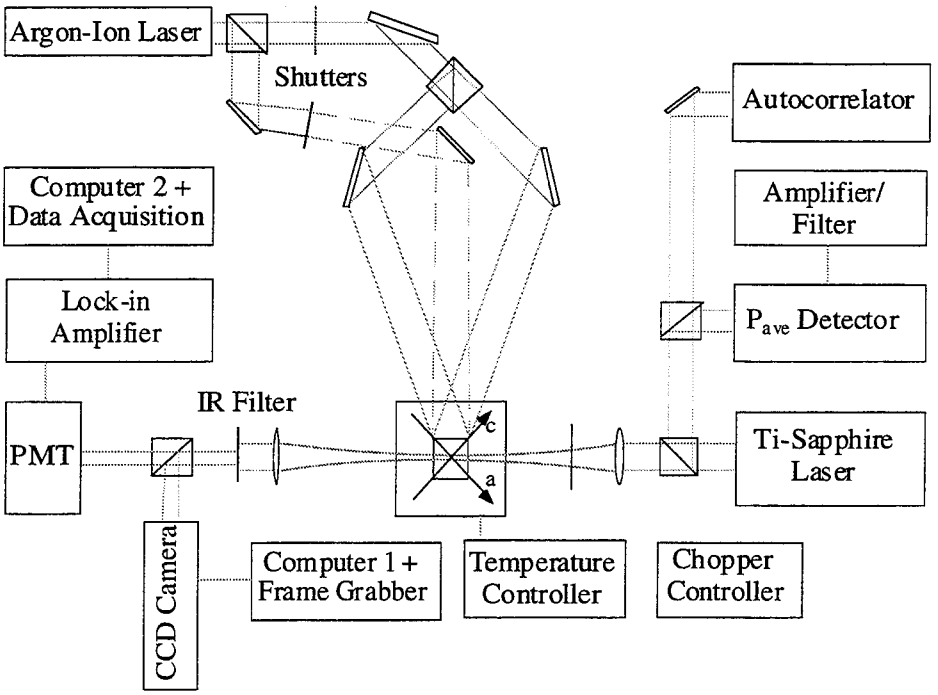

Figure 7.2: Experimental setup for quasi-phase matched second harmonic generation using dynamic domain gratings.

The orientation of the crystalline axes of the SBN:75 crystal shown in figure 7.2 must be selected so that both the grating vector and polarization of the fundamental beam have a significant projection along the c axis. Since the space charge field is used to invert domains, a component of the grating vector along the poling axis is required. Similarly, the fundamental beam must have a significant projection of its optical electric field along the c axis to induce a large polarization at the second harmonic frequency. The magnitude of the polarization at the second harmonic perpendicular to $\mathbf{k}^{\omega}$, the fundamental wave vector, is:

$$P^{2\omega} = 2\left(2\, d_{15}\sin^2\theta\cos\theta + d_{33}\cos^3\theta + d_{31}\sin^2\theta\cos\theta\right)E^{\omega}E^{\omega}, \qquad 7.11$$

where θ is the angle of both $\mathbf{P}^{2\omega}$ and $\mathbf{E}^{\omega}$ relative to the c axis. This function is plotted in figure 7.3. Although $\mathbf{P}^{2\omega}$ attains a maximum value at θ = 0 degrees, this orientation prevents the space charge field from having a significant component parallel to the c axis. However, $\mathbf{P}^{2\omega}$ remains significant for θ as large as 45 degrees. θ = 45 degrees is selected as a convenient tradeoff. By symmetry arguments, inverting the orientation of a ferroelectric domain changes the sign of all three nonlinear coefficients (see chapter two). Thus the effective nonlinear coefficient $d_{eff} = (2\, d_{15} + d_{33} + d_{31})/2^{3/2}$ is modulated in sign by the polarization grating. The grating vector $k_g = \pi/\Lambda$ is oriented parallel to $\mathbf{k}^{\omega}$ and $\mathbf{k}^{2\omega}$ to maximize the spatial overlap of the fundamental and second harmonic field profiles.

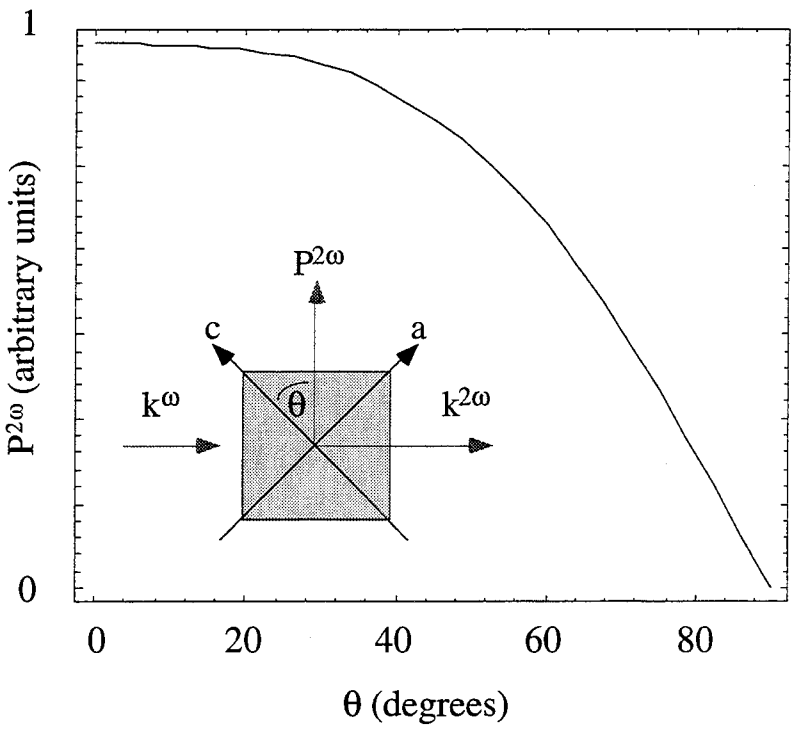

Figure 7.3: Dependence of quasi-phase matched second harmonic power on the crystal configuration of SBN:75.

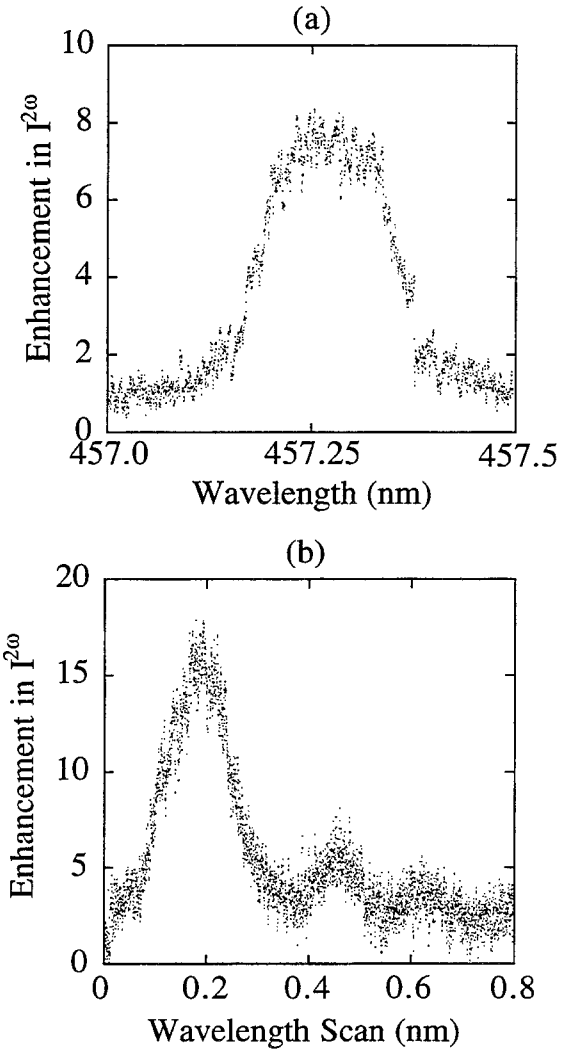

Figure 7.4: (a) QPM tuning curve centered on 457.25 nm with a full width half maxima of 0.175 nm (b) Multiple quasi-phase matching peaks generated by writing several gratings sequentially at the same location within the crystal.

The QPM second harmonic enhancement peak can be shifted across the available tuning range, from 440 to 495 nm, by writing gratings with periods ranging from 3.7 to 3.0 microns. Figure 7.4(a) illustrates a typical QPM peak centered on 457.25 nm. The full

width half maximum (FWHM) of the QPM peak is calculated using reference [18] in addition to the measured index dispersion data [19]. A FWHM of 0.2 nm is predicted for a crystal of thickness 4.25 mm, in close agreement with the measured FWHM of 0.175 nm from figure 7.4(a). This observation confirms that the grating is uniform over the entire 4.25 mm propagation distance. The slight discrepancy is accounted for by differences in the index dispersion of different crystal samples.

An ensemble of gratings with different periods can be written in the same or different locations of the crystal to tailor the spectral response of the SHG and can be rendered permanent by cooling and/or increasing the writing beam intensity. Figure 7.4b illustrates a series of QPM peaks written sequentially in the same volume, with the strongest enhancement peak corresponding to the last grating written. The spectral response can be tailored by writing several gratings (either simultaneously or consecutively) with different periods. This figure also demonstrates that an enhancement of a factor of 17 above the background can be achieved by writing dynamic domain gratings. Typical single pass conversion efficiencies obtained experimentally are of the order of 0.01%. The SHG enhancement will increase further with higher intensity writing beams or with a lower intensity fundamental beam. While the latter option will decrease the conversion efficiency, both options will increase the fringe visibility of the optical interference pattern and enhance the polarization modulation of the grating. The uniform fundamental beam is incoherent with the two writing beams so it reduces the modulation index of the intensity grating. The degree of reduction depends on the absorption of the crystal at the fundamental wavelength. As a direct consequence the photoinduced space charge field and the polarization modulation are reduced by a factor of the modulation index.

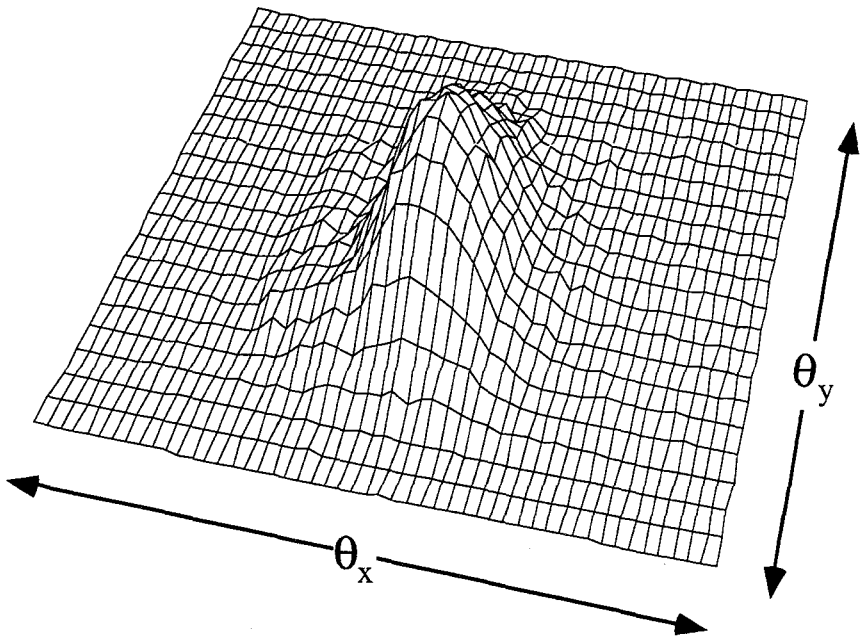

Figure 7.5: Quasi-phase matched, second harmonic far field intensity profile (TEM_{00} mode, angular beam divergence $\theta_{x,y}$ on the order of 1 mrad).

The second harmonic beam exits the crystal in a well collimated, symmetric TEM_{00} mode (figure 7.5) collinear with the fundamental. No change in second harmonic power was measured while scanning the fundamental beam across the face of the crystal and maintaining the relative orientation, confirming that the polarization modulation extends well into the bulk of the crystal.

The rapid enhancement of second harmonic power during the hologram recording stage further supports the existence of dynamic polarization gratings discussed earlier in the context of the Barkhausen noise measurements. Figure 7.6 illustrates the time evolution of this enhancement while writing a QPM polarization grating with a total intensity of 1 W cm^{-2} and a spatial period of 3.5 microns. The transients in the peak enhancement result from the decay and build-up of the grating as the optical interference pattern shifts due to vibration, air currents and temperature changes. The build-up time constant of the QPM peak is approximately inversely proportional to intensity and is consistent with the

photorefractive grating build-up time for SBN:75. At 1 W cm^{-2} the second harmonic build-up time is 0.5 seconds, and at 0.33 W cm^{-2} it is 1.5 seconds.

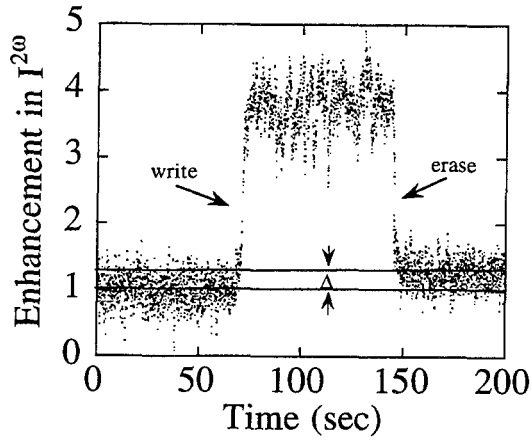

Figure 7.6: Time response of the buildup and decay of second harmonic enhancement while centered on a QPM peak at 457 nm.

At second harmonic wavelengths removed several nanometers from the center of the QPM spectral peak, the second harmonic power is diminished by typically a factor of two rather than enhanced. The time evolution of the second harmonic power is then opposite to that of figure 7.6. This is consistent with the notion that the background pseudo-random domains which contribute to a broadband enhancement of the second harmonic [10] become ordered due to the space charge field, so the second harmonic at wavelengths other than the QPM peak is reduced when the grating is formed.

The decay of the second harmonic enhancement upon uniform illumination indicates that a significant number of domains aligned at $\mathbf{k}_g$ reorient, causing the domain grating to decay. As indicated in figure 7.6, a small remnant enhancement Δ in the second harmonic is permanent, corresponding to the fixed domain grating reported earlier. The lifetime of this permanent grating is highly dependent on temperature but is relatively independent of the

intensity of the erasing beams. Its strength can be increased by applying a fixing technique [17]. At lower temperatures (T < 20 °C) the non-ergodicity characteristic of SBN's glassy polarization state enables the domain orientation to be permanently frozen-in, while at higher temperatures (T > 45 °C) thermal fluctuations of the microdomain orientation randomize the grating [17].

7.5 Experimental Observation of QPM in SBN:61

Domain gratings were recorded in SBN:61 and the temperature dependence of QPM-SHG was analyzed [14]. Space charge field induced QPM-SHG can be achieved even in the paraelectric phase, where the nonlinear optical susceptibility is expected to vanish. In addition, an optically fatigued crystal displays significantly stronger QPM-SHG than an electrically poled crystal. A strong broad-band second harmonic enhancement occurs in optically depoled crystals, as observed earlier [10, 20] with external electric fields applied along the **c** axis. In fact, this broad-band enhancement can attain values several orders of magnitude larger than the QPM enhancement.

The tunable, mode-locked Ti-sapphire laser is frequency doubled within the 45° cut, Ce doped SBN:61 crystal (4.5x4.5x5.5 mm), with a ferroelectric-paraelectric phase transition at 75 °C. The fundamental infrared beam is focused with a 20 cm lens to a 60 micron beam diameter, producing a peak fundamental intensity of 17 MW cm^{-2} at the beam waist. A 2 to 6.6 Watt argon-ion laser at 514.5 nm records a domain grating throughout the entire crystal volume. To maintain the poled state at elevated temperatures, a field of 8000 V cm^{-1} is applied across the electrodes between optical exposures.

The spatial profile of the second harmonic wave is related to the ferroelectric domain structure through a Fourier transform relation [21-23]. The angular spectrum of this wave

indicates the periodicities of the spontaneous polarization or nonlinear optical susceptibility. Upon recording a domain grating in an initially poled crystal, a collimated QPM second harmonic beam is observed (figure 7.7), in addition to a non-phase matched streak. This streak exits the crystal at an angular displacement of approximately 10 degrees below the QPM spot. The origin of this angular walk-off between the two distinct second harmonic beams is the 45 degree inclination of the c axis relative to horizontal. The broad extent of the streak along the x axis and the narrow extent in the y direction indicates that domains are extremely narrow in diameter, while being elongated along the c axis. Typical dimensions of microdomains are tens of nanometers in diameter to 1 μm in length. Figure 7.8 depicts the resulting range of grating vectors generated by the randomly distributed microdomains, represented as a multiplicity of grating vectors with different magnitudes. The momentum conservation relation for the three photon-one phonon interaction is $2\mathbf{k}^{\omega} + \mathbf{k}_g = \mathbf{k}^{2\omega}$, where k^{ω} is the fundamental wavevector and $k^{2\omega}$ is the second harmonic wavevector. The second harmonic far field profile will be directed to a spot (upon interacting with grating periodicity $\mathbf{k}_g^{qpm}$) and a streak (upon interacting with multiplicity of grating periodicities $\mathbf{k}_g^{streak}$). For a random distribution of microdomains of diameter 10 nm, the distribution of $\mathbf{k}_g^{streak}$ is also random up to grating vectors as large as $6\ 10^8\ m^{-1}$.

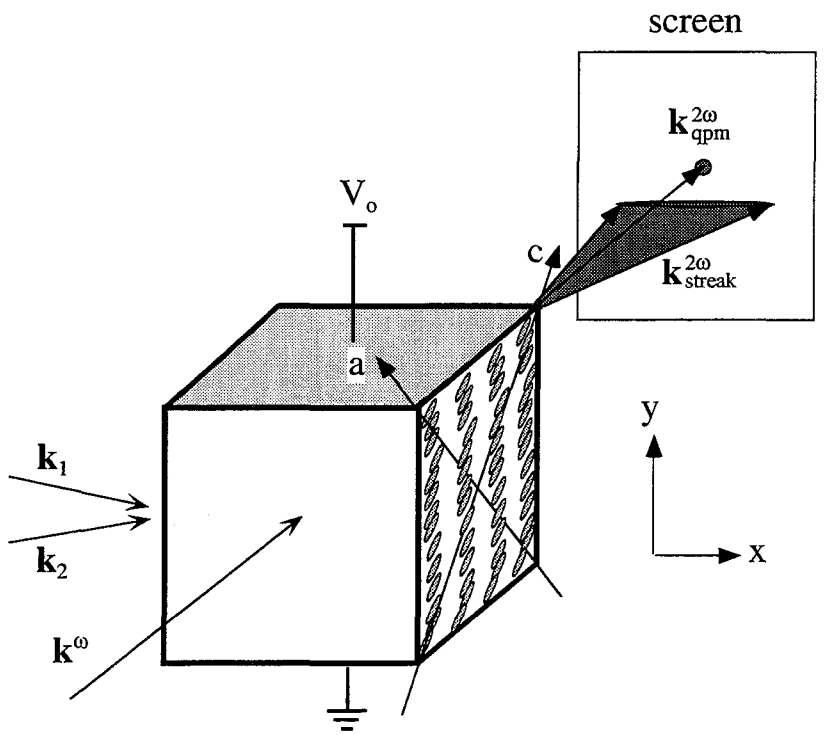

Figure 7.7: Experimental setup: Optical waves $\mathbf{k}_1$ and $\mathbf{k}_2$ record dynamic domain grating, $\mathbf{k}^{\omega}$ is the fundamental beam, and the second harmonic waves exit the crystal to form both a spot $\mathbf{k}^{2\omega}{}_{qpm}$ and a streak $\mathbf{k}^{2\omega}{}_{streak}$ in the far field.

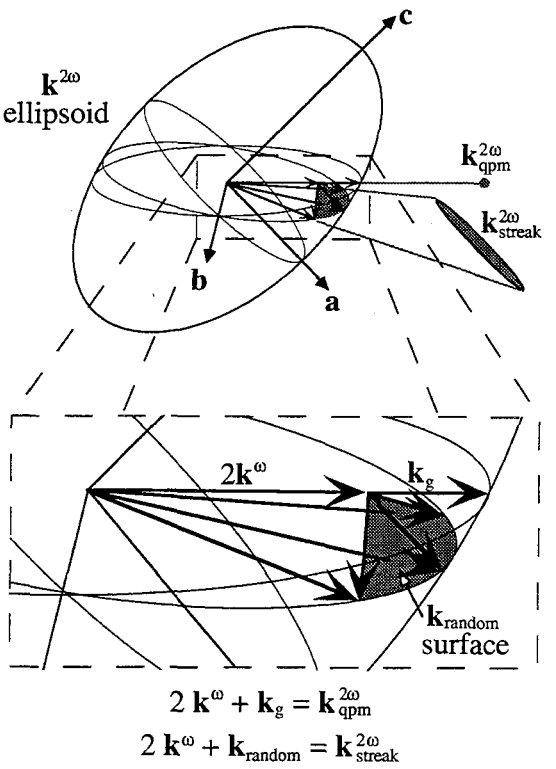

Figure 7.8: k space diagram illustrating origin of angular displacement of second harmonic spot (QPM contribution) and streak (random domain contribution).

This total second harmonic power in the streak can attain a value two orders of magnitude larger than the QPM spot, if the random depolarization of the crystal is more severe than the periodic depolarization. The random depolarization arises because each time a QPM grating is recorded, inverted microdomains form along those grating planes in which the space charge field is directed opposite to the spontaneous polarization. Instabilities in the spatial phase of the optical interference pattern (arising from temperature changes, for instance) tend to uniformly depole the crystal over time. Thus, the volume of uniformly distributed, inverted microdomains continues to increase as multiple holograms are exposed. In contrast, the domain modulation at the periodicity of the hologram compensates the instantaneous photorefractive space charge field. This spontaneous polarization modulation depth is small in comparison to the broadband distribution of periodicities arising from the accumulation of microdomains. The second harmonic conversion efficiency is enhanced by a factor of 1000 (to 1%) in an optically fatigued crystal, above the conversion in a poled crystal. Long term fringe stability (greater than hours) is necessary to maximize the periodic domain modulation while minimizing the uniform depolarization. In practice, this level of stability is extremely difficult to achieve.

Periodic depolarization is induced by the photorefractive space charge field to produce a narrow band SHG enhancement. This effect displays strong temperature dependence in SBN:61. By heating the crystal to within 20 ^{o}C of the ferroelectric phase transition, we find that the QPM enhancement, or equivalently the modulation of the spontaneous polarization, attains a maximum. Furthermore, the glassy ferroelectric properties of SBN is manifest in the observation of QPM-SHG above the ferroelectric phase transition temperature (figure 7.9). The origin of this effect is the alignment of micropolar regions in the paraelectric phase under the influence of the space charge field. In fact, micropolar regions are believed to exist up to temperatures as large as 300 ^{o}C [24]. However, the

quasi-phase matching enhancement observed here becomes extremely weak at temperatures in excess of 85 °C.

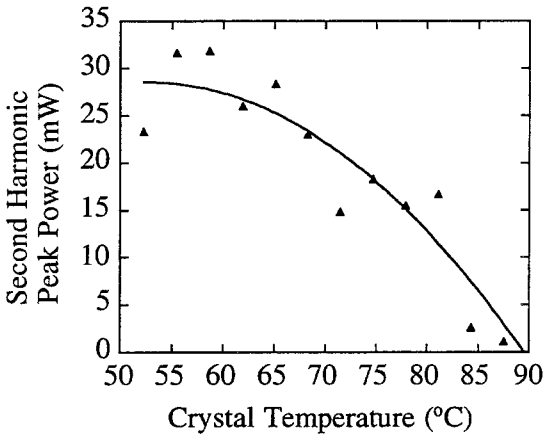

Figure 7.9: Temperature dependence of quasi-phase matching peak enhancement for gratings written with total intensity of 1 W cm^{-2} at 514.5 nm. Note the existence of QPM-SHG above the Curie temperature T_c = 75 °C.

The second harmonic power is dramatically enhanced by recording gratings in optically fatigued crystals; that is, crystals which have been exposed to significant optical energy (> 10^4 J cm^{-2}) at 514.5 nm (figure 7.10). The formation of random microdomains in the illuminated regions reduces the macroscopic spontaneous polarization by a factor of 3 to 10 (as indicated by the degradation of the electrooptic coefficient). The pre-existence of microdomains facilitates the subsequent domain grating formation. The small volume of microdomains (< 100 nm^3) lowers the energy required to invert an individual dipole. Furthermore, the reduction of electrical Barkhausen noise at this stage in the ferroelectric history of the crystal [25] suggests that the primary mechanism for depolarization is the sideways motion of domain walls under the action of the space charge field, rather than reversed domain nucleation.

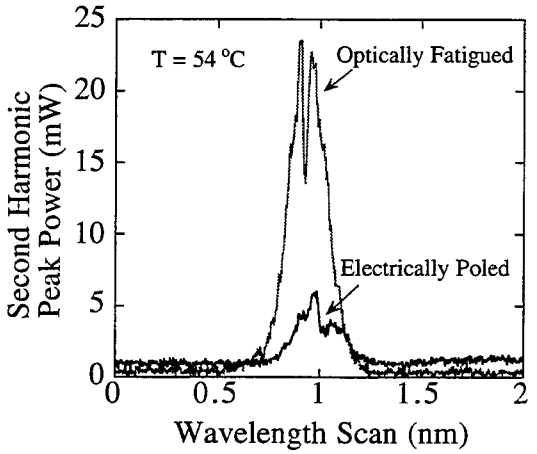

Figure 7.10: Enhancement of second harmonic peak in an optically fatigued crystal by high intensity exposure for ~ 3 hours, 1 W cm^{-2}. The noise features superimposed on peak are due to fluctuations in the interference grating.

Unlike earlier measurements performed in SBN:75 [13], a measurable remnant enhancement in second harmonic conversion efficiency is not observed in SBN:61. Apparently, the ferroelectric hysteresis for exposures and readout conducted at the same temperature (30 to 90 °C) is negligible in this material. To produce a significant remnant enhancement, the crystal must be cooled following the optical exposure to freeze-in a fraction of the dynamic domain grating [17].

7.6 Depth of Modulation of Spontaneous Polarization

The second harmonic power arising from a single coherence length (ℓ_c = 1.12 μm) slice of the crystal is predicted to be 0.1 mW from published values of the nonlinear optical susceptibilities [26]. The measured background second harmonic is ~ 1 mW, suggesting that the conversion efficiency is enhanced by the broad-band random domain contribution.

This power is centered on the QPM spot, and does not include the power contribution from the second harmonic streak. From the second harmonic power at the QPM peak (figure 7.11) the depth of periodic modulation of the spontaneous polarization is estimated. For instance, the measured peak second harmonic power of 30 mW translates into an effective crystal length of 40 coherence lengths. The spontaneous polarization is equivalently modulated by 1 %, so the effective nonlinear optic susceptibility induced by the space charge field is 0.06 pm V^{-1}. To attain conversion efficiencies of several percent at these fundamental beam intensities (17 MW cm^{-2}), the spontaneous polarization must be modulated by at least 20 %. The inset of figure 7.11 indicates the predicted second harmonic power as a function of the polarization modulation, expressed as a percentage of the room temperature spontaneous polarization.

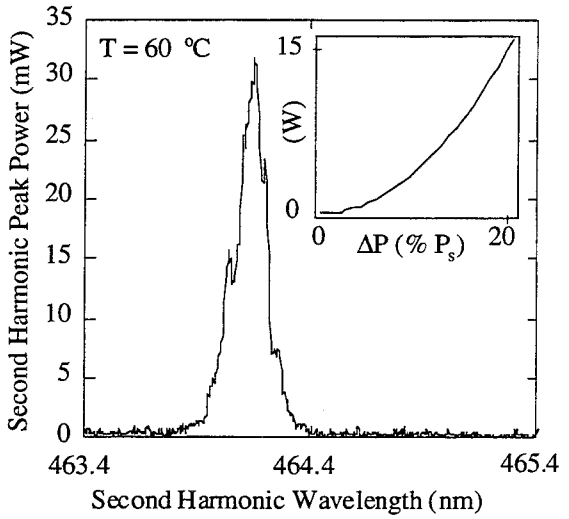

Figure 7.11: Typical quasi-phase matched tuning curve in SBN:60 at 60 °C for 3.25 micron grating written with a total intensity of 1 W cm^{-2}. Maximum conversion efficiency is 0.01 %. Inset: calculated second harmonic peak power as a function of the percent modulation of the spontaneous polarization (for a 17 MW cm^{-2} fundamental plane wave).

The modulation of the spontaneous polarization achieved during the relatively short optical exposures conducted here (typically less than 15 minutes) is limited by the mobile charge available to compensate the depolarization fields at head-to-head domain walls. The free carrier density required to compensate the non-zero divergence of the polarization, for a grating composed of domain walls whose surface normal is at 45 degrees to the c axis, is given by:

$$N_{comp} = \sqrt{2}\,\frac{\pi\,\Delta P}{q\,\Lambda_g}, \qquad 7.12$$

where ΔP is the polarization modulation amplitude at spatial periodicity Λ_g and q is the charge of an electron. The carrier density required to produce a field equal to the coercive field is:

$$N_{coercive} = \frac{2\sqrt{2}\,\pi\,\varepsilon\,E_{coercive}}{q\,\Lambda_g}, \qquad 7.13$$

where q is the charge of an electron and ε is the low frequency dielectric constant. For P_s equal to 25 $\mu C\ cm^{-2}$, $E_{coercive}$ equal to 1 $kV\ cm^{-1}$ (typical for SBN:61 at 45 °C) and a grating period of 3.25 micron, the compensating charge density required on the domain walls for *bipolar* modulation ($\Delta P = 2\ P_s$) is $N_{comp} \sim 10^{18}\ cm^{-3}$, and the coercive charge density is $4 \times 10^{16}\ cm^{-3}$. The charge should be localized about the domain walls, so significantly higher charge densities may be required (by a factor of 10). In the experiments described here, the small effective modulation of the spontaneous polarization (1%) indicates that the spatially periodic photoinduced space charge density is $\sim 10^{16}\ cm^{-3}$ to $\sim 10^{17}\ cm^{-3}$, depending on the degree of localization of the compensating charge. This suggests that further improvement in the QPM second harmonic powers can be attained by

tailoring the effective density of photorefractive traps to increase the space charge field without strongly increasing the absorption at the second harmonic wavelength.

7.7 Summary

The rapid enhancement in second harmonic power upon recording phase matching gratings further demonstrates that domain gratings exhibit a large dynamic component. Domain gratings can be recorded above the ferroelectric-paraelectric phase transition due to the glassy ferroelectric nature of SBN. The QPM-SHG is significantly enhanced by recording in optically fatigued rather than electrically poled crystals. The narrow band second harmonic is significantly weaker than the broadband second harmonic enhancement arising from the microdomain structure. The relatively small QPM-SHG conversion efficiencies are a consequence of the limited compensating charge available to screen the depolarization fields. Therefore, the primary effort to increase the degree of domain modulation should be directed at increasing the effective density of photorefractive traps through optimization of the dopant chemistry.

References for chapter seven

[1] A. Yariv, *Quantum Electronics* (Saunders College Publishing, Philadelphia, 1991).

[2] J. A. Armstrong, N. Bloembergen, J. Ducuing, P. S. Pershan, *Phys. Rev.* **127**, 1918 (1962).

[3] S. Somekh, A. Yariv, *Opt. Comm.* **6**, 301 (1972).

[4] J. A. Giordmaine, *Phys. Rev. Lett.* **8**, 19 (1962).

[5] P. K. Tien, *Appl. Opt.* **10**, 2395 (1971).

[6] N. Ming, J. Hong, D. Feng, *J. Mater. Sci.* **17**, 1663 (1982).

[7] C. J. van der Poel, J. D. Bierlein, J. B. Brown, S. Colak, *Appl. Phys. Lett.* **57**, 2074 (1990).

[8] E. J. Lim, M. M. Fejer, R. L. Beyer, *Electron. Lett.* **25**, 174 (1989).

[9] A. Feisst, P. Koidl, *Appl. Phys. Lett.* **47**, 1125 (1985).

[10] M. Horowitz, A. Bekker, B. Fischer, *Appl. Phys. Lett.* **62**, 2619-2621 (1993).

[11] H. Ito, C. Takyu, H. Inabe, *Electron. Lett.* **27**, 1221 (1991).

[12] J. Webjörn, F. Laurell, G. Arvidsson, *IEEE Photon. Technol. Lett.* **1**, 1989 (1989).

[13] A. S. Kewitsch, M. Segev, A. Yariv, G. J. Salamo, T. W. Towe, E. J. Sharp, R. R. Neurgaonkar, *Appl. Phys. Lett.* **64**, 3068-3070 (1994).

[14] A. S. Kewitsch, T. W. Towe, G. J. Salamo, A. Yariv, M. Zhang, M. Segev, E. J. Sharp, R. R. Neurgaonkar, *Appl. Phys. Lett.* **66**, 1865-1867 (1995).

[15] A. S. Kewitsch, M. Segev, A. Yariv, R. R. Neurgaonkar, *Opt. Lett.* **18**, 1262-1264 (1993).

[16] A. S. Kewitsch, M. Segev, A. Yariv, R. R. Neurgaonkar, *Jpn. J. Appl. Phys.* **32**, 5445-5546 (1993).

[17] A. S. Kewitsch, M. Segev, A. Yariv, G. J. Salamo, T. W. Towe, E. J. Sharp, R. R. Neurgaonkar, *Phys. Rev. Lett.* **73**, 1174-1177 (1994).

[18] M. M. Fejer, G. A. Magel, D. H. Jundt, R. L. Byer, *J. Quant. Elect.* **28**, 2631 (1992).

[19] E. L. Venturini, E. G. Spencer, P. V. Lenzo, A. A. Ballman, *J. Appl. Phys.* **39**, 343-344 (1968).

[20] M. Horowitz, A. Bekker, B. Fischer, *Appl. Phys. Lett.* **65**, 679-681 (1994).

[21] R. C. Miller, *Phys. Rev.* **134**, A1313 (1962).

[22] I. Freund, *Phys. Rev. Lett.* **21**, 1404 (1968).

[23] G. Dolino, *Phys. Rev. B* **6**, 4025 (1972).

[24] A. S. Bhalla, R. Guo, L. E. Cross, G. Burns, F. H. Dacol, R. R. Neurgaonkar, *J. Appl. Phys.* **71**, 5591 (1992).

[25] A. S. Kewitsch, A. Saito, A. Yariv, M. Segev, R. R. Neurgaonkar, *JOSA B* , in press (1995).

[26] Yamada, *Landolt-Börnstein New Series III*. T. Mitsuiand E. Nakamura, Eds., Ferroelectric Oxides (Springer Verlag, Berlin, 1990), vol. 28a.

Chapter Eight

Photopolymerization

8.1 Introduction

The process of linking individual monomer molecules into polymer chains is called polymerization. These chains can be joined along the backbone to form a crosslinked solid. This reaction is ubiquitous in the commercial production of plastics from precursors based on liquid monomers and oligomers. Polymerization and crosslinking are typically achieved by thermal initiation or photoinitiation. This discussion will focus on photoinitiation and on the nonlinear optical phenomenon arising upon photopolymerization. The chemistry of photopolymerization is described in detail in numerous texts [1-8]. This chapter will provide a brief review of photochemistry and polymerization.

8.2 Photoinitiated Polymerization

Light induced radical chain polymerization is a chain reaction initiated by UV generated reactive species. Most monomers do not produce initiating species with sufficiently high yield upon UV exposure, so a photosensitive initiator is introduced. Typical UV curable materials are made of at least two components: (1) a photosensitive initiator system that effectively absorbs the incident light and readily splits into reactive components and (2) a

monomer/oligomer containing at least two unsaturated bonds that will generate the polymer network.

The first step in the photoinitiation process is the absorption of a photon by a suitable chromophore and the promotion of a valence electron to an unoccupied molecular orbital. For a one photon absorption process, the energy E of the photon must be at least as large as the energy difference between the ground and the first excited singlet states of the molecule. Since most photoinitiators have a ΔE value above 350 kJ mol^{-1}, they will absorb strongly at wavelengths below 340 nm [9].

The electronic states of molecules are conveniently characterized in terms of the total electronic spin. A state with all spins paired is called a singlet state; one unpaired spin is a doublet state; two unpaired spins is a triplet state. While there are exceptions (e.g. O_2), in most ground-state molecules all electrons are paired (i.e., in the singlet state) [1]. A valence electron of the photoinitiator molecule is typically promoted to an excited singlet state upon absorption of a suitable photon. Excited singlet molecules are short-lived species (10^{-9} to 10^{-6} s) that decay by fluorescence, intersystem crossing and phosphorescence, or energy transfer.

One deactivation pathway of particular importance in photopolymerization is the intersystem crossing of the excited singlet state S_1 to the excited triplet state T_1 [10]. The excited triplet state is in turn deactivated by a radiative process or by a nonradiative intersystem crossing to the ground state. The energy level diagram of this process is depicted in the left half of figure 8.1, where the reactant is a photoinitiator. The right-hand side of this diagram will be discussed in the context of photosensitized reactions in section 8.4.

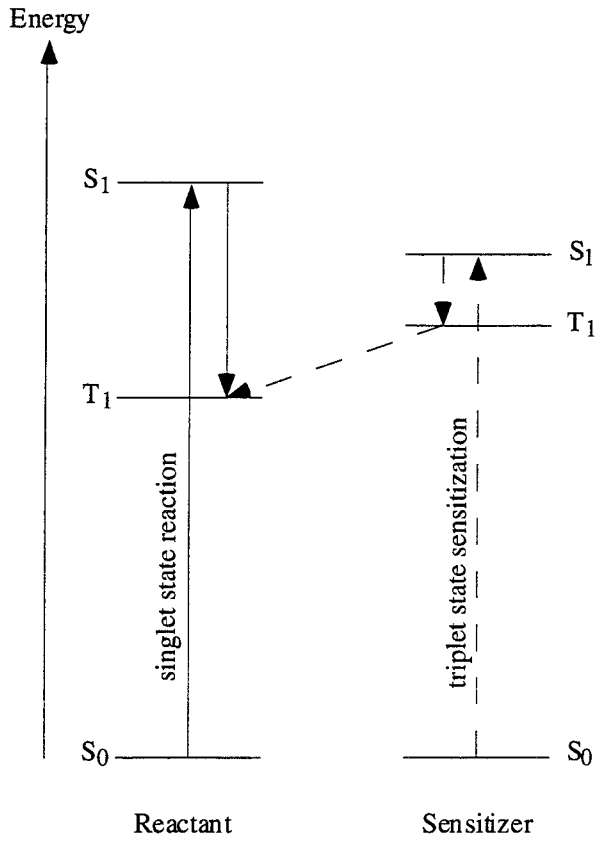

Figure 8.1: Energy level diagram typical for singlet excitation (solid lines) versus triplet sensitization (dashed lines).

Because of the long lifetime of the triplet state and the presence of two unpaired electrons, excited triplet states are more likely to undergo bond cleavage to form long lived radicals. The cleavage reaction is particularly important because it is responsible for the production of free radicals which will initiate either the degradation of an existing polymer or the crosslinking of a functionalized prepolymer. The bond breaking reaction can occur only if the photon energy exceeds the bond dissociation energy of one of the covalent bonds in the polymer. The bond dissociation energy of various bonds are summarized in table 8.1.

Bond Broken:	Bond Dissociation Energy (einstein kJ mol-1)
C-H	380 to 420
O-H	420
C-OH	380
C-C	340
C-O	320
C-Cl	320

Table 8.1: Typical bond dissociation energies [10].

Symbol:	Chemical Species:
$R\cdot$	Initiator Radical
M_m	Terminated Polymer of m Monomeric Units
$M_m\cdot$	Polymer Radical
PI	Photoinitiator
PS	Photosensitizer
PS^*	Excited State Photosensitizer
C	Chain Terminating Species

Table 8.2: Photopolymerization nomenclature.

The photoinitiators used in this study are based on the mechanism of photofragmentation. The absorption of a photon by a molecule promotes an electron from a bonding to an antibonding molecular orbital. Upon fragmentation, radicals are produced by the scission of a covalent bond:

$$PI + h\nu \rightarrow R_1\cdot + R_2\cdot \quad . \qquad 8.1$$

The nomenclature is described in table 8.2. For photofragmentation, the rate of radical generation at a particular location within the polymer depends on the extinction coefficient ε_λ, the local concentration of the photoinitiator [PI] and the local light intensity I [5]:

$$\frac{d[PI]}{dt} = -\varepsilon_\lambda I [PI] \quad . \qquad 8.2$$

Assuming the two radicals $R_1\cdot$, $R_2\cdot$ are identical, the rate of initiation is then given by

$$\frac{d[R\cdot]}{dt} = -2\frac{d[PI]}{dt} \quad . \qquad 8.3$$

In a liquid solution, the effective radical yields upon photodissociation are reduced by cage recombination. The solvent surrounding the initiator molecule at the moment of scission forms a molecular cage which must rearrange before the initiator fragments can physically separate. The cage keeps the fragments together for some time during which they may readily recombine. Only a fraction of the radicals produced in the scission event become available for reaction outside the cage [3, 11, 12]. The cage effect is responsible for the strong viscosity dependence of the initiation efficiency, for instance.

The probability of radical recombination in the solvent cage depends on the multiplicity of the excited state. An excited singlet state dissociates into radicals with antiparallel spins. Their recombination is spin allowed and may occur within the time of a single nuclear vibration (10^{-15} s). However, radicals formed from an excited triplet state have parallel spins and can recombine to a singlet state only after spin inversion, which requires a time

on the order of 100 ns [11]. Therefore, excited triplet states play the dominant role in photoinitiation.

8.3 Types of Photoinitiators

There are three primary classes of photoinitiators [7] used in industrial applications. In addition to the photocleavage mechanism described above, additional mechanisms are based on photoinduced hydrogen abstraction and photogeneration of acids. These materials are summarized below.

i. Photocleavage (Benzoin Ethers, Benzil Ketal, Acetophenones, Phosphine Oxide, Titanocene) This class includes aromatic carbonyl compounds that undergo a bond scission when exposed to UV light. The most commonly employed photoinitiators are benzoin ethers, which are highly efficient radical sources.

ii. Hydrogen abstraction (Benzophenone or related compounds with Amine, Thioxanthone, Camphorquinone, Bisimidazole) Aromatic ketones do not undergo fragmentation upon optical excitation. Instead, they "abstract" or borrow a hydrogen atom from another H-donor molecule. Tertiary amines often play the role of hydrogen donors.

iii. Cationic photoinitiators (Aryldiazonium salts, Arylsulfonium and Aryliodonium salts, Ferrocenium salts) Cations form free acids under illumination, which are efficient initiators for the polymerization of epoxy monomers by opening the epoxy ring to form chains. Chain propagation is initiated either by another cation or by a strong electophile, for example a Lewis acid (BF_3) or a

protonic Brønsted acid. Oxygen has no effect on cationic polymerization because the acids are oxygen insensitive. This is an important advantage for applications such as UV curable thin resists.

8.4 Photosensitized Polymerization

The response of the photopolymers can be shifted to the visible and infrared spectrum by using the electron-transfer reaction common among dyes. This is typically called photosensitized rather than photoinitiated polymerization. To achieve singlet energy transfer with a photosensitizer that absorbs at a longer wavelength than the reactant would require endothermic energy transfer, which is energetically improbable. However, it is often possible to find a sensitizer whose singlet excited state lies below that of the reactant, but whose triplet level lies above the triplet level of the reactant (figure 8.1). While in the context of section 8.3 the reactant was the photoinitiator, that is not necessarily the case for photosensitized polymerization.

Most sensitization processes in organic photochemistry are based on the following reaction:

$$S_0\,(\text{reactant}) + T^*(\text{sensitizer}) \rightarrow T^*(\text{reactant}) + S_0\,(\text{sensitizer})\ . \qquad 8.4$$

Since the overall spin of the system is conserved, the transfer process is spin allowed and occurs efficiently, as long as the transfer is exothermic (E_T (sensitizer) > E_T (reactant)). A photosensitizer such as a dye typically absorbs the optical energy,

$$PS + h\nu_2 \rightarrow PS^* \qquad 8.5$$

and subsequently transfers an electron to another molecule. Excimers and exciplexes are two types of molecular excitations that play an important role in the process of electron transfer. Excimers are formed by pairs of aromatic molecules that do not significantly interact in the ground state, yet become weakly bonded in the excited state. This bonding occurs between an excited state molecule and a ground state molecule of the same species. The origin of this bonding is the change of orbital symmetry that accompanies excitation and leads to orbital overlap and hence to bonding between the two systems. In the ground state the two molecules repel each other upon approaching within the distance of their van der Waals radii, but in the excited state the attractive force of the orbital overlap creates a potential energy well that leads to an energetically stable excimer state. The depth of the well is the excimer binding energy. This is the energy decrease relative to the energy of the excited state of an isolated (monomeric) molecule [3].

If two molecules differ significantly in their electron affinities, so that one may be regarded as an electron donor and the other as an electron acceptor, then the bonding process between these two molecules is accompanied by a partial transfer of charge. In this case the interaction is stronger than in conventional excimers and the transient excited species is called an exciplex (excited complex). Exciplexes lead to the complete transfer of an electron from one molecule to another and to the formation of radical ions [3].

Electron transfer in photosensitized reactions is often mediated by an exciplex. There are two prototypical sensitization mechanisms. In the first, an excited sensitizer PS^* functions as an electron acceptor. In the presence of a suitable electron donor D, the reduction of PS^* produces the donor cation radical D^+, which may be transformed into a species capable of initiation. It is also possible for excited sensitizers to act as electron donors for a suitable ground state electron acceptor A. The reduced acceptor A^- may then produce radical

initiators upon further reaction. In practice both types of sensitization have been observed. The first type is called photoreducible dye sensitization [13]:

$$PS^* + D \rightarrow PS^- + D^+ , \qquad 8.6$$

$$D^+ \rightarrow R\cdot . \qquad 8.7$$

The second type of sensitization by electron transfer employs a photooxidizable dye:

$$PS^* + A \rightarrow PS^+ + A^- , \qquad 8.8$$

$$A^- \rightarrow R\cdot . \qquad 8.9$$

The electron donor D and the electron acceptor A are sometimes referred to as activators or coinitiators. Typical classes of activators are amines (primarily tertiary amines), sulfinates, enolates, carboxylates, and organometallics [13]. Often the photoinitiator compounds described in the previous section also serve as effective activators or coinitiators.

Dye sensitization can occur not only by electron transfer, but also by energy transfer. Energy transfer is possible when two molecules are in close proximity. The molecule that carries excitation energy is distinguished as the energy donor (D), the other molecule as the energy acceptor (A). Energy transfer is accomplished by the interaction

$$D^* + A \rightarrow D + A^* , \qquad 8.10$$

where the * denotes that the molecule is in an excited electronic state. Energy transfer is an electronic process that occurs on the time scale of 10^{-15} seconds. It is energetically

favorable when the excitation energy of D^* is more than or equal to that of A^*. Two distinct coupling mechanisms are important in this process: coulombic or dipolar interaction (Förster) and electron exchange or orbital interaction (Dexter) [3].

8.5 Dipole Resonance Transfer

Energy transfer by coulomb interaction is a dipole radiation effect. The electronic transitions of two molecules couple in a manner similar to two oscillating dipoles. The radiation field produced by one molecule is absorbed by the other [14, 15]. The rate of energy transfer for this type of coupling is given by [3]:

$$k_{ET}(\text{coulombic}) = \frac{\mu_A^2 \mu_D^2}{r_{AD}^2}, \qquad 8.11$$

where k_{ET} is the rate constant, μ_A and μ_D are the transition dipole moments of the absorption (A-A^*) and fluorescence transition (D^*-D), and r_{AD} is the separation between the two molecular centers at the moment of interaction. This expression can be written in terms of measured quantities [16]:

$$k_{ET} = 8.8 \times 10^{-25} \frac{\kappa^2 \phi_F(D)}{n^4 r^6 \tau_D^0} \int_0^\infty f_D(\nu)\, \varepsilon_A(\nu) \frac{d\nu}{\nu^4}, \qquad 8.12$$

where n is the index of refraction, $\phi_F(D)$ is the quantum yield of fluorescence of the donor, τ_D^0 is the fluorescence lifetime of the donor in the absence of the acceptor and κ^2 is a geometric factor. In fluid systems, where the rotational relaxation time is shorter than the lifetime of the excited state, κ^2has a value of 0.67, while in a rigid medium it is 0.457 [3, 16]. $f_D(\nu)$ is the fluorescence spectrum of the donor normalized to unity, $\varepsilon_A(\nu)$ is the absorption spectrum of the donor (not normalized), and r is the separation between the two

molecules. In dipole resonance transfer the rate of energy transfer depends on the fluorescence intensity and on the fluorescence lifetime of the donor, as well as on the spectral overlap between the fluorescence of the donor and the absorbance of the acceptor. Because the energy transfer is carried by the electric field, Förster transfer does not require diffusional encounters between molecules, so it is relatively independent of solution viscosity.

8.6 Exchange Transfer

Exchange transfer is an alternate means of energy transfer between molecules that arises from the physical interaction between orbitals of the donor and acceptor (figure 8.2). The exchange mechanism requires orbital overlap between the donor and acceptor upon collisions. Exchange transfer occurs on almost every molecular encounter if the process is exothermic ($E_{D^*} - E_{A^*} < 0$) [3]. The exchange transfer is less sensitive to changes in spin multiplicity than resonance transfer, so it is dominant in triplet-to-singlet energy transfer [17].

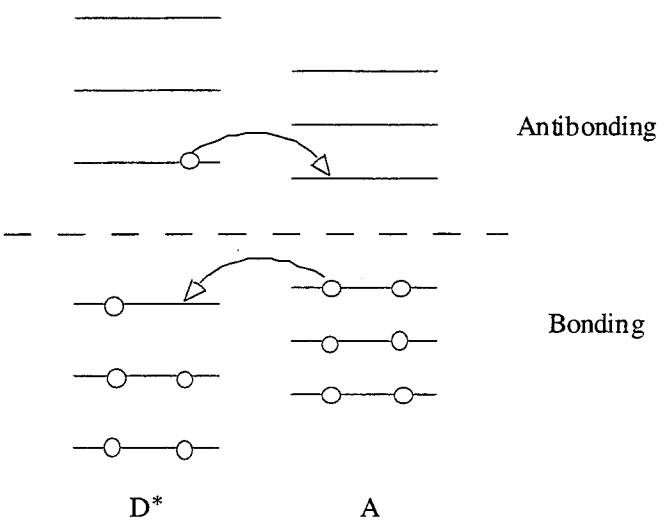

Figure 8.2: Energy transfer by electron exchange as represented by a Hückel orbital diagram [3].

8.7 Types of Photosensitizers

Photosensitizers typically exhibit the following properties [3]:

i. They have a high rate of intersystem crossing from S_1 to T_1 and consequently a high quantum yield ϕ_T of triplet formation.

ii. The energy difference between the singlet excited state S_1 and the triplet excited state T_1 (called singlet-triplet splitting) must be small.

iii. The triplet lifetime should be long to increase the probability of energy transfer between sensitizer and reactant.

iv. They should absorb strongly in a spectral region where the reactant does not absorb.

v. They must be soluble in the reaction medium (solvent or polymer matrix).

The majority of common sensitizers are either ketones or contain the carbonyl group. The $n\pi^*$ character of the excited states (triplet and singlet) of aromatic ketones favors intersystem crossing, high quantum yields, as well as small singlet-triplet splitting [3]. The $n\pi^*$ configuration is formed by promoting an electron from a nonbonding n orbital on oxygen into an antibonding π^* orbital that is delocalized over the aromatic π system. Charge delocalization produces a partial positive charge on oxygen that may interact with the electron rich C-H bond typical of the polymer backbone.

Several classes of photoreducible dyes have been identified: xanthene (eosin, fluorescein, Rose Bengal), thiazine (methylene blue, thionine), and acridinium dyes (acriflavin). The absorption maximum is centered on 460 nm for acridinium, 565 nm for xanthene, and 645 nm for thiazine [13]. The absorption α is also a function of time because of the formation

of light absorbing photoproducts (discoloration) and the destruction of the original chromophores (bleaching) responsible for absorption.

Photocrosslinking has been achieved with wavelengths as long as 632.8 nm, by using a dye such as methylene blue and toluenesulfinic acid. The dye is thought to be reduced by the sulfinate ion to form a radical which initiates acrylate polymerization [18, 19]. This reaction proceeds very slowly (1-2 days) in the absence of illumination. The initiating system is quite sensitive to illumination. The required exposure is as low as 0.6 mJ cm^{-2}. Therefore, photopolymerization can be induced by visible diode, He-Ne and Ar-ion lasers.

8.8 Chain Propagation

A dominant mechanism for the growth of polymer chains upon illumination is radical chain polymerization. The initiation of the polymer chain begins with the reaction of a radical with a monomer unit:

$$R\cdot + M \rightarrow M\cdot. \qquad 8.13$$

Once the monomer is radicalized, a chain reaction proceeds and the monomer grows into a polymer chain. This stage is called radical chain propagation, and is represented by the process:

$$M + M_m\cdot \rightarrow M_{m+1}\cdot. \qquad 8.14$$

The addition of a monomer molecule to the growing polymer chain can be represented by the conventional expression for the rate of a second-order reaction [5]. Since the only source of polymer molecules is chain propagation, and since neither polymer molecules nor

polymer radicals migrate significantly during the course of the reaction, the polymer radical concentration $[P\cdot]$ is given approximately by:

$$\frac{\partial[P\cdot]}{\partial t} = K_p[M]\sum_{j=1}^{\infty}[M_j\cdot] \ , \qquad 8.15$$

where

$$[P\cdot] \equiv \sum_{j=1}^{\infty}[M_j\cdot] \ . \qquad 8.16$$

K_p is the second-order rate constant, [M] the concentration of monomer, and $[M_j\cdot]$ the local concentration of polymer radicals of chain length j. Monomer molecules diffuse from regions of high monomer concentration according to the diffusion equation, including a monomer consumption term on the right [5]:

$$\frac{\partial[M]}{\partial t} = D_m\nabla^2[M] - K_p[M]\sum_{j=1}^{\infty}[M_j\cdot] \ . \qquad 8.17$$

D_m is the monomer diffusivity in the polymer matrix, which itself is a function of time because the polymer becomes more viscous upon crosslinking. Mass transport by convection or turbulence is ignored. The rate of chemical reactions in viscous media is influenced by the rate of diffusion of reagents towards one another. Radical polymerization reaction kinetics are diffusion controlled. Propagating polymer chains become very large and lose their mobility during polymerization. However, monomers continue to diffuse more or less freely. In the polymer matrix, the diffusivities of small molecules range from 10^{-6} to 10^{-10} $cm^2\ s^{-1}$, while the diffusivity of the polymer species ranges from 10^{-11} to 10^{-13} $cm^2\ s^{-1}$ [5].

8.9 Chain Termination

In theory one absorbed photon may polymerize the entire monomer solution, since one radical R · can join an infinite number of monomers. In practice, this reaction is terminated at some intermediate stage by chain termination agents C. This limits the mechanical strength of the crosslinked polymer, for instance. The mechanism of chain termination is an important factor in the spatial resolution of polymeric microstructures. A quantitative theory is essential to model this process and address issues such as resolution, contrast, and index of refraction change. The elementary results which comprise this section are based primarily on chapter five of the text by Krongauz [5].

Chain termination is represented by the following process:

$$C + M_m\cdot \rightarrow C\cdot + M_m \quad . \tag{8.18}$$

Oxygen inhibition is a common mechanism for chain termination. It leads to a threshold energy for photopolymerization (an induction period) and a reduced rate of polymerization or crosslinking. This occurs by two processes. The photoinitiator radical may be deactivated by oxygen:

$$R\cdot + O_2 \rightarrow ROO\cdot \quad , \tag{8.19}$$

or the polymer chain may be terminated by oxygen directly:

$$O_2 + M_m\cdot \rightarrow M_mOO\cdot \quad . \tag{8.20}$$

Oxygen inhibition has the desirable effect of scavenging the diffusing photoinitiator, which improves the spatial contrast between cured and uncured regions. In the absence of oxygen, chain termination is dominated by radical occlusion. The radicals are trapped at locations where no reaction partners (monomers) are available. Radical-radical chain termination is usually ignored because the mobility of growing polymer chains is orders of magnitude lower than that of monomer molecules.

The oxygen triplet ground state exhibits a high reactivity with excited states and free radicals because of oxygen's biradical nature. It deactivates both singlet and triplet excited states by an energy transfer process:

$$S^* + O_2 \rightarrow S + O_2^* \quad , \qquad 8.21$$

$$T^* + O_2 \rightarrow T + O_2^* \quad . \qquad 8.22$$

In air saturated systems, effective scavenging by oxygen occurs only if the radical lifetime is larger than 10^{-7} s, which is typically the case in polymers. Otherwise, the lifetime of the radical is not sufficient to come into contact with oxygen. If a chain transfer agent C and oxygen are free to diffuse within the polymer matrix, then the chain-termination rate is expressed as:

$$\frac{d[P]}{dt} = \{K_T[O_2] + K_{CT}[C]\} \sum_{j=1}^{\infty} [M_{j\cdot}] \quad , \qquad 8.23$$

where K_T and K_{CT} are the second order rate constants of the chain termination by O_2 and by a chain terminating agent, respectively, and [P] is the concentration of terminated polymer. The fraction of radicals that succeed in initiating polymerization is denoted by f_i:

$$f_i = \frac{K_r[M]}{K_r[M] + K_{CT}[C] + K_T[O_2]} \quad , \qquad 8.24$$

where K_r is the rate constant for radical initiation, the reaction described by equation 8.13. By comparing equation 8.23 and 8.15, it is apparent that chain propagation dominates the early stages of the photopolymerization reaction when the concentration of monomer is high, while chain termination dominates the latter stages of the reaction when the concentration of polymer radical is high.

The diffusivity of oxygen, D_T, is higher than that of the monomer because of its smaller size. Therefore, polymerization would not occur if oxygen solubility in the film were high. Fortunately, the usual photopolymer oxygen solubility is quite low ($< 3\ 10^{-6}$ mol cm^{-3}) [5]. The concentration of oxygen and the chain terminating agent are given by diffusion equations:

$$\frac{\partial[O_2]}{\partial t} = D_T \nabla^2 [O_2] - K_T [O_2] \sum_{j=1}^{\infty} [M_{j\cdot}] \qquad 8.25$$

and

$$\frac{\partial[C]}{\partial t} = D_{CT} \nabla^2 [C] - K_{CT} [C] \sum_{j=1}^{\infty} [M_{j\cdot}] \, . \qquad 8.26$$

Oxygen can be scavenged from the polymer by reacting with tertiary amines. Amines are very effective as hydrogen donors and consume oxygen in a chain reaction. This reaction is able to consume up to 12 molecules of oxygen with 12 amine molecules, with the loss of

only one radical M · [20]. Tertiary amines are commonly added to the photopolymer system as antioxidants.

Several mechanisms reduce the rate of photopolymerization. Additives exploiting these mechanisms are called photostabilizers. There are five primary types [9]:

i. UV screeners: prevent absorption of incident light by the polymer
ii. UV absorbers: compete with the polymer for absorption of light
iii. Quenchers: deactivate the excited states formed in the polymer
iv. Radical scavengers: react with alkyl, alkoxy, and peroxy radicals
v. Peroxide decomposers: suppress the chain branching process

The latter three types of photostabilizers may be added to the photopolymer system to reduce unwanted polymerization in dark regions due to radical diffusion. While this improves the spatial resolution of the photopolymer system, it also reduces the light sensitivity.

8.10 Kinetic Model of Polymerization

The local concentration of the polymer can be determined as a function of time by modeling the processes of initiation, propagation and termination. The goal is to ultimately determine the index of refraction from the polymer concentration as a function of space and time. This requires the simultaneous solution of the chemical rate equations, the diffusion equations, and the wave equation in an inhomogeneous medium. In chapter nine a relatively simple, approximate expression for the index evolution is used, which is solved numerically in chapter eleven.

For a more exact treatment of the kinetics of polymerization, the evolution of the polymer radical concentration $[P\cdot]$ must be evaluated. The evolution in time is given by [5]:

$$\frac{\partial[P\cdot]}{\partial t} = 2\frac{\partial[PI]}{\partial t} - \{K_T[O_2] + K_{CT}[C]\}\ P\cdot \quad . \qquad 8.27$$

The initiator, monomer and polymer absorb light within the medium. Since chemical reactions and diffusion change the distribution of the absorbing species, the local light intensity also changes upon illumination:

$$\frac{\partial[I]}{\partial t} = -I\left\{\varepsilon_{PI}[PI] + \varepsilon_M\left([P] + [P\cdot] + [M] + [M\cdot]\right) + \sum_k \varepsilon_k[Q_k]\right\} \quad , \qquad 8.28$$

where $[Q_k]$ is the concentration of the *k*th component of the reactive mixture and ε_k is the extinction coefficient of the *k*th component. The extinction coefficient ε_M of the monomer and polymer are assumed to be identical. These equations can be solved numerically to determine the local concentration of polymer at any time. The relative concentration of polymer is typically linearly proportional to the density. We can then model the time evolution of the index of refraction exactly by relating the density change to the index of refraction change. This will be the subject of future studies.

8.11 Summary

Photopolymerization is a technique of great practical and commercial importance. This reaction is also of interest in nonlinear optics because dramatic and permanent index changes are generated with low optical exposures. As the monomer crosslinks, the density of polymer increases and the index tends to increase. However, the change in absorption

upon illumination also introduces large index changes. The factors which determine the index change are described in the next chapter.

References for chapter eight

[1] T. H. Lowry, K. S. Richardson, *Mechanism and Theory in Organic Chemistry.* (Harper & Row, New York, 1987).

[2] G. Odian, *Principles of Polymerization.* (Wiley, New York, 1981).

[3] A. Reiser, *Photoreactive Polymers The Science and Technology of Resists.* (Wiley, New York, 1989).

[4] D. Volman, G. S. Hammond, K. Gollnick, Eds., *Advances in Photochemistry* , vol. 13 (Wiley, New York, 1986).

[5] V. V. Krongauz, A. D. Trifunac, Eds., *Processes in Photoreactive Polymers* (Chapman & Hall, New York, 1995).

[6] M. Koizumi, S. Kato, N. Mataga, T. Matsuura, Y. Usui, *Photosensitized Reactions.* (Kagakudojin Publishing Co., Kyoto, 1978).

[7] C.-H. Chang, A. Mar, A. Tiefenthaler, D. Wostratzky, in *Handbook of Coatings Additives* L. J. Calbo, Ed. (Marcel Dekker, Inc., 1992), vol. 2, pp. 1-43.

[8] N. S. Allen, Ed., *Photopolymerisation and Photoimaging Science and Technology* (Elsevier Applied Science, London, 1989).

[9] C. Decker, in *Handbook of Polymer Science and Technology* N. P. Cheremisinoff, Ed. (M. Dekker, New York, 1989), vol. 3, pp. 541-608.

[10] B. Rånby, J. Rabek, *Photodegradation, Photooxidation and Photostabilization of Polymers*. (Wiley, London, 1975).

[11] J. Franck, E. Rabinowitch, *Trans. Faraday Soc.* **30**, 120 (1934).

[12] R. M. Noyes, *J. Am. Chem. Soc.* **77**, 2042 (1955).

[13] D. F. Eaton, in *Advances in Photochemistry* D. Volman, G. Hammond, K. Gollnick, Eds. (Wiley, New York, 1986), vol. 13, pp. 427-487.

[14] T. Förster, *Ann. Phys.* **2**, 55 (1953).

[15] T. Förster, *Discuss. Faraday Soc.* **27**, 7 (1959).

[16] M. Z. Maksimov, I. B. Rotman, *Opt. Spectrosc.* **12**, 237 (1962).

[17] P. J. Wagner, *Creat. Detect. Excited State* **1A**, 174 (1977).

[18] Jenny, *J. Opt. Soc. Am.* **60**, 1155 (1970).

[19] J. A. Jenny, *J. Opt. Soc. Am.* **61**, 1116 (1971).

[20] R. F. Bartholomew, R. S. Davidson, *J. Chem. Soc. Chem. Commun.* , 2347 (1971).

Chapter Nine

Index Changes Upon Photopolymerization

9.1 Introduction

Permanent changes in the optical index of refraction as large as 0.3 may be induced by photochemical reactions, with typical values equal to 0.04. For instance, crosslinking increases the density of the polymer. The change in index of refraction is typically linearly proportional to the fractional density change. Photopolymerization provides a tool to permanently tailor the optical and structural properties of the material on the microscopic scale. The application of this technique to self-focusing and self-trapping optical beams is of particular interest.

9.2 Index of Refraction of Polymer

The Lorentz-Lorenz relation relates the index of refraction of an isotropic material to the optical polarizability P per unit volume:

$$\frac{n^2 - 1}{n^2 + 2} = \frac{4}{3}\pi P \ . \qquad 9.1$$

This relation holds for relatively high densities of the liquid and solid phase, and is accurate to within a few percent for nonpolar molecules in the transparent region of the optical

spectrum [1]. The polarizability may be expressed in terms of the polarizability α_i per molecule i. For an ideal mixture of j components, with no interactions among components,

$$\frac{n^2 - 1}{n^2 + 2} = \frac{4}{3}\pi \sum_j \frac{N_j \rho_j \alpha_j}{M_j}, \qquad 9.2$$

where M_j is the molecular weight, ρ_j is the density and N_j is the number of molecules in each component j. The refractivity of component j is defined as $4\pi N_j \alpha_j/3$. Equation 9.2 addresses three basic ways to change the index of refraction:

i. The polarizabilities of the individual molecules α_j can be altered by chemical reactions.

ii. The density of the components can be changed by altering the molecular structure. For instance, photopolymerization changes molecular packing and induces substantial density changes.

iii. The relative concentrations of the various components of the sample can be altered. This requires the addition or removal of material. To get a large refractive index change, one must alter the relative concentrations of components that have significantly different indices of refraction (e.g., remove uncured liquid from sample).

Accurate estimates of the molecular polarizability based on measured bond polarizabilities have been computed. For example, in diacrylate and triacrylate monomers, the electronic polarizability decreases upon polymerization because a double bond is replaced by two single bonds. As described in chapter three, the highly covalent double bond has more bond charge whose position will be perturbed by the optical field. However, polymerization results in a substantial increase in density, since van der Waals interactions between molecules are replaced by covalent bonds which draw individual monomer units

together into a solid polymer network. The majority of monomer-polymer systems share the property of giving polarizability and density contributions to the index change of opposite signs, yet in many the density change is dominant.

A density change $\Delta\rho$ produces an index change [2]:

$$\Delta n = \frac{(n^2 + 2)(n^2 - 1)}{6\,n}\frac{\Delta\rho}{\rho}\,. \qquad 9.3$$

For n = 1.5, this gives $\Delta n = 0.59\ \Delta\rho/\rho$. The largest density changes are associated with changes in molecular packing. This is maximized for reactions of small molecules, in which the reactive bonds constitute a larger fraction of the molecule. For example, the density change upon polymerization of a relatively small molecule such as methyl methacrylate (M = 100) produces a fractional density change $\Delta\rho/\rho$ of 0.254 (see table 9.1). Methyl methacrylate exhibits a fractional index change $\Delta n/n$ upon polymerization of +0.052. Photochemical reactions are unlikely to produce density changes in excess of $\Delta\rho/\rho \approx 0.5$, corresponding to a Δn of 0.3. By removing the uncured liquid photopolymer using a solvent, it is possible to achieve an index change as large as 0.7 between the solid and air, since the index of typical organic solids is in the range of n ~ 1.4 to 1.7.

Monomer:	MW	Monomer Density	Polymer Density	$\Delta\rho/\rho$
Acrylonitrile	53	0.880	1.35	0.534
Vinyl chloride	62.5	0.919	1.41	0.534
Methyl acrylate	68	0.952	1.32	0.387
Vinyl acetate	86	0.934	1.19	0.274
Methyl methacrylate	100	0.940	1.179	0.254
Styrene	104	0.909	1.068	0.175
n-propyl methacrylate	142	0.902	1.049	0.163
Cyclohexyl methacrylate	168	1.030	1.142	0.109

Table 9.1: Fractional density change upon photopolymerization. The density change data is compiled from Ref.[3].

The index of refraction of polymers before and after curing is not typically measured. However, extensive work has been performed to characterize the volume shrinkage of polymers upon crosslinking [3-6]. From equation 9.3, the index change can be deduced from the volume shrinkage. Acrylates exhibit more shrinkage than epoxies. The volume shrinkage is reduced in a system for which the polymerization propagates through ring opening, such as epoxies, because the unfolding of the ring counteracts the increase in density upon crosslinking. Therefore, epoxies typically have shrinkage factors of less than 5%.

9.3 Index of Refraction of Photoinitiator

The mass fraction of the photoinitiator relative to the polymer/monomer background can range from more than 1 to typically less than a 0.01. High concentrations of photoinitiator

are feasible if the absorption exhibits photobleaching at the curing wavelength and if the photoinitiator is sufficiently soluble in the polymer liquid. The light intensity as a function of depth in a bleachable photoinitiator is [7]:

$$I = \frac{I_o}{[1 - \exp(-\kappa \mu I_o t)(1 - \exp(\mu c_o x))]} , \qquad 9.4$$

where I_o is the incident intensity (erg cm^{-2} sec^{-1}), μ is the absorption coefficient (cm^2 mol^{-1}), c_o is the initial concentration of the absorber (mol cm^{-3}), and κ is the photochemical efficiency of the reaction. Figure 9.1 illustrates the theoretical light intensity as a function of propagation depth z at different times t. Individual layers of polymer as thin as the absorption length may cured, a distance which may be less than an optical wavelength [8].

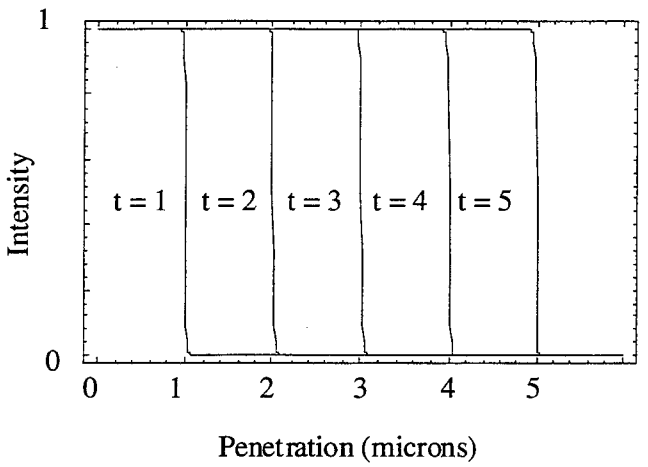

Figure 9.1: Theoretical intensity distribution at different times in a medium which exhibits photobleaching. The extinction coefficient is 0.1 microns.

The contribution to the index change arising from photobleaching is related to the absorption change through the Kramers-Kronig relations [9]. For wavelengths longer than the center wavelength of the optical transition (for instance, 475 nm for CGI 784

photoinitiator), the index increases upon photobleaching (figure 9.2). Therefore, for the Ar-ion optical beam at 488 nm or 514.5 nm, the structural index change upon solidification and the index change due to photobleaching are both positive. Alternately, operating at wavelengths below the center wavelength results in a reduced index change which can be either positive or negative upon exposure.

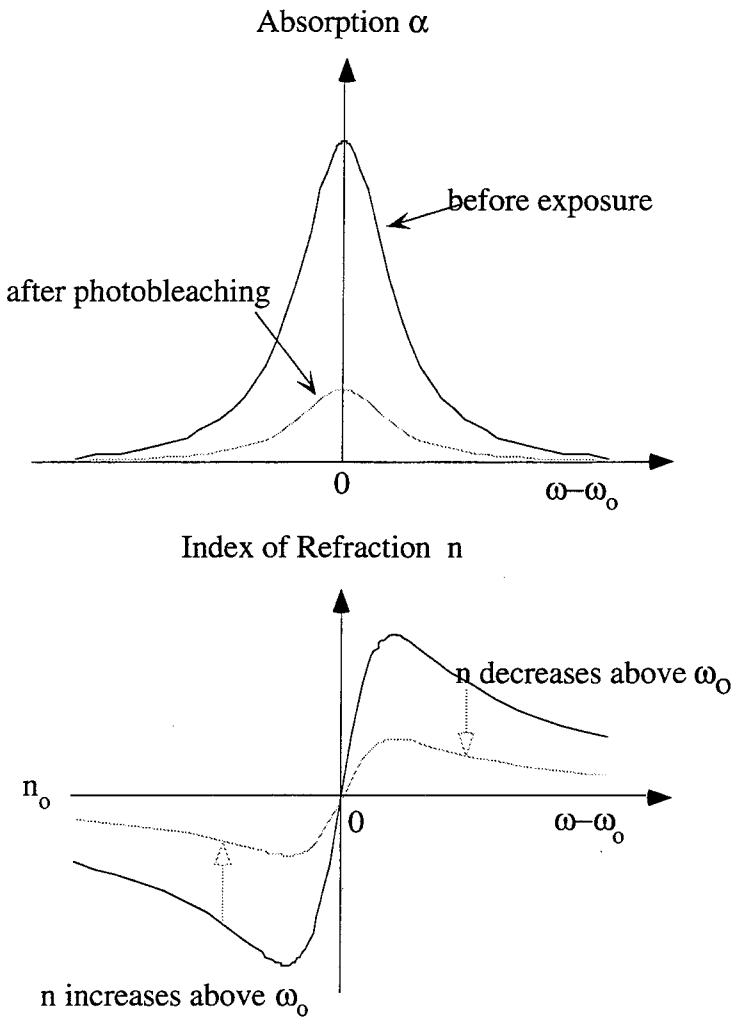

Figure 9.2: Index change due to photobleaching of photoinitiator.

The intrinsic absorption of the monomer/polymer typically is not photobleachable. In fact, the ring structure of epoxies results in strong absorption by the polymer in the UV spectrum, leading to very small cure depths. Polymers are classified according to their intrinsic absorption in table 9.2. The near UV cutoff which distinguishes the two classes of materials is approximately 290 nm.

Polymers not absorbing in near UV	Polymers absorbing at near UV
Polyolefins	Polyphenoxy
Polyacrylics	Polyethersulfones
Polystyrenes	Polycarbonates
Poly(vinyl chloride)	Polyphenylene oxide
Polydienes	Aromatic polyesters
Polyesters	Aromatic polyurethanes
Aliphatic polyamides	
Aliphatic polyurethanes	
Aliphatic polyethers	

Table 9.2: Absorption characteristics of some common polymers [10].

9.4 Dynamic Model of Index Change Upon Photopolymerization

To model the time evolution of the refractive index, the shrinkage or density change is taken to be proportional to the degree of polymerization:

$$\frac{\Delta\rho}{\rho} = \beta \frac{[P]_t}{[M]_{t=0}}, \qquad 9.5$$

where β is a constant indicating the degree of volume shrinkage. Using equation 9.5 in addition to the rate equations for [P] discussed in chapter eight, the local index of refraction can be determined at all times.

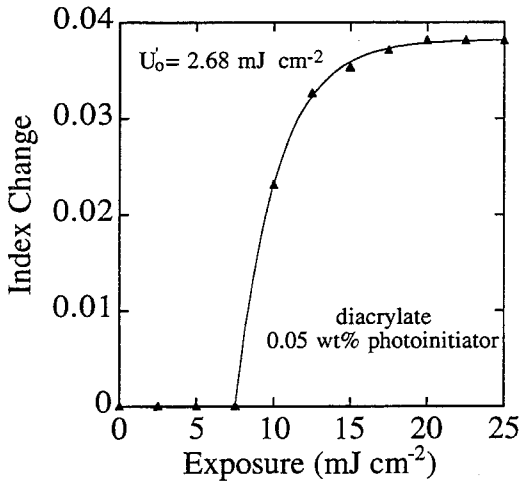

Figure 9.3: Measured change in index of refraction (at 589.3 nm) of the diacrylate photopolymer under UV exposure at 325 nm. The curve fit is given by equation 9.6 with U_o' (in energy units) equal to 2.68 mJ cm^{-2}.

9.5 Measured Evolution of the Index of Refraction

The index variation with time is expected to display three distinct responses. During the first stage, at small times or small exposures, the polymer chains are still small (< 10 monomer units). The bonding of two small chains induces only a small density and index of refraction change. The photoinitiation efficiency is also small during the early stage of the exposure because most of the radicals are scavenged by the highly reactive oxygen radicals [11]. This corresponds to the initial flat induction period in figure 9.3 for

exposures less than 7.5 mJ cm^{-2}. During the second stage, larger polymer chains are formed, so the crosslinking between two adjoining large molecules occurs at several sites. This induces a more rapid increase in the index. The third stage exhibits saturation of the index change, occurring near the end of crosslinking. The polymer chains have reached their maximum length (typically > 10,000 units) and the efficiency of photopolymerization is reduced because of the cage effect, in which the large viscosity restricts the movement of radicals [11].

The complex index of refraction $n = n' + n''$ is composed of a real part representing the index of refraction and an imaginary part representing absorption. The real and imaginary parts of the index can be solved numerically from equation 9.5 assuming that the index change due to photobleaching of the absorption is relatively small. An analytical solution to the chemical rate equations does not exist. However, experimental observations, such as that presented in figure 9.3, indicate that the index response can approximated by:

$$\Delta n'(x,y,z,t) = \Delta n'_o \left[1 - \exp\left(- \frac{1}{U'_o} \int_0^t |E(t')|^2 dt' \right) \right] \quad . \qquad 9.6$$

The expression for absorption photobleaching is approximately:

$$\Delta n''(x,y,z,t) = \Delta n''_o \exp\left(- \frac{1}{U''_o} \int_0^t |E(t')|^2 dt' \right) \quad . \qquad 9.7$$

Note that the index and absorption display different critical exposures U'_o and U''_o, respectively, which in general depend on time because of the dramatic increase in polymer viscosity during chain growth. The absorption change occurs very rapidly, since the characteristic time of optical excitation and bond cleavage of the photoinitiator molecule is on the order of 10^{-15} sec. However, the rate of index change generated by chain

propagation and crosslinking is determined by the diffusion time of the radical within the viscous polymer network to an appropriate monomer unit. In fact, from the measured index time response, we can infer that the lifetime of the radicals successful in initiating polymerization is approximately 250 ms for low monomer conversion. This lifetime for high monomer conversion (i.e., when the index change is 0.9 of the maximum index change) is in excess of 30 seconds. Note that equation 9.6 neglects the induction period apparent for small exposures in figure 9.3, because the exposure threshold is reduced in our experiments by minimizing oxygen scavenging of photogenerated radicals. The curve fit of equation 9.6 for constant critical exposure $U_o^{'}$ displays good correlation with the data presented in figure 9.3, for exposures below 30 mJ cm^{-2}. Beyond this exposure, the viscosity increases dramatically, so $U_o^{'}$ and $U_o^{''}$ both depend strongly on time.

9.5 Summary

The index change upon photopolymerization is large enough to produce dramatic nonlinear optical effects such as self-focusing and self-trapping of optical beams. The time response of the index change is an important material consideration. The index must change rapidly enough to begin to guide the optical beam before a large number of photogenerated radicals are produced outside the waveguide. The index change displays an absorbed energy dependence similar to the photorefractive effect.

References for chapter nine

[1] M. V. Klein, T. E. Furtak, *Optics.* (Wiley, New York, 1986).

[2] W. J. Tomlinson, E. A. Chandross, in *Advances in Photochemistry* J. J. N. Pitts, G. S. Hammond, K. Gollnick, Eds. (Wiley, New York, 1985), vol. twelve, pp. 201-281.

[3] J. S. Arney, L. Sanders, R. Hardesty, *J. of Imaging Sci. and Tech.* **38**, 262-268 (1994).

[4] J. d. Boer, R. J. Visser, G. P. Melis, *Polymer* **33**, 1123-1126 (1992).

[5] P. Karrer, S. Corbel, J. C. Andre, D. J. Lougnot, *J. Polymer Sci.:Part A: Polymer Chem.* **30**, 2715-2723 (1992).

[6] A. M. Duclos, J. Y. Jézéquel, J. C. André, *J. Photochem. Photobiol. A: Chem.* **70**, 285-299 (1993).

[7] J. H. C. Kessler, *J. of Phys. Chem.* **71**, 2736-2737 (1966).

[8] N. Bühler, *Chimia* **47**, 375-377 (1993).

[9] A. Yariv, *Quantum Electronics.* (Wiley, New York, 1989).

[10] C. Decker, in *Handbook of Polymer Science and Technology* N. P. Cheremisinoff, Ed. (M. Dekker, New York, 1989), vol. 3, pp. 541-608.

[11] G. Odian, *Principles of Polymerization.* (Wiley, New York, 1981).

Chapter Ten

Introduction to Self-Trapping and Self-Focusing

10.1 Introduction

Self-trapping and self-focusing of optical beams based on the Kerr effect are familiar phenomena extensively reported in the literature. Self-focusing describes the formation of a light-induced lens within the nonlinear medium. Self-trapping occurs when this self-focusing exactly balances diffraction, so the beam maintains a constant diameter as it passes through the medium. The conditions under which an optical beam is self-trapped due to the Kerr effect were first described by Ciao et al. [1]. In a Kerr medium, the index of refraction is dependent on the optical field amplitude E through the relation:

$$n = n_0 + n_2 E^2 \quad . \tag{10.1}$$

For media with positive Kerr constants n_2, the index increases in regions of high optical intensity. This induces waveguiding of the original optical beam, which balances diffraction. For instance, if the beam diameter is D, the beam expands by diffraction in a homogeneous media with an angular divergence given by

$$\theta \approx 1.22 \frac{\lambda}{n_0 D} , \tag{10.2}$$

where λ is the wavelength of light in vacuum. If the critical angle for total internal reflection at the interface between the bright and dark regions of the transverse intensity profile is greater than θ given by equation 10.2, then spreading by diffraction is absent. The transverse intensity profile of the beam will remain constant, independent of the propagation distance. By definition this is called self-trapping. In general, the diameter of a trapped beam may be slightly modulated as if the waveguiding were due to a periodic sequence of convex lenses; however, the average diameter along the propagation direction is constant. For small angles, the beam will be trapped for powers P greater than:

$$P = \frac{\pi D^2}{4}\frac{n_0 E^2 c}{8\pi} \geq (1.22\,\lambda)^2 \frac{c}{64\,n_2} \quad . \qquad 10.3$$

For typical materials, the critical power for trapping is believed to be within one or two orders of magnitude of 10^6 W. As we will see later, no critical power is needed for self-trapping in photopolymers, because the index change depends on optical exposure rather than intensity.

The Fresnel diffraction equation for the electric field amplitude E with wavevector k, in a Kerr medium with small index modulation n_2, is:

$$2ik\frac{\partial E}{\partial z} + \frac{\partial^2 E}{\partial x^2} + 2k^2 n_o n_2 |E|^2 E = 0 \; . \qquad 10.4$$

Note that we are dealing with trapping in one transverse direction only (i.e., x) to simplify the analysis. These results will readily generalize to trapping in two dimensions. The trapped solution (i.e., dE/dz =0) to equation 10.4 is:

$$E_t(x) = E_t(0)\,\mathrm{sech}^2 \Gamma x \;\; , \qquad 10.5$$

where

$$\Gamma = \frac{1}{2} n_2 k_0 E_t(0) \ . \qquad 10.6$$

Closed form analytical solutions to equation 10.4 demand overly restrictive assumptions. This dilemma will be even more apparent for trapping in photopolymers. For instance, equation 10.4 ignores the effect of saturation of the index of refraction. A more realistic analysis requires a numerical simulation. Reference [2] presented a numerical analysis for beam propagation in a Kerr like medium with a saturable, intensity dependent refractive index. The modified Fresnel equation used in this study is:

$$2ik\frac{\partial E}{\partial z} + \frac{\partial^2 E}{\partial x^2} + \frac{2k^2 n_o n_2 |E|^2 E}{1 + |E/E_s|^2} = 0 \ . \qquad 10.7$$

Equation 10.7 possesses solutions which exhibit both self-focusing and trapping. It is common for the beam diameter to oscillate and produce periodic foci. The distance between adjacent foci is given by:

$$z_s = \pi \, k \, a_s^2 \frac{(P/P_{cr})^{1/4}}{\left[(P/P_{cr})^{1/2} - 1\right]^{3/2}} \ , \qquad 10.8$$

where

$$(a_s/a_o)^2 = 0.273 \ (P/P_{cr}E_s^2) \ . \qquad 10.9$$

As the beam propagates, the refractive index near the axis rises until saturation. The resultant induced "convex lens" is flat in the center and therefore tends to focus incoming

(still nearly parallel) rays into a ring. This produces a characteristic ring-like transverse intensity distribution, rather than the typical TEM_{oo} profile.

The filaments of optical damage observed experimentally in inorganic crystals have been explained both by a self-trapping and by a transient self-focusing mechanism. Shen [3] reported that small scale filaments were composed of a continuous series of focal spots. These observations are consistent with a model based on a time varying focal length. Lugovoi and Prokhorov [4] also suggested that in some situations filaments are simply tracks of moving foci, in accordance with the time variation of the input laser intensity during an individual pulse. Shen's observations of a 50 micron diameter beam producing filaments of 10 micron diameter in toluene and 5 microns in CS_2 support this moving foci picture. The finite length of the filament is attributed to the depletion of the incoming laser power arising from stimulated backward Raman and Brillouin scattering. For a certain laser power P the focal spot appears at the self-focusing distance [5]

$$z_f = \frac{k}{\left[(P/P_{cr})^{1/2} - 1\right]} \quad . \qquad 10.10$$

P_{cr} is the critical power for saturation of the Kerr effect. The position of the focal spot is then a function of the input laser power, which moves as the power within the pulse changes.

Recently, optical beams have been self-trapped using the Kerr effect in sodium vapor [6] and a planar glass waveguide [7]. Self-trapping has also been achieved at low optical intensities by the photorefractive effect, in which diffraction is balanced by two wave mixing among the spatial frequency components of the input beam [8-10].

10.2 Wave Equation in Inhomogeneous Medium

The photopolymerization reaction leads to a significant increase in the index of refraction. This change in index may exceed by orders of magnitude that usually associated with the Kerr effect. The irreversible change in index of refraction of a photopolymer is a function of absorbed optical energy rather than intensity. While Kerr solitons require a critical intensity of MW cm^{-2} for trapping, no critical power is needed for self-trapping in photopolymers. Self-trapping arises from a fundamentally different mechanism than Kerr spatial solitons. However, like the Kerr effect, photopolymerization is a local phenomenon, for the local index change depends on the local light intensity.

The propagation of light in a photopolymer is described by the scalar, three-dimensional, paraxial wave equation for the optical electric field envelop E in an inhomogeneous medium:

$$2ikn_o \frac{\partial E}{\partial z} + \frac{\partial^2 E}{\partial x^2} + \frac{\partial^2 E}{\partial y^2} + k^2 \left[n(x,y,z)^2 - n_o^2 \right] E = 0 \,, \qquad 10.11$$

where n and n_o are the spatially modulated and unperturbed complex indices of refraction, respectively, $k = 2\pi/\lambda$ is the wavevector for a paraxial beam propagating along the z direction and λ is the wavelength in vacuum. The index of refraction and absorption described by n depend on optical exposure, time and position x, y, z, where the real part is:

$$n' = n_o' + \Delta n' \,, \qquad 10.12a$$

and the imaginary part is:

$$n'' = n_o'' + \Delta n'' \ . \qquad 10.12b$$

The expressions for $\Delta n'$ and $\Delta n''$ given by equations 9.6 and 9.7 permit a solution to the wave equation in the photopolymer at all times.

10.3 Critical Waveguide Diameter

The guidance condition for an optical waveguide of radius r depends on the index change between the core and cladding. In this case the solid polymer is the core and the liquid photopolymer is the cladding. In general, the inequality relating the radius to the index change $\Delta n'$ is [11]:

$$k\, r\, (2n_o'\Delta n')^{1/2} \geq 2 \ . \qquad 10.13$$

For a typical $\Delta n'$ of 0.04, the smallest stable diameter of the self-trapped beam is predicted to be 0.6 μm. Therefore, if a TEM_{oo} Ar-ion beam at 488 nm initiates polymerization, the minimum transverse feature size is on the order of a micron. The actual diameter of the waveguide is expected to be slightly larger than the wavelength because of the time lag of the index change upon illumination and because of scattering of light within the waveguide.

10.4 Waveguide evolution

Some fundamental qualitative predictions regarding the evolution of the light-induced waveguide can be deduced, based on the measured index of refraction dynamics presented in figure 9.3. Figure 10.1 presents a qualitative model of the evolution of the optical waveguide upon photopolymerization. At early times and low exposures, an induction period causes exposure thresholding. The very small index change increases

approximately quadratically. Polymerization is initiated first in regions of intense illumination, so the dimension of the waveguide is smaller that the optical beam. The lens-like index profile focuses the central part of the beam. At later times, the index increases linearly with exposure, and the index distribution is a faithful replica of the transverse intensity profile. Self-focusing is remains strong. For large exposures, the index change begins to saturate at the center of the waveguide. The index is nearly uniform across the beam, and self-focusing becomes very weak. At this stage, the waveguide becomes essentially a step-index fiber. The cladding layer is composed of the unpolymerized monomer. If the optical beam is strongly confined to the core, the diameter of the waveguide will not increase significantly upon continued exposure. Of course, for very large exposures the entire liquid volume will polymerize due to the scatter of light and the diffusion of free radicals beyond the illuminated region. The index can also begin to decrease after saturation, as UV illumination begins to break bonds on the polymer backbone itself. While this is common in positive photoresists, we have not observed this effect in diacrylate and triacrylate photopolymers.

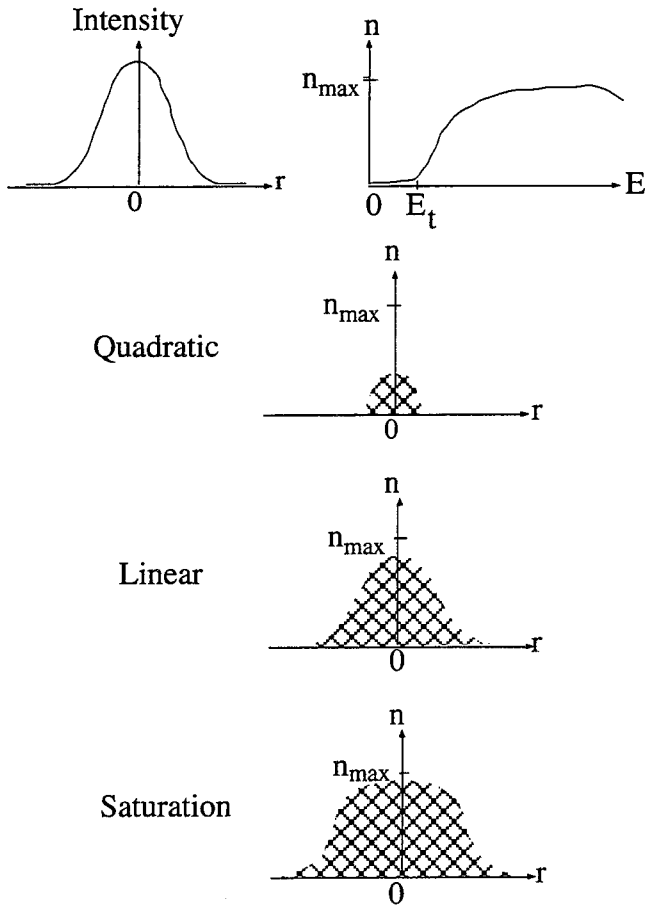

Figure 10.1: Three regimes of waveguide evolution upon photopolymerization

10.5 Summary

The propagation of light in a photopolymer is described by the nonlinear wave equation in an inhomogeneous medium. Both the index of refraction and absorption depend on optical exposure, time and position. Analytical solutions of the wave equation are overly simplistic and not described here. However, some qualitative predictions regarding the evolution of the light-induced waveguide can be drawn based an experimentally observed index dynamics. A numerical simulation of the propagation of a beam through the polymer is presented in chapter eleven.

References for chapter ten

[1] R. Y. Chiao, E. Garmire, C. H. Townes, *Phys. Rev. Lett.* **13**, 479-482 (1964).

[2] J. H. Marburger, E. Dawes, *Phys. Rev. Lett.* **21**, 556-558 (1968).

[3] M. M. T. Loy, Y. R. Shen, *Phys. Rev. Lett.* **22**, 994-997 (1969).

[4] V. N. Lugovoi, A. M. Prokhorov, *JETP Letters* **7**, 117-119 (1968).

[5] P. L. Kelley, *Phys. Rev. Lett.* **15**, 1005-1008 (1965).

[6] J. E. Bjorkholm, A. Ashkin, *Phys. Rev. Lett.* **32**, 129-132 (1974).

[7] J. S. Aitchison, A. M. Weiner, Y. Silberberg, M. K. Oliver, J. L. Jackel, D. E. Leaird, E. M. Vogel, P. W. E. Smith, *Opt. Lett.* **15**, 471-473 (1990).

[8] M. Segev, B. Crosignani, A. Yariv, B. Fischer, *Phys. Rev. Lett.* **68**, 923-926 (1992).

[9] J. G. C. Duree, J. L. Shultz, G. J. Salamo, M. Segev, A. Yariv, B. Crosignani, P. D. Porto, E. J. Sharp, R. R. Neurgaonkar, *Phys. Rev. Lett.* **71**, 533-536 (1993).

[10] B. Crosignani, M. Segev, D. Engin, P. D. Porto, A. Yariv, G. Salamo, *JOSA B* **10**, 446-453 (1993).

[11] D. Marcuse, *Theory of Dielectric Optical Waveguides.* (Academic, New York, 1974).

Chapter Eleven

Numerical Simulations of Self-Trapping and Self-Focusing Upon Photopolymerization

11.1 Introduction

Analytical solutions to the inhomogeneous wave equation with indices of refraction given by equations 9.6 and 9.7 could be obtained only for overly simplistic approximations. Consequently, we analyzed the beam propagation numerically. The propagation of the optical wave through the photopolymer is computed by solving the wave equation in an inhomogeneous medium, where the index of refraction evolves as in chapter nine. The time rate of change in the index of refraction is much slower than the period of optical oscillations, so the wave evolution can be solved at a particular time by using the index profile from the earlier time-step. This optical intensity profile is used to compute the exposure at every point in the medium, and the index of refraction is then updated before the next time-step. This iterative process is repeated to simulate both the temporal and spatial evolution of the optical beam in the nonlinear polymer medium.

11.2 Finite Differenced Beam Propagation Method

The evolution of the electric field amplitude and phase of the optical beam is computed by using the beam propagation method (BPM). BPM is typically implemented using a finite

difference rather than fast-Fourier transform method [1, 2]. The addition of a transparent boundary condition [3, 4] prevents reflections at the edge of the grid and allows the boundaries of the solution to be placed closer to the physical region of interest. This maximizes the transverse spatial resolution.

The finite differenced wave equation for propagation in the z direction and one transverse dimension x is computed by the symmetric finite difference scheme [1]:

$$- a\, E_{i-1}(z+\Delta z) + b\, E_i(z+\Delta z) - a\, E_{i+1}(z+\Delta z) \qquad 11.1$$
$$= a\, E_{i-1}(z) + c\, E_i(z) + a\, E_{i+1}(z)\ .$$

The coefficients of the scalar electric field E_i are defined as:

$$a = \frac{\Delta z}{2(\Delta x)^2}, \qquad 11.2$$

$$b = \frac{\Delta z}{(\Delta x)^2} - \frac{\Delta z}{2}\left(n_i^2(z+\Delta z) - n_o^2\right) + 2\, j\, k_o n_o, \qquad 11.3$$

and

$$c = -\frac{\Delta z}{(\Delta x)^2} + \frac{\Delta z}{2}\left(n_i^2(z) - n_o^2\right) + 2\, j\, k_o n_o. \qquad 11.4$$

The wavefront at any position $z+\Delta z$ is completely determined by the wavefront at position z. This allows the solution to be solved iteratively in the z direction. Note that the index of refraction and absorption depend on position (x,z) and time, so the expressions b and c also depend both on position and time.

Equations 11.1-11.4 are a system of linear equations that can be solved efficiently by the tridiagonal algorithm [5]. This is apparent by expressing equation 11.1 as the matrix equation $\mathbf{A}\cdot\mathbf{u} = \mathbf{b}$, where $\mathbf{u}$ is a vector composed of the discretized electric field amplitudes E_i at a particular z slice. The right-hand side of equation 11.1 can be evaluated at the input $z = 0$ to determine $\mathbf{b}$. By inverting the tridiagonal matrix $\mathbf{A}$, the electric field amplitude can be solved at each subsequent z. The value of the electric field at the boundary is computed according to the transparent boundary condition.

11.3 Results of Numerical Simulations

The evolution of the optical intensity profile is computed using the evolution of the index given by equation 9.6. The parameters of this function are determined by a least squares curve fit to figure 9.3. We ignore the induction period because the oxygen level in the self-trapping experiments is dramatically lower than that of the index measurement. Typical photopolymer compositions used in these experiments have low optical absorption associated with the photoinitiator (0.48 cm^{-1} at 325 nm), so photobleaching is also ignored.

Figure 11.1 illustrates a numerical simulation of the intensity profile of the self-trapped, one dimensional Gaussian beam in a photopolymer liquid. The gray scale of the simulation is linearly related to the optical intensity. The waist of the beam is located at z=0, the input surface of the photopolymer. The beam radius at the input is equal to two wavelengths and the propagation distance is 10^3 wavelengths. Note that the horizontal scale is magnified by a factor of ten compared to the vertical scale, to improve transverse resolution. The left-most simulation illustrates the evolution of the beam through the homogeneous photopolymer before any index changes are induced. The time-steps from left to right are in units of 5 t_c. t_c is a normalized parameter chosen to be equal to that time to reach the gel point at the location of maximum intensity (z=0, r=0) of the optical beam. The gel point

corresponds to the 1-1/e point on the index of refraction change versus exposure curve. Self-trapping of the optical beam over a distance of 500 wavelengths is apparent after an exposure of 15 t_c, the right-most figure. The oscillations in the beam diameter evident at 15 t_c appear to be a common phenomenon for self-trapped beams. Indeed, this effect has also been predicted for Kerr spatial solitons [6]. The background absorption length is 10^3 wavelengths, so self-trapping terminates in approximately this distance because the exposure remains extremely weak.

These simulations are highly sensitive to numerical precision and the accuracy of the transparent boundary condition. In left-most simulation in figure 11.1, the beam intensity is extremely weak after propagating 200 wavelengths because of the strong diffraction. Beyond this propagation distance, numerical precision becomes inadequate since the intensity decreases as the inverse square of the propagation distance for the unguided beam. As a consequence, the on-axis intensity is slightly lower than the off-axis intensity, an unphysical result. This computing artifact is only apparent in the regions of extremely weak optical intensity, which lie outside the problem area of interest.

These calculations also reveal self-focusing for the same beam and material parameters. Figure 11.2 illustrates the focusing of a Gaussian beam with its waist at z = 0, for a propagation distance of 100 wavelengths. Again, the input beam radius is 2 wavelengths. The top figure illustrates the diffraction of a Gaussian beam in the homogeneous liquid photopolymer before crosslinking. The bottom figure reveals strong self-focusing after 15 t_c. The minimum beam diameter is approximately a factor of 2 smaller than the input waist after propagating approximately 20 wavelengths.

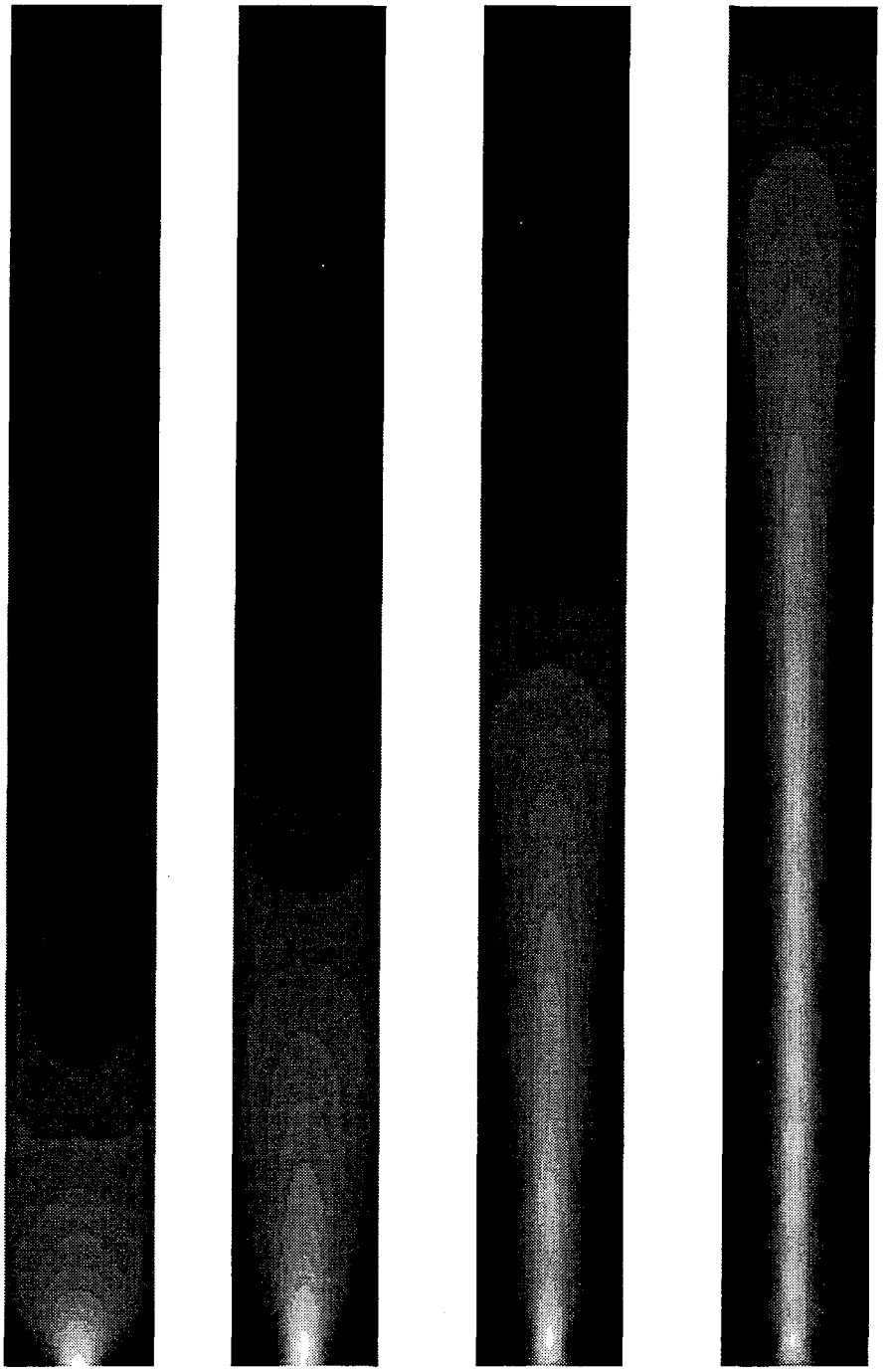

Figure 11.1: Numerical simulations of beam propagation in photopolymer in timesteps equal to 5 t_c. Leftmost beam: t = 0, rightmost beam: t = 15 t_c. The vertical scale is 10^3 wavelengths, horizontal scale is 10 wavelengths.

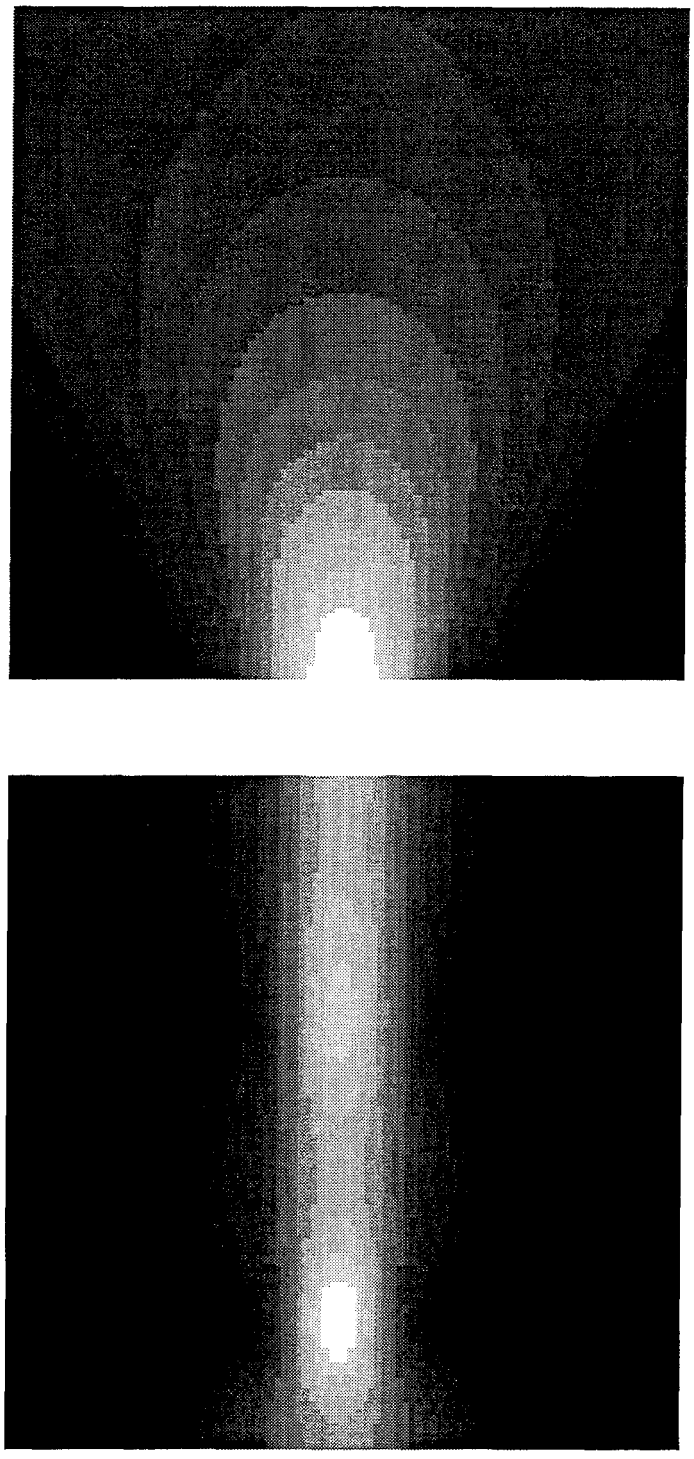

Figure 11.2: Numerical simulation of self-focusing upon photopolymerization. Top: t = 0, bottom: t = 15 t_c. The vertical scale is 100 wavelengths, horizontal scale is 10 wavelengths. The periodic focusing is indicative of self-trapping.

11.4 Summary

Numerical simulations of beam propagation upon photopolymerization for typical material parameters display self-focusing and self-trapping. The diameter of the self-trapped beam oscillates with propagation distance, similar to the Kerr soliton results described in chapter ten. These results agree qualitatively with the experimental demonstration to be discussed in chapter twelve.

References for chapter eleven

[1] Y. Chung, N. Dagli, *IEEE J. Q.E.* **26**, 13351-1339 (1990).

[2] L. Sun, G. L. Yip, *Opt. Lett.* **18**, 1229-1231 (1993).

[3] G. R. Hadley, *Opt. Lett.* **16**, 624-626 (1991).

[4] G. R. Hadley, *IEEE J. Q. E.* **28**, 363-370 (1992).

[5] W. H. Press, S. A. Teukolsky, W. T. Vetterling, B. P. Flannery, *Numerical Recipes in C-The Art of Scientific Computing*. (Cambridge University Press, Cambridge, 1992).

[6] J. H. Marburger, E. Dawes, *Phys. Rev. Lett.* **21**, 556-558 (1968).

Chapter Twelve

Applications of Self-Trapping and Self-Focusing in Photopolymers

12.1 Introduction

Self-focusing and self-trapping of optical beams overcome the diffraction effects which become significant for optical beams with diameters on the order of an optical wavelength. The waveguide associated with the self-trapped beam forms microscopic filaments from which polymeric microstructures can be fabricated. This technique has applications to high resolution photolithography, microstereolithography and micromachining. These applications will be described in detail in this chapter.

12.2 Application of Self-Focusing to High Resolution Photolithography

The primary obstacle to the continued increase in integrated circuit density is the limitation on the resolution and depth of focus in the photolithography stage. The smallest feature size x_{min} that can be projected by a coherent imaging system is

$$x_{min} = \frac{\lambda}{2\ \text{N.A.}} \qquad 12.1$$

and the depth of focus (DOF) is:

$$DOF = \frac{\lambda}{2\,(N.A.)^2}\ , \qquad 12.2$$

where λ is the wavelength of the illumination and N.A. is the numerical aperture. The most direct route to smaller feature sizes is to reduce the wavelength from the i-line standard of today (365 nm) to excimer laser wavelengths (248 or 193 nm). The N.A. is typically 0.5, so the feature size is on the order of the exposure wavelength. State-of-the-art semiconductor fabrication facilities in the year 2005 are forecasted to use a 0.1 μm process, at which point the resolution and depth of focus constraints of optical lithography become severe. Therefore, techniques to extend the performance of optical lithography into this regime are of particular technological and economic significance.

One proven method to improve the resolution is based on a contrast enhancement layer (CEL) composed of a photobleachable dye overcoated on the photoresist [1-11]. Upon projecting a photolithography mask onto the CEL, the regions exposed to the highest intensity bleach first, while those parts of the layer that receive the lowest intensity are absorbed. The effect of the photobleachable layer is to increase the contrast of the projected image by introducing exposure thresholding. Extensive work has been done to develop materials for contrast enhancement based on bleachable dyes, which has been incorporated into a 0.25 μm i-line process [3].

Improvements in the resolution and the depth of focus may be attained by exploiting the nonlinear optical property of self-focusing upon photopolymerization [12]. When a liquid photopolymer is illuminated with UV radiation, the exposed regions crosslink to form a solid with an index of refraction typically 0.1 to 0.04 larger than the liquid. This exposure dependent index of refraction leads to self-focusing. Therefore, a standard photoresist may be overcoated with a resolution enhancement layer (REL) that self-focuses the light (figure

12.1) before developing the photoresist. The addition of a REL to present and future lithography processes has the potential of reducing the feature size to half an exposure wavelength using existing steppers and photoresists, a factor of two improvement in resolution.

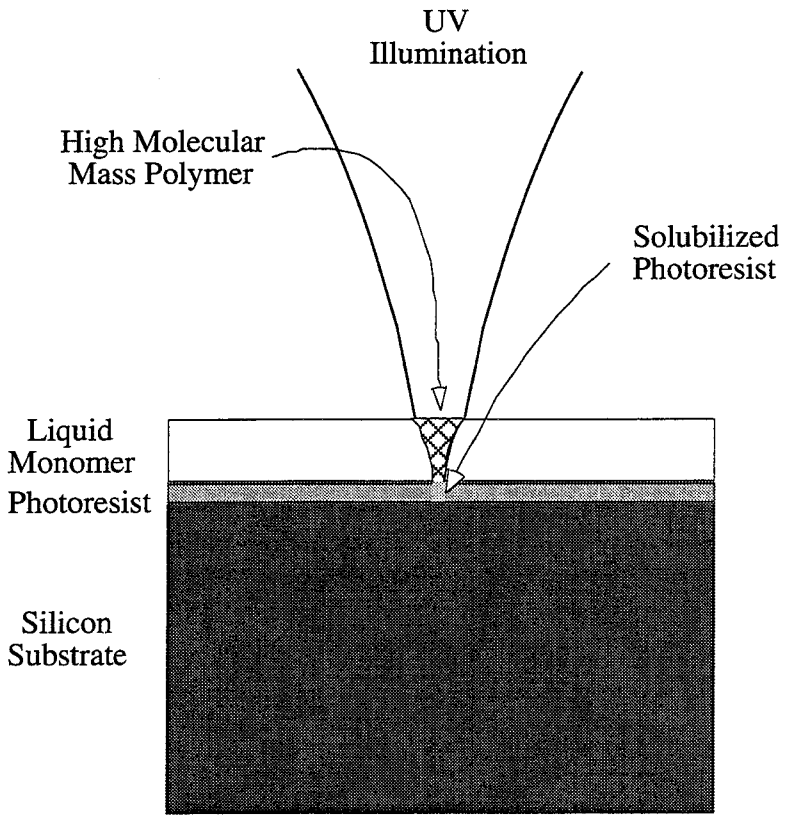

Figure 12.1: Resolution enhancement layer for photolithography.

A numerical simulation of the propagation of a single illuminated line through a REL (figure 11.2) indicates that the feature size may be reduced by more than a factor of two upon propagating 20 wavelengths in the medium. Theoretical predictions based on the measured index changes upon photopolymerization suggest that the optimal REL thickness for a 0.3 μm process is 2 to 3 μm. If the waveguiding is strong enough, the focused

optical beam becomes trapped, dramatically extending the depth of focus. For instance, figure 11.2 shows that the beam diameter remains smaller than its input waist while propagating over a distance of 100 wavelengths. We believe that the addition of a photobleachable dye to the REL will reduce the oscillations in the beam diameter and trap the beam at a smaller diameter.

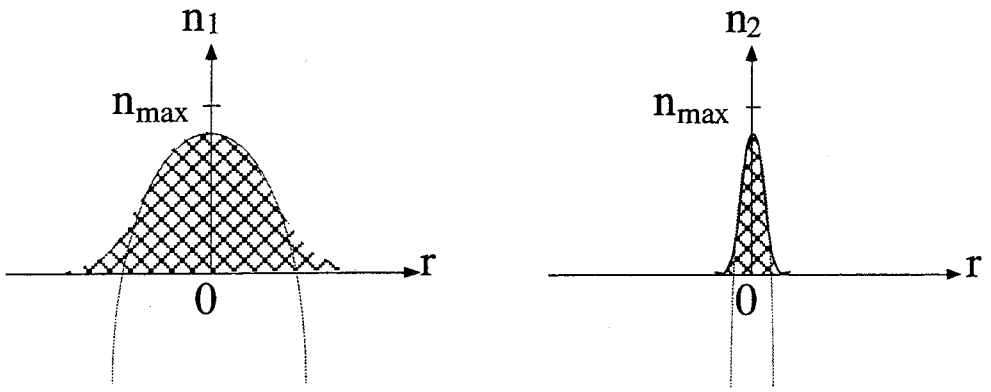

Figure 12.2: Approximate model of self-focusing layer index profile by a quadratic function of radius from center of optical beam.

The self-focusing can be dealt with analytically by treating the index profile within the medium as quadratic. For a input beam of large diameter (representative of an individual pixel, for example), the index profile is

$$n_1(r) = n_o\left(1 - \frac{\Delta n_1^2}{2} r^2\right) . \qquad 12.3$$

For an input beam of smaller diameter, the index profile is

$$n_2(r) = n_o\left(1 - \frac{\Delta n_2^2}{2} r^2\right) . \qquad 12.4$$

In both instances, the effective focal length is a function of the propagation length of the medium and the index change Δn [13]:

$$f = \frac{1}{\Delta n} \frac{1}{\sin \Delta n L} . \qquad 12.5$$

For the example of figure 12.2, Δn_2 is greater than Δn_1, so $f_1 > f_2$. This leads us to the fortuitous condition that the self-focal length decreases with beam diameter. The self-focal lengths for different feature sizes and index changes are summarized in figure 12.3.

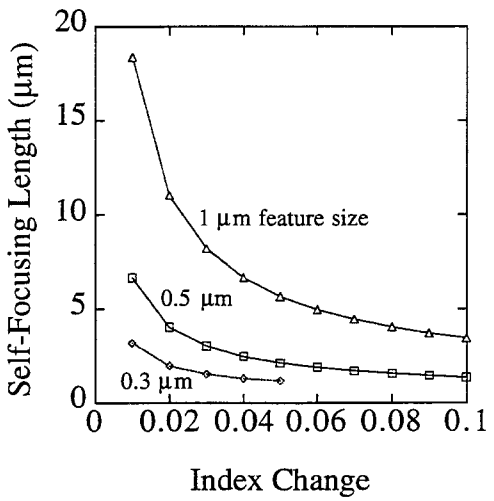

Figure 12.3: Self-focal length as a function of minimum feature size and index change across profile of optical beam.

There are several requirements on the photopolymer system for a practical REL. First, the rate of crosslinking within the self-focusing layer must be rapid enough that the light is focused before the underlying photoresist is exposed. This implies that the exposure necessary to induce self-focusing should be smaller than the optical energy required to

expose the photoresist. Alternately, two different wavelengths can be used, first to create the lens, next to expose the photoresist. Second, the addition of a photobleachable dye within the REL will enhance and stabilize the focusing effect. Third, since the excitation rate of radicals is typically larger than the rate of crosslinking, the light source should be intensity modulated to allow the material to crosslink partially before the next exposure pulse. Fourth, the viscosity of the monomer should be sufficiently high that the radicals do not diffuse into the unexposed regions during the time scale of the optical exposure. Fifth, the sensitivity of the REL must be high enough that wafer throughput is not sacrificed. Finally, the REL must be easily removed by a suitable solvent. While these requirements are numerous, the REL is essentially a thick negative photoresist, so the majority of these issues have already been addressed in a different context.

Some candidate monomers for resolution enhancement layers are ethylene, isobutylene, acrylonitrile and vinyl chloride. The distinctive feature of thes materials is a large density upon photopolymerization. Their chemical structure is described in table 12.1. Acrylonitrile has be photoinitiated by xanthene dyes (fluorescein, Rose Bengal) in the presence of reducing agents (phenylhydrazine, ascorbic acid) and oxygen. The amount of dye required was very small, 0.1% of the weight of the monomer, yet the quantum yield of monomer consumption was in excess of 4000 monomer units per photon [14]. The addition of bleachable dyes may further enhance the resolution, as demonstrated with contrast enhancement layers.

Monomer Name:	Monomer:	Polymer:
ethylene	$CH_2=CH_2$	$\left[-CH_2-CH_2-\right]_n$
isobutylene	$CH_2=C(CH_3)_2$	$\left[-CH_2-C(CH_3)_2-\right]_n$
acrylonitrile	$CH_2=CH-CN$	$\left[-CH_2-CH(CN)-\right]_n$
vinyl chloride	$CH_2=CN-Cl$	$\left[-CH_2-CH(Cl)-\right]_n$

Table 12.1: These low molecular weight monomers [15] typically undergo a relatively large density change upon photopolymerization, and for this reason are well suited as resolution enhancement layers in the presence of a suitable photoinitiator species (e.g., Irgacure 369).

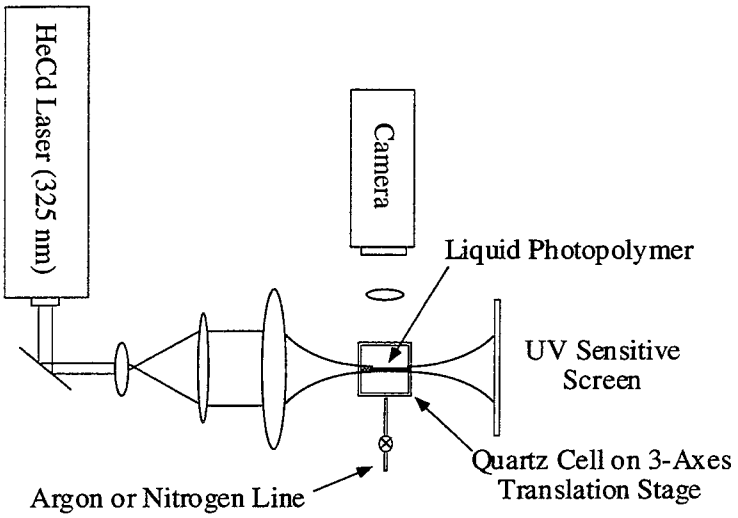

Figure 12.4: Experimental setup for photopolymerization.

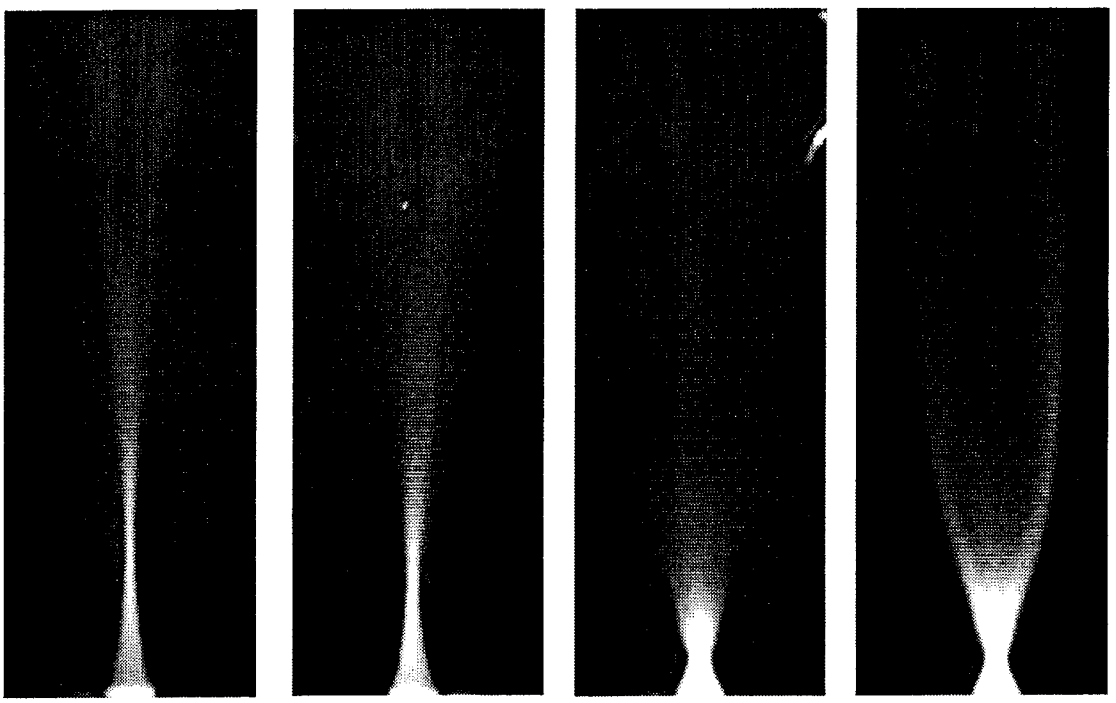

Figure 12.5: Self-focusing upon photopolymerization. Leftmost: photopolymer at t = 0; Rightmost: photopolymer at t = 30 seconds.

We have demonstrated self-focusing in a liquid diacrylate monomer in the experimental configuration of figure 12.4. The input beam is a 5 mW, TEM_{oo} Gaussian mode at 325 nm from a HeCd laser, with a diameter at the input face of 100 μm. The samples are polymerized within a 1x1x5 cm quartz cuvette filled with a diacrylate photopolymer. Prior to exposure, nitrogen is bubbled through the liquid to liberate the material of oxygen scavengers. All experiments are conducted at ambient temperature and humidity.

Figure 12.5 illustrates the evolution of a self-focused beam upon photopolymerization. The vertical scale is 2 mm, the horizontal scale is 500 μm. The illuminated regions correspond to the visible florescence emitted by the photopolymer. The left-most figure illustrates the beam profile at t=0 inside the liquid photopolymer. The time increases from left to right. The right-most figure is taken after approximately 30 seconds of continuous illumination with 2 mW incident intensity. The position of the beam waist moves closer to the input plane as photopolymerization proceeds, a manifestation of self-focusing. However, the beam waist increases rather than decreases. To improve the self-focusing, the intensity of the input beam should be modulated to allow the slow index time response to keep up with the rapid photoexcitation time response.

12.3 Application of Self-Trapping to the Fabrication of Polymeric Microstructures

We have used self-trapping to fabricate solid optical fiber cores as long as 3 cm with diameters of 10 μm to 1 mm. The input beam is a 5 mW, TEM_{oo} Gaussian mode at 325 nm from a HeCd laser (figure 12.4). The samples are grown within a 1x1x5 cm quartz cuvette filled with either a diacrylate or triacrylate photopolymer. Prior to exposure, nitrogen or argon is bubbled through the liquid to liberate the material of oxygen scavengers. Exposures are conducted in regions of the liquid several mm below the polymer-air interface, to minimize the effects of subsequent oxygen indiffusion .

Figure 12.6 shows a series of polymeric fibers of 10 μm diameter and several mm length still submerged within the liquid photopolymer. The optical contrast in the photograph is a result of the large index perturbation in the region of the crosslinked solid. Several minutes after the exposure, the fibers bend downward under the force of gravity, because the solid fibers are more dense than the liquid surroundings. Each fiber is exposed 30 times for 1/16 second, with a delay of 1 to 5 seconds between each successive exposure. The continued crosslinking within the waveguide is visually apparent for several second after the UV illumination is blocked. This observation has been used to tailor the delays between UV exposures to optimize the self-focusing process. Regular arrays of fibers of 200 μm diameter and 10 mm length have been fabricated in an epoxy-triacrylate photopolymer, as illustrated in figure 12.7. Each post was formed using a *single* 1/8 second exposure, so trapping was not as dramatic. Hence, the diameter of the waveguides are significantly larger.

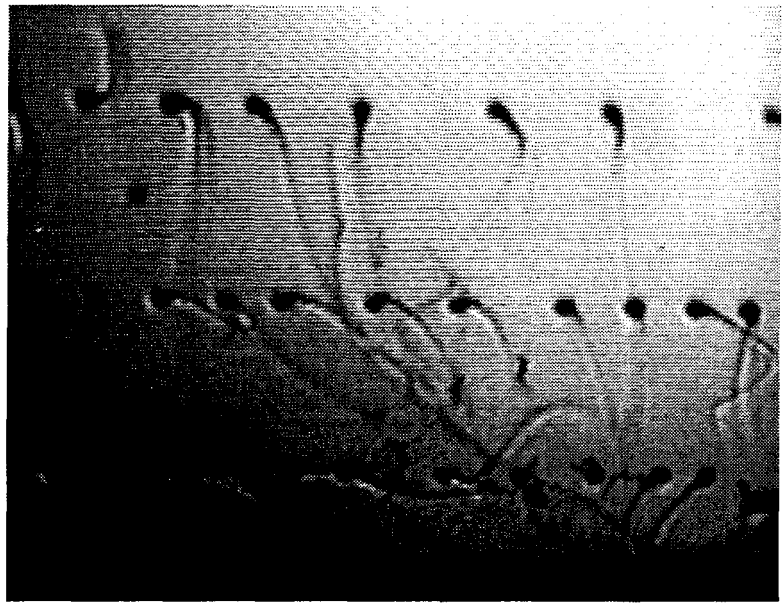

Figure 12.6: Series of fibers grown by self-trapping the UV curing beam. The nominal diameter is 10 μm.

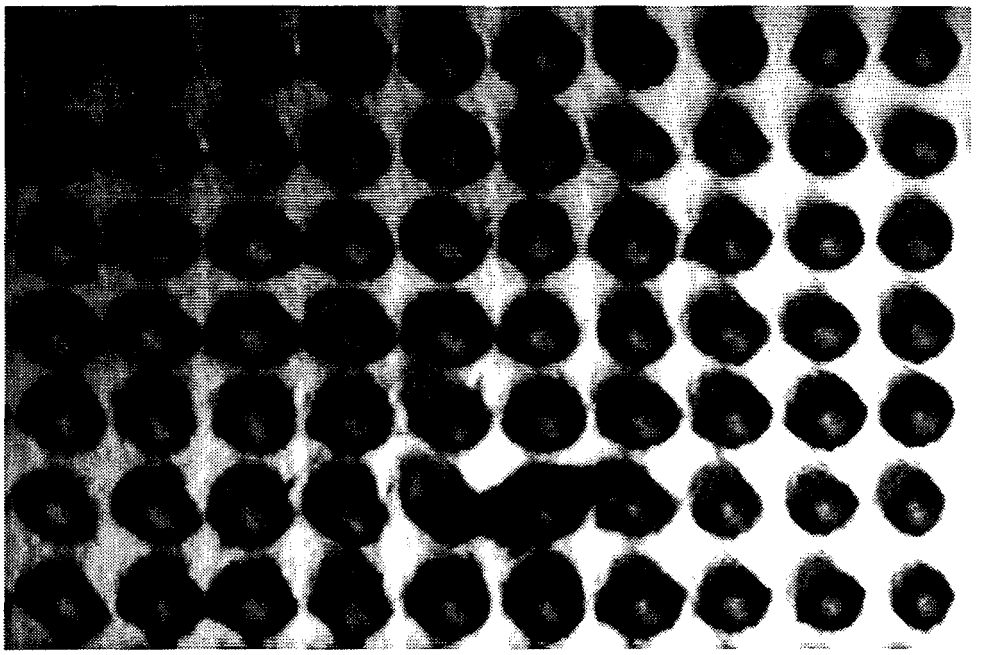

Figure 12.7: Array of fibers of 200 μm diameter and 10 mm length.

The direction of growth of these fibers can be controlled by changing the intensity distribution of the optical beam at the input. Any perturbation from radial symmetry across the intensity profile of the beam leads to the filamentation and break-up of the optical beam. This break-up can be used to produce optical fiber "Y" junctions, for instance. In addition, by introducing an asymmetry in the intensity profile, the fiber can be steered as it is grown, because one side of the waveguide will induce stronger self-focusing to deflect the beam.

An array of fiber-like structures can be fabricated to produce a three-dimensional microlattice. The fabrication technique described here is ideal for producing high aspect ratio structures with dimensions on the order of optical wavelengths, and index changes as large as 0.7 between air and the polymer. A primitive three-dimensional lattice of fiber-like

filaments can be fabricated using this technique (figure 12.9). The diameter of each solid filament is 50 μm, spaced by approximately 500 μm.

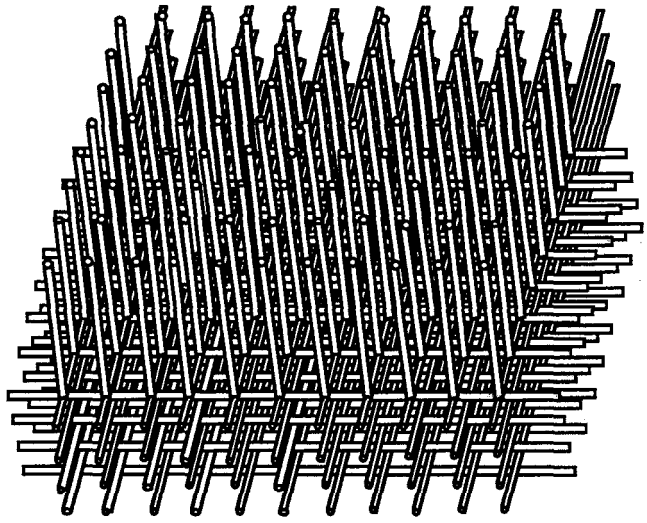

Figure 12.8: Three-dimensional fiber lattice microstructure.

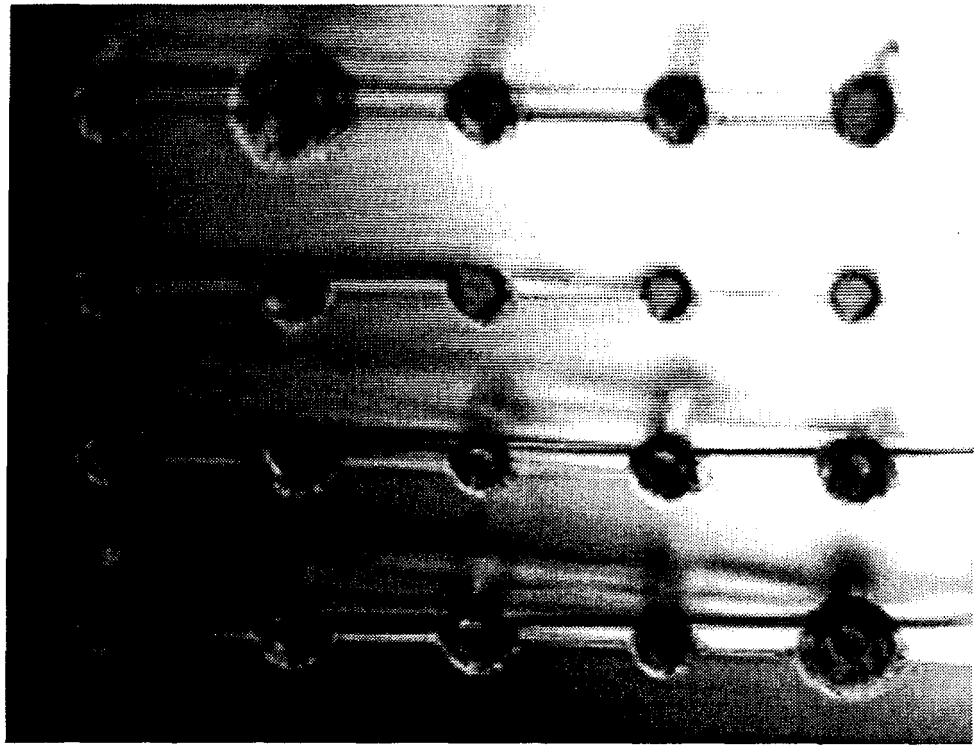

Figure 12.9: Three-dimensional fiber lattice with 50 μm diameter filaments fabricated within a photopolymer filled cuvette.

12.4 Data Storage in Corrugated Waveguides

By modulating the diameter of these waveguides periodically, the reflectivity spectrum of the fiber can be tailored. The theory of dielectric waveguides with modulated diameters has been developed by Marcuse [16-18]. Forward waveguide modes of a particular wavelength λ are coupled to backward waveguide modes by modulating the waveguide diameter every $\lambda/2n$. By introducing many different spatial frequency components, (as in a chirped distributed feedback grating) information can be encoded in the optical reflectivity spectrum of each fiber. The presence of a particular periodicity corresponds, say, to a bit "1", and the absence to a bit "0". Each bit will be read out by measuring the amount of light reflected from the fiber at a particular wavelength address. A tunable laser can read out data from a multitude of adjacent waveguides simultaneously.

This memory architecture has the advantages inherent in holographic storage systems (e.g., fast, parallel access, high information density 10^{12} bits cm^{-3}). In addition, it is unique because the memory is permanent and the dynamic range is extremely large. The index difference obtained once the uncured polymer is removed is ~0.5, compared to an index change of 10^{-3} in ferroelectric photorefractive materials. It can potentially be applied to a memory system analogous to a multi-level CD ROM with a terabyte memory capacity.

12.5 Optical Extrusion

The two primary tools for micromachining in silicon are sacrificial layers and anisotropic etching. These techniques enable microstructures as thick as a hundred microns to be fabricated. A complementary tool to produce deep structures in silicon is ion beam milling. In addition, thick microstructures are fabricated in polymers, metals, and ceramics using the LIGA process [19-24]. This tool uses synchrotron radiation lithography to produce

precise masters of three-dimensional microstructures with very high depth-to-width aspect ratios. A subsequent electroforming stage converts the polymer structure into a metal master, which can serve as a mold for additional replication.

A new tool for micromachining deep structures based on optical self-trapping is called optical extrusion [12]. Traditional deep etch techniques such as LIGA project a collimated beam of x-rays or ions onto a proximity mask whose feature size is typically microns, so diffraction effects are negligible. However, undesirable diffraction occurs as the illumination wavelength approaches the feature size. That is, for a high resolution mask imaged by coherent light at wavelength λ in an optical system of numerical aperture N.A., the depth of focus z_{max} is:

$$z_{max} = \frac{\lambda}{2\,(\text{N.A.})^2} . \qquad 12.6$$

The depth of focus is typically only a micron for UV illumination at 365 or 248 nm. To produce a deep structure using UV illumination, the part must normally be built up layer by layer as in stereolithography [25, 26], where the layer thickness is less than the depth of focus.

An important exception to this depth of focus constraint occurs when imaging in nonlinear optical materials such as photopolymers. Strong optical nonlinearities are present upon photopolymerization. As UV illumination impinges on a photosensitized liquid monomer, it produces free radicals which initiate polymerization and crosslinking of the monomer to form a solid. The index of refraction of the solid is typically 0.04 larger than the index of the liquid, so strong optical waveguiding is induced. This guides the beam through the liquid without diffraction, leaving a solid structure in its path. The diameter of the beam is

maintained as it propagates through the liquid, providing a new tool to create thick microstructures.

A simple implementation of optical extrusion is illustrated in figure 12.10. A reservoir of liquid photopolymer is placed over a standard photolithography mask, which is back illuminated by a collimated source of UV illumination (a He-Cd laser at 325 nm or a mercury i-line lamp at 365 nm). The absorption is chosen to be sufficiently strong that only a thin layer of photopolymer will cure at any one time. However, as the absorption of this layer bleaches, the light is guided to the next layer where the same image is exposed. As this process continues, a polymeric structure whose cross section is a replica of the original mask is extruded. Because this is an additive process, other structures can be subsequently woven-in by projecting masks in different directions. Finally, the uncured monomer is removed by an appropriate solvent, leaving only the desired part. Like the LIGA process, these parts may be converted into complementary metal structures by a subsequent electroforming stage.

These extruded parts have many applications to microfabrication. Optical fiber coupling segments can be grown from the facets of laser arrays to facilitate fiber coupling. Optical interconnects, x-ray optics and indeed any structure produced using the LIGA technique can be fabricated. The primary commercial advantage of optical extrusion over LIGA is the use of a standard UV light bulb rather than a synchrotron radiation source, albeit at the expense of a more complicated photopolymer system.

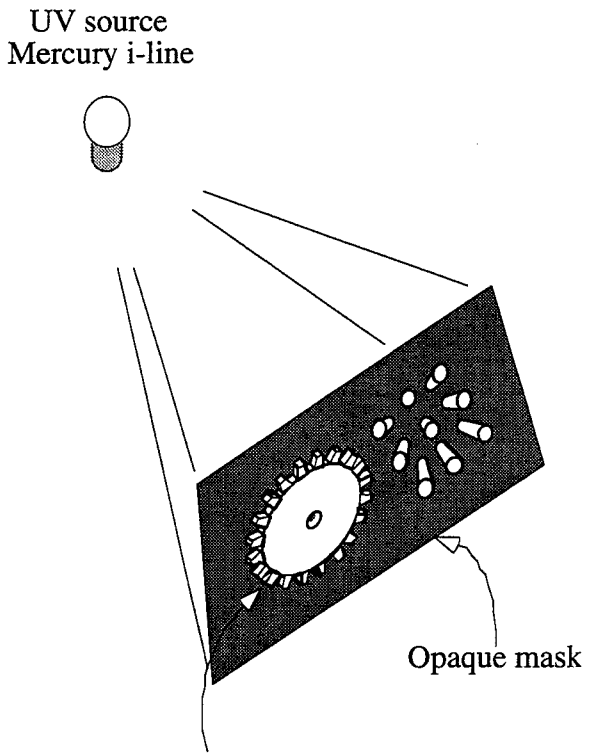

Figure 12.10: Optically extruding thick, polymeric microstructures by using waveguiding of UV illumination to overcome mask diffraction.

12.6 Self-Organized Semiconductor Laser to Fiber Coupling

Efficient coupling of the highly divergent beams from semiconductor lasers to fibers is a major technical hurdle. By selecting a photosensitizer/photoinitiator system with strong absorption at the laser wavelength (typically in the near IR, 0.7 to 1.5 mm), fibers can be grown from the laser output coupler automatically, guided by the output beam of the laser itself. In principle, this allows very efficient , self-aligned, tappered, and high numerical aperture fiber coupling to lasers or indeed any device.

12.7 Summary

In summary, we have demonstrated theoretically and experimentally that optical beams are self-focused and self-trapped upon photopolymerization. Self-trapping is used to fabricate polymeric fibers of 10 μm diameter and 10 mm length. These filaments are used to directly fabricate polymeric microstructures in polymers. Fibers have been grown in different directions to "weave" three-dimensional lattices. In principle, this technique provides an alternative to using x-rays or ion beams to deep etch structures in polymers. Self-focusing in photoresist systems may enhance the resolution of optical photolithography for microelectronics. This nonlinear optical phenomenon provides a novel tool to permanently tailor the optical and structural properties of the polymer on a microscopic scale.

References for chapter twelve

[1] S. V. Babu, E. Barouch, B. Bradie, *J. Vac. Sci. Technol. B* **6**, 564-568 (1988).

[2] S. V. Babu, E. Barouch, *J. of Imaging Science* **33**, 193-199 (1989).

[3] B. Davari, W.-H. Chang, K. E. Petrillo, C. Y. Wong, D. Moy, Y. Taur, M. R. Wordeman, J. Y.-C. Sun, C. C.-H. Hsu, M. R. Polcari, *IEEE Transactions on Electron Devices* **39**, 967-975 (1992).

[4] M. Endo, M. Sasago, Y. Hirai, K. Ogawa, T. Ishihara, *J. Vac. Sci. Technol. B* **6**, 87-90 (1988).

[5] B. F. Griffing, P. R. West, in *Solid State Technology* . 1985), pp. 152-157.

[6] Y. Hirai, M. Sasago, M. Endo, K. Ogawa, Y. Mano, T. Ishihara, *J. Vac. Sci. Technol. B* **5**, 434-438 (1987).

[7] D. C. Hofer, C. G. Willson, A. R. Neureuther, M. Hakey, Optical Microlithography-Technology for the Mid-1980's (SPIE, 1982), vol. 334, pp. 196-205.

[8] K. Kaifu, T. Itoh, M. Kosuge, Y. Yamashita, S. Ohno, T. Asano, K. Kobayashi, G. Nagamatsu, *J. Vac. Sci. Technol. B* **5**, 439-442 (1987).

[9] W. Loong, H. Pan, *J. Vac. Sci. Technol. B* **8**, 1731-1734 (1990).

[10] T. Ochiai, Y. Kameyama, R. Takasaki, T. Ishiguro, M. Nishi, K. Miura, *J. Photochem. Photobiol. A: Chem.* **65**, 277-284 (1992).

[11] Y. Tomo, H. Junbo, Y. Yamashita, S. Ohno, T. Asano, S. Nishibu, H. Umehara, *Polymer Engineering and Science* **29**, 902-906 (1989).

[12] A. S. Kewitsch, A. Yariv *U.S. Patent pending*, (1995).

[13] A. Yariv, *Quantum Electronics* (Wiley, New York, 1989).

[14] G. Oster, *Nature* **173**, 300 (1954).

[15] G. Odian, *Principles of Polymerization* (Wiley, New York, 1981).

[16] D. Marcuse, *Bell Sys. Tech. J.* **48**, 3187-3215 (1969).

[17] D. Marcuse, *Bell Sys. Tech. J.* **48**, 3233-3242 (1969).

[18] D. Marcuse, *Theory of Dielectric Optical Waveguides* (Academic, New York, 1974).

[19] S. Abel, H. Freimuth, H. Lehr, H. Mensinger, *J. Micromech. Microeng.* **4**, 47-54 (1994).

[20] K.-H. Brenner, M. Kufner, S. Kufner, J. Moisel, A. Müller, S. Sinzinger, M. Testorf, J. Göttert, M. Mohr, *Appl. Opt.* **32**, 6464-6469 (1993).

[21] C. Burbaum, J. Mohr, P. Bley, *Sensors and Actuators A* **25-27**, 559-563 (1991).

[22] C. Müller, J. Mohr, *InterDisciplinary Science Reviews* **18**, 273-279 (1993).

[23] D. Münchmeyer, J. Langen, *Rev. Sci. Instrum.* **63**, 713-721 (1992).

[24] O. Wollersheim, H. Zumaqué, J. Hormes, J. Langen, P. Hoessel, L. Häußling, G. Hoffmann, *J. Micromech. Microeng.* **4**, 84-93 (1994).

[25] A. J. Herbert, *J. Appl. Photographic Eng.* **8**, 185-188 (1982).

[26] C. W. Hull, 3D Systems, Valencia, CA, Integration of Stereolithography into Agile Manufacturing (1993).

Chapter Thirteen

Relevant Publications

Self-Focusing and Self-Trapping of Optical Beams Upon Photopolymerization, A. Kewitsch, A. Yariv, to be published.

Permanently Fixed Volume Phase Gratings in Ferroelectrics, A. Kewitsch, A. Yariv, M. Segev, Chapter 9, The Photorefractive Effect, Ed. D. Nolte, (Kluwer Academic, 1995).

Optically Induced Quasi-Phase Matching in Strontium Barium Niobate, A. Kewitsch, G. Salamo, T. Towe, A. Yariv, M. Tong, M. Segev, E. Sharp, R. Neurgaonkar, Appl. Phys. Lett. **66**, 1865 (1995).

Optical and Electrical Barkhausen Noise Induced While Recording Ferroelectric Domain Holograms, A. Kewitsch, A. Saito, M. Segev, A. Yariv, R. Neurgoankar, accepted to JOSA B (1995).

Ferroelectric Domain Gratings Induced by Photorefractive Space Charge Fields, A. Kewitsch, M. Segev, A. Yariv, G. Salamo, T. Towe, E. Sharp, R. Neurgoankar, Phys. Rev. Lett. **73**, 1174 (1994).

Tunable Quasi-Phase Matching Using Dynamic Ferroelectric Domain Gratings Induced by Photorefractive Space-Charge Fields, A. Kewitsch, M. Segev, A. Yariv, G. Salamo, T. Towe, E. Sharp, R. Neurgoankar, Appl. Phys. Lett. **64**, 3068 (1994).

Controlled, Periodic Domain Formation in Strontium Barium Niobate Induced by Volume Holograms, A. Kewitsch, M. Segev, A. Yariv, R. Neurgoankar, Jpn. J. Appl. Phys. **32**, 5445 (1993).

Selective, Page-Addressable Fixing of Volume Holograms in Strontium Barium Niobate, A. Kewitsch, M. Segev, A. Yariv, R. Neurgoankar, Opt. Lett. **18**, 1262 (1993).

Electric-field Multiplexing/Demultiplexing of Volume Holograms in Photorefractive Media, A. Kewitsch, M. Segev, A. Yariv, R. Neurgoankar, Opt. Lett. **18**, 534 (1993).

Self-Enhanced Diffraction From Fixed Photorefractive Gratings During Coherent Reconstruction, M. Segev, A. Kewitsch, A. Yariv, G. Rakuljic, Appl. Phys. Lett. **62**, 907 (1993).

Electric Field Multiplexing, Selective Fixing, Overwriting and Erasure of Volume Holograms, and Quasi-Phase Matched Second Harmonic Generation Using Optically Induced Domain Gratings, A. Kewitsch, M. Segev, A. Yariv, U.S. Patent Application No. 08/037,076, January 1993.

Self-Focusing and Self-Trapping of Optical Beams Upon Photopolymerization, A. Kewitsch, A. Yariv, US Patent Application pending.